An Off-line Methodology to Determine Limits of Lubrication in Sheet Metal Forming

Üstünyagiz, Esmeray

Publication date:
2018

Document Version
Publisher's PDF, also known as Version of record

An Off-line Methodology to Determine Limits of Lubrication in Sheet Metal Forming

PhD Thesis

$$(EIv'')'' = q - \rho A\ddot{v}$$

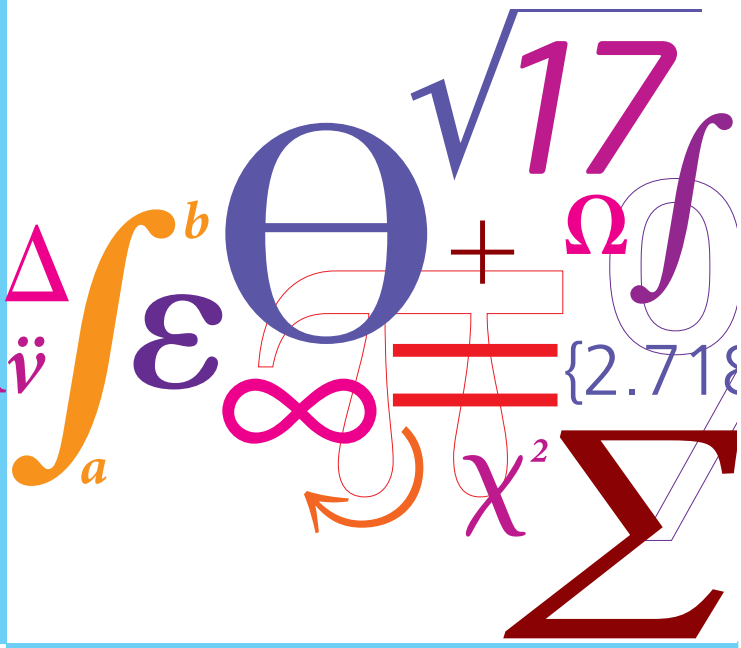

Esmeray Üstünyagiz
September 2018

DTU Mechanical Engineering
Department of Mechanical Engineering

An Off-line Methodology to Determine Limits of Lubrication in Sheet Metal Forming

In partial fulfilment of the requirements for the degree of Philosophiae Doctor

Esmeray Üstünyagiz

Kongens Lyngby 2018

Technical University of Denmark
Department of Mechanical Engineering
Nils Koppels Allè, Building 404,
2800 Kongens Lyngby, Denmark
Phone +45 4525 1960
www.mek.dtu.dk

Preface

This thesis is submitted in partial fulfilment of the requirements for acquiring a Philosophiae Doctor degree. The PhD work was carried out from 1st of March, 2015 until 30th of September, 2018 including seven months of leave of absence due to a research stay as a Graduate Research Associate at The Ohio State University, USA.

The supervision of the project was divided among Professor Niels Bay as a main supervisor, Professor Emeritus since 1.4.2017, and co-supervisors Associate Professor Chris V. Nielsen and Professor Paulo A.F. Martins.

The majority of the project was carried out within the research group of Professor Niels Bay at the Manufacturing Engineering Section of the Mechanical Engineering Department at the Technical University of Denmark (DTU). Part of the project was carried out at Grundfos A/S by means of performing experiments in the production and regular contact during the whole project period. A considerable amount of time was also spent abroad. An external stay of six weeks was hosted by Professor Paulo Martins and his group at the Department of Mechanical Engineering, Instituto Superior Técnico (IST), Technical University of Lisbon, Portugal. Additionally, two external stays of a total of two weeks took place at the Technical University of Dortmund for collaboration work with Professor Paulo Martins during his visit at TU Dortmund. Finally,

nine weeks of external stay took place at The Ohio State University at the Center for Precision Forming under the supervision of Emeritus Professor Taylan Altan.

I would like to thank all my supervisors for their contributions to this project. Particularly, I would like to express my gratitude to Professor Niels Bay for the long discussions and for sharing his expertise with me. His experience in metal forming and tribology has truly been an inspiration. In spite of his retirement, he has kept the project on track by his continuing supervision during the entire process. Professor Paulo Martins is greatly acknowledged for his outstanding engagement, providing a broad view on modelling and hosting my multiple research visits. Associate Professor Chris Nielsen is acknowledged for his brilliant advice in designing the experiments in laboratory and modelling as well as for daily discussions in many topics. Emeritus Professor Taylan Altan is deeply thanked for giving me the opportunity to work in his group and being a true inspiration through his engagement in the field of metal forming.

I would like to thank Ermanno Ceron for helping and guiding me during my visits to Grundfos A/S and for answering my many questions regarding the production case study. A special thanks is due to Nikolas A. Paldan who was involved during the tool design and shared his expertise not only in tool design but also in various aspects of the tribotester as one of the designers of it. All members of the instruments group, particularly Frida Gideon Husmark and Claus Grølsted, and the workshop group have been a great support during the laboratory tests and are kindly acknowledged. Thanks to my colleagues for sharing the daily life.

At last I would like to express my thanks to my closest family and friends for their patience and understanding during this project. I acknowledge Linus Klemp for proofreading the work. Anneciğim, babacığım ve canım kardeşim, çalışmalarım boyunca manevi desteğinizle beni hiçbir zaman yalnız bırakmadığınız için sonsuz teşekkürler.

Lyngby,

September 30th, 2018

Esmeray Üstünyagiz

In partial fulfilment of the requirements for the degree of
Philosophiae Doctor

Abstract

In order to sustain in the competitive market in manufacturing, high-quality products with good surface finish and tight tolerances is a necessary but not sufficient condition. To keep pace with the high growth rate of the developing industry and the economy, it is also required to reduce the resources and increase the productivity. In order to ensure an efficient manufacturing line, the practice is to use environmentally hazardous chlorinated paraffin oils. By using these oils, not only the lubricant film breakdown, leading to scratching of the surfaces of the metal sheets, but otherwise required repolishing of the tools can be avoided, too. Thereby, financial and material resources can be reduced. At the same time, as a result of the growing awareness of environmental aspects and increasing legislations, some companies are substituting these oils with more environmentally friendly lubricants and/or tribo-systems. However, these attempts have been only partially successful, because the change in the tribo-system often results in a shift in the active lubrication mechanism. It is therefore the aim of this project to propose an off-line methodology on how to replace environmentally hazardous oils with environmentally friendly tribo-systems. While doing so, attention is also paid to numerical simulation of the lubrication in sheet metal forming operations by means of a newly proposed approach based on full coupling of fluid flow and metal flow.

In this project, an industrial case from the production line of Grundfos A/S was selected. The process concerns manufacturing of a stainless steel cup and includes thirteen stages consisting of multiple drawings and a final collar drawing and ironing operation. Lubricant breakdown occurs due to large reduction of wall thickness during the ironing operation. To start with, the production platform was analysed and the tribological parameters were identified. The methodology during the detailed analysis of the production includes experimental work in production, thermo-mechanical numerical calculations and validation of the results. The Strip Reduction Test (SRT) was selected as a suitable laboratory test to emulate the ironing operation in the production. A new SRT tool emulating both forward and backward strokes of the ironing operation has been designed and manufactured. The testing and the analyses of the entire SRT at room temperature as well as at elevated temperature were performed. After ensuring similar process conditions in the laboratory, selected tribo-systems were investigated. Additionally, enhancements for improving the current design were suggested and tested.

The proposed off-line methodology for industrial ironing operations was followed by a more fundamental research. The final part of the thesis focuses on understanding the behaviour of the fluids as pressure carriers in metal forming processes. For that, the finite element flow formulation, enabling strong coupling between metals and fluids, was adapted. Finally, the developed model was applied to thickness reduction testing of a sheet with mesoscopic surface pockets in order to investigate the mechanisms causing the escape of lubricants from the pockets.

Resume (in Danish)

For at være konkurrencedygtig i fremstillings- og produktionsbranchen er det nødvendigt at kunne lave produkter af høj kvalitet med god overfladefinish, men det er i sig selv ikke nok. For at følge med den hurtigt udviklende industri og økonomi er det også nødvendigt at reducere ressourceforbrug og øge produktiviteten. Det er praksis at anvende miljøskadelige, klorerede paraffinolier for at opretholde en effektiv produktionslinje. Ved at anvende disse olier reduceres smørefilmnedbrud som resulterer i rivninger på pladeoverfladerne. Ligeledes reduceres hyppigheden af nødvendig oppolering af værktøjerne. Derved forbedres økonomien, og materialeforbruget mindskes. Som et resultat af voksende bevidsthed om miljøhensyn og øget lovgivning, udskifter nogle virksomheder disse olier med mere miljøvenlige smøremidler og/eller tribosystemer. Disse anstrengelser har dog kun været delvist succesfulde, da en ændring af tribo-systemet ofte leder til ændringer i de aktive smøremekanismer. Formålet med dette projekt er derfor at udvikle en offline metodik til udskiftning af miljøskadelige olier med miljøvenlige tribo-systemer. Endvidere anvendes numerisk simulering af smøring i pladeformgivningsprocesser gennem en nyligt opstillet fremgangsmåde baseret på en fuld kobling af væske- og metalflow.

I dette projekt er et industrielt eksempel fra en produktionslinje hos

Grundfos A/S udvalgt. Processen vedrører fremstilling af en kop i rustfrit stål og indeholder 13 trin, herunder flere dybtræk og til slut et kraveoptræk samt en strækningsreduktion. Smørefilmnedbrud finder sted på grund af stor reduktion af en vægtykkelsen under strækningsreduktionen. Til at starte med blev produktionsplatformen analyseret, og de tribologiske parametre blev identificeret. Metodikken i den detaljerede analyse af produktionen inkluderer eksperimentelt arbejde, numeriske beregninger af det termomekaniske problem og validering af resultaterne. En stripreduktionstest (SRT) blev valgt som en passende laboratorietest til at efterligne strækningsreduktionen i produktionen. Et nyt SRT-værktøj, som simulerer stempelslaget inklusiv returslag, er konstrueret og fremstillet. Der er foretaget test og analyser af hele SRT'en ved både stuetemperatur og forhøjet temperatur. Efter at have sikret procesforhold i laboratoriet svarende til produktionen blev udvalgte tribo-systemer undersøgt. Ydermere blev forbedringer til konstruktionen foreslået og afprøvet.

Den foreslåede offline metodik for industriel strækningsreduktion blev efterfulgt af mere fundamental forskning. Den sidste del af afhandlingen fokuserer på forståelse af mekanismerne i en væske, der virker som trykbærer i metalformgivningsprocesser. Hertil blev finite element flowformuleringen anvendt, idet denne tillader en stærk kobling mellem metaller og væsker. Den udviklede model blev anvendt til simulering af tykkelsesreduktion af en plade med mesaskopiske smørelommer til undersøgelse af mekanismerne, der får smøremidlet til at undslippe fra lommerne.

Contents

Nomenclature and Abbreviations

Nomenclature

a	Lever arm	$[mm]$
a_i	Acceleration	$[mm/s^2]$
B	Strain rate matrix relating strain rates to nodal velocities	$[mm^{-1}]$
C	Matrix form of Kronecker delta	$[-]$
c	Speed of sound	$[mm/s]$
D	Diagonal matrix	$[Pa \cdot s]$
$\mathbf{D}_\mu$	Diagonal matrix of the lubricant	$[Pa \cdot s]$
E	Young's modulus	$[GPa]$
e_{AB}	Seebeck voltage	$[V]$
E_i	i'th edge	$[-]$
F	Load vector	$[N]$
F_d	Drawing force	$[N]$
g_i	Gravity acceleration	$[mm/s^2]$
H_{vap}	Enthalpy of vaporisation	$[kJ/mol]$
h	Heat transfer coefficient	$[W/(m^2K)]$
h	Height	$[mm]$

h	Local film thickness (in Chapter 8)	$[mm]$
h_m	Film thickness	$[mm]$
i	Iteration number	$[\,-\,]$
K	Penalty factor	$[MPa \cdot s]$
$\mathbf{K}$	Stiffness matrix	$[N \cdot s/mm]$
$\mathbf{K}_\mu$	Stiffness matrix of the lubricant	$[N \cdot s/mm]$
l	Contact length	$[mm]$
L_e	Element length	$[mm]$
M	Number of elements	$[\,-\,]$
$\mathbf{M}$	Mass matrix	$[kg]$
m	Friction factor	$[\,-\,]$
$\mathbf{N}$	Matrix of element shape functions	$[\,-\,]$
$\mathbf{n}$	Normal vector	$[\,-\,]$
n_j	Surface normal unit vector	$[\,-\,]$
$P_{1,2}$	Air pressure	$[Pa]$
p	Normal pressure	$[MPa]$
p	Hydrostatic pressure (in Chapter 8)	$[MPa]$
p_f	Sealing pressure in front of the pocket	$[MPa]$
p_{liq}	Lubricant pressure in the pocket	$[MPa]$
p_r	Sealing pressure at the rear end of the pocket	$[MPa]$
R	Tool radius	$[mm]$
R	Gas constant (in Appendix C)	$[J/mol \cdot K]$
R_a	Roughness parameter	$[\mu m]$
$\mathbf{R}$	Residual force vector	$[N]$
S	Surface	$[mm^2]$
s	Sliding length	$[mm]$
sfact	penalty scale factor	$[\,-\,]$
T	Torque	$[N \cdot m]$
$T_{1,2}$	Boiling temperature at pressure $P_{1,2}$	$[K]$
$\mathbf{T}$	Boundary surface traction matrix	$[MPa]$
T_A	Temperature of thermocouple A	$[^\circ C]$
T_{actual}	Calibrated temperature	$[^\circ C]$
T_B	Temperature of thermocouple B	$[^\circ C]$
T_{base}	Punch base temperature	$[^\circ C]$
$\mathrm{T}_{measured}$	Uncalibrated temperature	$[^\circ C]$
TC_i	*i*'th thermocouple and temperature	$[^\circ C]$
t	Time	$[s]$
t_i	Surface traction	$[MPa]$

$\mathbf{u}$	Vector of velocities	$[mm/s]$
u_i	Velocity	$[mm/s]$
V	Volume	$[mm^3]$
V_i	i'th vertex	$[-]$
v	Sliding (drawing) speed	$[mm/s]$
$\mathbf{v}$	Vector of nodal velocities	$[mm/s]$
w	Sheet width	$[mm]$
x	Calibration slope	$[-]$
x_j	Coordinate	$[mm]$
y	Calibration offset	$[-]$
α	Contact angle	$[^\circ]$
β	Pressure-viscosity coefficient	$[Pa^{-1}]$
δ_{ij}	Kronecker delta	$[-]$
ε_{ij}	Strain tensor	$[-]$
$\dot{\varepsilon}_{ij}$	Strain rate tensor	$[s^{-1}]$
$\dot{\varepsilon}'_{ij}$	Deviatoric strain rate tensor	$[s^{-1}]$
$\dot{\bar{\varepsilon}}$	Effective strain rate	$[s^{-1}]$
η	Kinematic viscosity	$[cSt]$
μ	Coefficient of friction	$[-]$
μ_s	Dynamic (shear) viscosity	$[Pa \cdot s]$
μ_v	Bulk viscosity	$[Pa \cdot s]$
ν	Poisson's ratio	$[-]$
Π	Energy rate	$[W]$
ρ	Structural density	$[g/cm^3]$
σ_{bt}	Back tension	$[MPa]$
σ_f	Yield stress	$[MPa]$
$\overline{\sigma}$	Effective stress	$[MPa]$
σ_{ij}	Stress tensor	$[MPa]$
σ'_{ij}	Deviatoric stress tensor	$[MPa]$
τ	Friction stress	$[MPa]$

Abbreviations

AHSS	Advanced High-Strength Steel
ALE	Arbitrary Lagrangian-Eulerian
BDC	Bottom Dead Centre
BUT	Bending Under Tension
CT	Computed Tomography
CVD	Chemical Vapour Deposition
DBT	Draw Bead Test
DLC	Diamond-Like Coating
DTU	Technical University of Denmark
EDM	Electrical Discharge Machining
EP	Extreme Pressure
FEM	Finite Element Method
HTC	Heat Transfer Coefficient
INN	Invariant Node Numbering
LOM	Light Optical Microscopy
MEK	Department of Mechanical Engineering
MPHDL	Micro Plasto HydroDynamic Lubrication
MPHSL	Micro Plato HydroStatic Lubrication
PM	Powder Metallurgical
PVD	Physical Vapour Deposition
RAP	Robot Assisted Polishing
RTD	Resistance Detector Thermometer
SEM	Scanning Electron Microscope
spm	stroke per minute
SRT	Strip Reduction Test
St_A	Station A
St_B	Station B
TDC	Top Dead Centre
UST1	Initial Universal Sheet Tribotester
UST2	New Universal Sheet Tribotester

CHAPTER 1

Introduction

As a science and art, metal forming goes back a long way. For more than 6000 years, humans have been smelting and forging copper to form tools and jewellery [1]. Considering the significance of the lubricants on metal forming processes, it is surprising that the lubrication technology has advanced only very recently. It is not more than 4000 years ago that oil-impregnated woods were used to slide building stones in Egypt [2]. Remains of two discovered ships showed that the Romans were using rolling bearings to support a wooden platform in the first century [3]. In spite of the different views among historians on the importance of the Middle Ages in terms of further developments in tribology, there is no doubt that the machinery used in the mediaeval period has been developed further to meet the tribological demands [4]. Thereafter, renaissance engineer and artist Leonardo da Vinci asserted a scientific approach to friction. Later, the industrial revolution brought with it metal-based machinery and accelerated the need for lubrication. In many cases, the use of chlorinated paraffin oil was the 'safest' method in industry to ensure good surface finish of the final part. However, in today's world of developing technology and increasing environmental awareness, the

trend is to replace the traditional oils with environmentally friendly ones.

This chapter introduces tribology in metal forming. A brief review of the literature in closely related topics such as lubrication mechanisms, simulative tests to emulate the process conditions in metal forming processes and the need for substituting hazardous oils in industry with environmentally friendly lubricants, is presented. Motivation derived from the state of the art and industrial needs is given and the objective of the project is presented. Finally, the outline of the remaining chapters is summarised.

1.1 State of the art

1.1.1 Fundamentals

Tribology plays a fundamental role in most metal forming processes. A lack of lubricant between contacting surfaces in relative motion that are usually sliding or rolling under load results in surface damage or removal of material. This phenomenon is known as wear. Wear is a system response and the primary types are adhesive wear, abrasive wear, corrosive wear and fatigue wear.

Adhesive wear occurs when so called asperities (surface bumps) in contact are sheared off during sliding. In such circumstances, particles from one surface come off and adhere to the other surface. Kayaba and Kato [5] described the detachment of the fragment mechanisms as plastic shearing of asperity contact layers. The overall mechanism is illustrated in Figure 1.1. They used slip-line fields and found that detachment of the layer is initiated with a shear crack resulting in a wedge-shaped fragment. The detached fragment adheres to the harder surface. Increased sliding causes more detachment of the layers.

During the process, adhered particles can either re-transfer to the softer surface or form loose wear particles [2]. In some cases, during adhesion

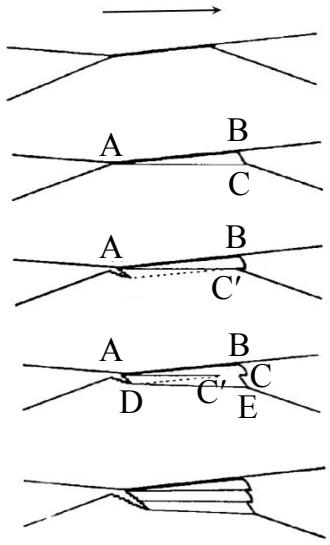

Figure 1.1: Illustration of the fragment detachment mechanism at the asperity contact [5].

and subsequent transfer, a work hardening of attached fragments may occur [6]. In severe cases, they may be cold-welded to one of the surfaces. As a consequence of materials being picked up on the harder surface, roughness increases and adhered particles lead to scoring of subsequent soft material surface upon further sliding. In metal forming, this problem is referred to as galling.

Abrasive wear is the cutting action of a hard, rough surface when sliding over a softer surface. In most of the abrasive wear cases, grooves parallel to the sliding direction are observed on the softer material surface [2]. Corrosive wear occurs when the sliding of the two bodies takes place in a corrosive environment and the protective oxide layer is worn off. Finally, fatigue wear is observed due to repetitive loading and unloading

cycles in sliding and rolling.

Lubricants are often used in order to enhance the tribological conditions. The functions that a metal forming lubricant must fulfill are as follows [1] :

- **Control friction.** Although very low friction is not always desirable, less friction leads to less power requirements and more homogeneous deformation.
- **Separate surfaces.** To prevent contact, lubricants must separate the tool and workpiece surfaces.
- **Minimise pick-up.** Breakdown of the lubricant or workpiece surface oxide causes adhesion, i.e. pick-up of the workpiece material on the tool surface.
- **Reduce wear.** During sliding, progressive loss of material is inevitable. Wear of the die and the workpiece surface is undesirable. It can be prevented by using a suitable lubricant.
- **Cooling.** A liquid lubricant may cool down the die and workpiece to prevent lubricant film breakdown and wear.

In addition to these main functions, protection of old and new surfaces, adaptability to varied working conditions, durability, stability, easy handling, safety and disposal are other important criteria that a lubricant must meet.

1.1.2 Lubrication mechanisms

Understanding of different lubrication mechanisms are important for further improvement of tribological techniques in metal forming. Lubrication mechanisms in metal forming may be listed as:

- Dry condition
- Solid film lubrication
- Boundary lubrication
- Mixed lubrication
- Hydrodynamic lubrication.

Illustrations of the above-mentioned lubrication mechanisms are given in Figure 1.2. The presented lubrication mechanisms are shown in the Stribeck curve, after [7], in Figure 1.3. The film thickness is determined by the applied normal pressure p, sliding speed v and lubricant viscosity η. The average film thickness and coefficient of friction for various lubrication mechanisms are function of these parameters. At lower normal

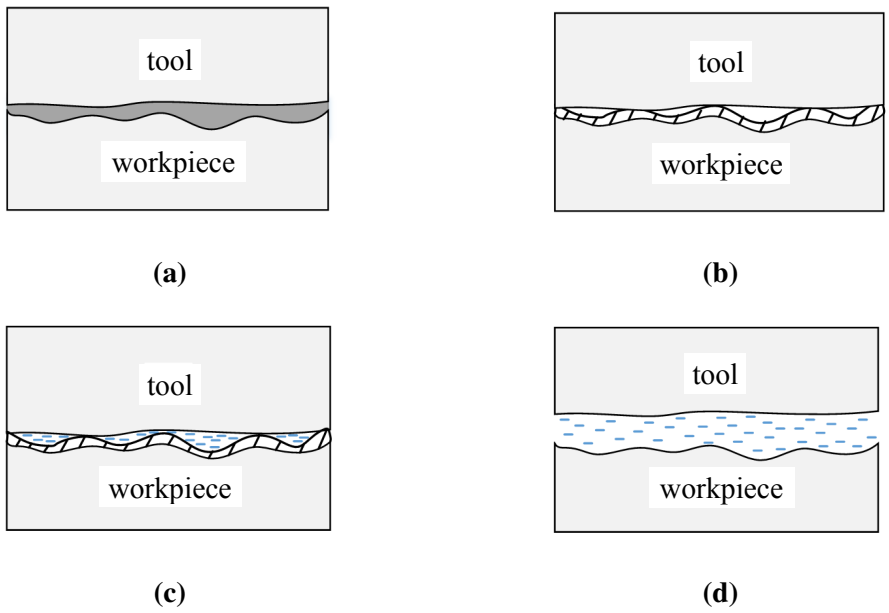

Figure 1.2: Illustration of lubrication mechanisms in metal forming: (a) solid film lubrication, (b) boundary lubrication, (c) mixed lubrication and (d) hydrodynamic lubrication.

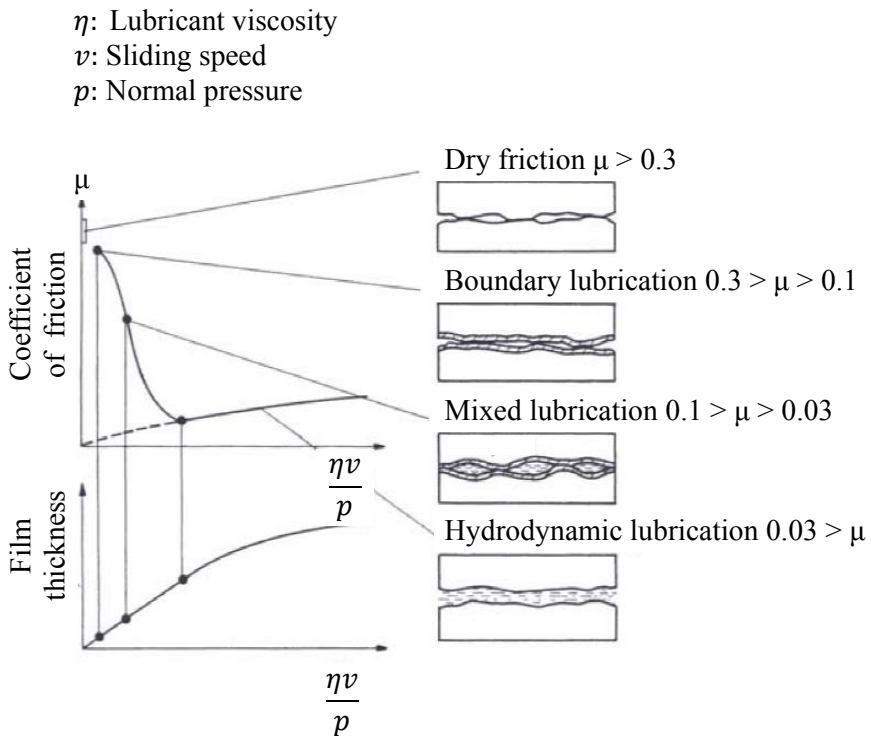

Figure 1.3: Coefficient of friction and average lubricant film thickness for various lubrication mechanisms [7].

pressure, when the viscosity and the speed are high enough, full separation between tool and workpiece surfaces through hydrodynamic lubrication can be assured, and the coefficient of friction is typically lower than 0.03 [7]. However, in metal forming, the contact pressures are often high. For lower ratios of $\eta v/p$, the lubricant film thickness decreases. As a result, complete separation cannot be achieved, asperity contact takes place and the friction coefficient increases above 0.03 [7].

The principles of different lubrication mechanisms, with focus on boundary lubrication and mixed lubrication that are often observed in metal forming applications, are described in the following.

Dry condition

In dry condition, no lubricant at the interacting surfaces is used. This condition corresponds therefore to high friction. It is common for a few metal forming processes such as air bending where the friction does not affect the quality of the workpiece significantly [7]. In spite of high friction, in a couple of forming processes as for instance hot rolling of slabs and plates, the dry condition may be desirable.

Solid film lubrication

In solid film lubrication, a contaminant film prevents metal-to-metal contact (see Figure 1.2a) and reduces the friction by having low shear strength. The film can be attached either on the workpiece or on the tool surface or even on both of them. The attachment may occur mechanically, by a chemical reaction or a physical adsorption. Metal films such as Zn, Pb, Cu, Ag and Au, oxide films, polymer films and graphite films are examples of solid-film lubricants [8].

Boundary lubrication

The foundation of boundary lubrication is primarily based on the investigations done by Hardy and Doubleday [9] in the early 1920s. They found thin films adhering to surfaces under sliding and introduced the term "boundary lubrication" [10].

Figure 1.2b illustrates pure boundary lubrication. Metal-to-metal contact is avoided by one or a few molecular thick lubricant layer. The boundary films can be formed by either chemical reaction, chemical adsorption or physical adsorption (see Figure 1.4).

Physically adsorbed boundary lubrication is characterised by weakly bonded, reversible molecular layer(s). Figure 1.4a is a schematical diagram of a physically adsorbed boundary lubrication on a metal surface. Layers can be either monolayer or multilayer. Figure 1.4b represents an example of chemical adsorption of stearic acid on an iron surface. In chemiadsorbed films, molecules are first adsorbed physically

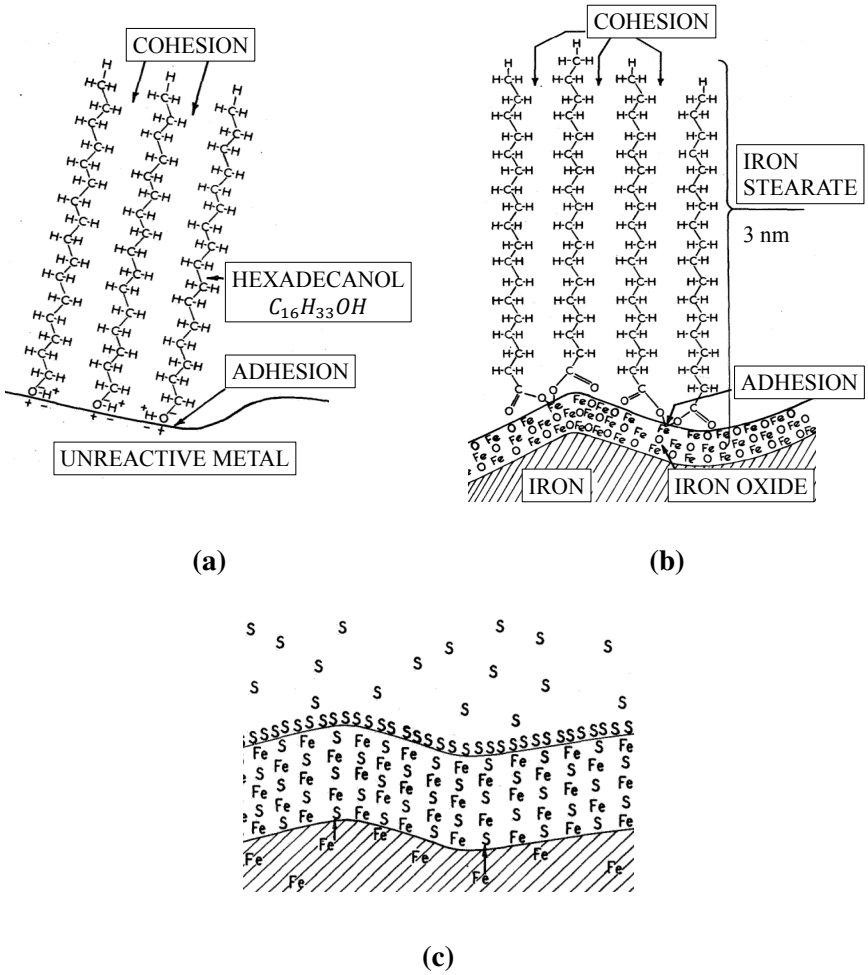

Figure 1.4: Schematical diagram of (a) physical adsorption of three polar hexadecanol molecules on a metal surface, (b) chemical adsorption of stearic acid on an iron surface to form iron stearate soap and (c) chemical reaction of sulfur on an iron surface to form iron sulfide [11].

and then reacted chemically. Boundary lubrication is limited to monolayers. Compared to physically adsorbed layers, chemically adsorbed layers are bonded stronger and they are irreversible. Chemical reaction is referred as formation of films of inorganic salts that have high acti-

vation energy and are irreversible. Figure 1.4c shows the reaction of sulphur with iron to form iron sulfide [1].

The chemical composition of the lubricant, the underlying metal and the process temperature are all in interaction with each other and affect the formation of boundary lubrication [9]. The shape of the molecules is another important factor. Rather than ring or branch chain molecules, straight chain molecules such as alcohols and soaps of fatty acids provide formation of thick, dense films with their polar ends [2]. Furthermore, orientation of the film also has influence on the efficiency of the boundary lubrication in such a way that a decreasing degree of orientation of the molecules indicates worse efficiency as a boundary lubricant [12]. Bulk properties of the lubricant, on the other hand, such as the viscosity, are less significant [1].

In boundary lubrication, a monomolecular layer is enough to reduce friction. However, increased number of layers provide lower friction and, as a result, longer durability under relative motion. Shear stress for defined sliding using various molecular layers has been previously tested and it was found that shear stress increases with decreased number of layers [13]. Moreover, the chain length of carbon atoms, or molecular weight of the lubricants in case of paraffins, alcohols and fatty acids, affects the friction [14]. A temperature rise, on the other hand, causes instability of the layers and disorientation. At a critical temperature, friction increases. If the temperature increases further, the solid film melts. The critical temperature of the lubricant, in other words the transition temperature, depends on the solid surface and the film agent. Figure 1.5 illustrates the transition temperature and melting point of fatty acids as a function of the number of carbon atoms in fatty acid chains. Lubricants based on fatty acids have a transition temperature, i.e. they are efficient up to about 40 °C to 70 °C above their melting points [14]. The actual value of breakdown temperature changes with the sliding speed, load and the nature of the underlying materials [2].

The stability of a film layer also depends on how it is formed. In general, chemical reaction films have better performance, whereas physically ad-

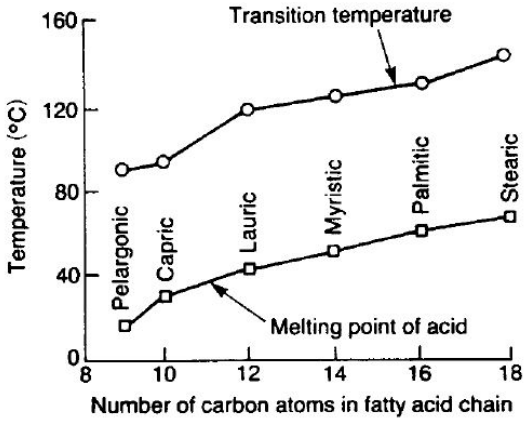

Figure 1.5: Transition temperature and melting points of fatty acids as a function of chain length [14].

sorbed films are the poorest in terms of stability [2].

Fluid film lubrication

In this type of lubrication, full separation between the tool and workpiece is ensured by fluid. Contrary to boundary lubrication, in fluid film lubrication friction and wear depend on the bulk properties of the lubricant, whereas the chemical interaction between the lubricant and the workpiece is less important.

In case the local elastic deformation around the asperities affect the lubrication regime, it is called an ElastoHydrodynamic lubrication. The film thickness is typically less than in hydrodynamic lubrication. On the Stribeck curve (Figure 1.3), it lies between hydrodynamic lubrication and mixed lubrication.

Mixed lubrication

In most of the metal forming processes, the film thickness is not sufficient to prevent metal-to-metal contact and some asperity contacts are generated. In the mixed lubrication regime, the interface pressure is carried partly by the pressurized lubricant in the surface valleys and partly

by the asperity contacts. Inspired by Bay and Wanheim [15], the mixed lubrication regime can be described under four subsections:

- Hydrodynamic lubrication – asperity contact
- Hydrodynamic lubrication – boundary lubrication
- Hydrostatic lubrication – boundary lubrication
- Micro Plasto HydroStatic lubrication – Micro Plasto HydroDynamic lubrication.

Hydrodynamic lubrication – asperity contact. This lubrication regime is the transition between hydrodynamic lubrication and asperity contact during which the load is still carried by the lubricant. The first contact between asperities and the resulting entrapment of the lubricant are greatly influenced by the viscosity of the lubricant, the relative velocity between moving surfaces and the surface topography of the workpiece and the tool [15].

Butler performed several experiments to show the role of the lubricant viscosity in the matching of the surfaces during bulk metal forming processes. Using no lubricant or less-viscous lubricants result in near-full contact between the workpiece and the tool, whereas a high-viscous lubricant limits the contact [16] [17]. In addition to the effect of viscosity, Wanheim [18], Azushima [19], Reid and Schey [20] and Lu and Chuang [21] studied the influence of surface topography on the determination of the active mechanism. They have pointed out that not only the degree of surface roughness, but also the rolling direction of the strip surface has crucial importance. A surface lay parallel to the sliding direction facilitates lubrication escape, leading to more metal-to-metal contact and consequently higher friction, whereas surfaces with perpendicular directionality improve entrapment of the lubricant and decrease friction.

In spite of various empirical investigations, theoretical analysis of viscous flow and entrapment of lubricants during the initial contact is highly complex and requires further theoretical and experimental research.

Hydrodynamic lubrication – boundary lubrication. In the combined hydrodynamic and boundary lubrication regime, the load is carried partly by the boundary lubricants on the asperities which prevents pick-up on the tool surface. The film thickness is smaller than the averaged sum of the roughness, the valleys between contact areas are interconnected to each other [22].

Detailed theoretical analysis on this mechanism in cold rolling was carried out by Tsao and Sargent [23]. They developed an isothermal model that takes into account both the hydrodynamic lubrication and the asperity contact. The developed mixed lubrication theory assumes a Gaussian distribution of the asperity height with a spherical top, which is in reality far from that assumption. Although the amount of asperity contact and its effect on the friction level were estimated, they did not take into account the supported load at asperity contacts. The plastic deformation of the workpiece would also lead to changes in the roughness. Sheu and Wilson [24] developed a more detailed analytical model taking into account the contribution of the asperity contact to support the load. They used Patir and Cheng's [25] thin film lubrication theory to determine the influence of roughness on the flow and combined it with Wilson and Sheu's [26] asperity flattening model for determination of the influence of bulk deformation on asperity hardness. Thermal effect was also included by an approximate correlation.

Hydrostatic lubrication – boundary lubrication. In the hydrostatic lubrication regime, the load is carried partly by the hydrostatic pressure generated in the surface pockets and partly by the asperity contacts or the boundary lubricant layer.

Lancaster and Rowe [27] studied the effect of a trapped lubricant. They performed drawing experiments using boundary lubricants under a light and a heavy load. They observed that the boundary film broke down, resulting in pick-up on the tool. To prevent this, they suggested to produce pockets on the workpiece by grit-blasting. It was shown that strips with grit-blasted surfaces could be reduced up to 60 % in thickness without pick-up, whereas the value was 15 % for polished surfaces.

The load-carrying capacity of the lubricant in surface pockets was emphasised by Wanheim [18]. He showed that at high pressures the hydrostatic pressure in the trapped lubricant has a great importance on the real contact area. Depending on the lubricant's compressibility, the real contact area and resulting friction force vary. Kudo [28] performed an analytical calculation of the friction coefficient to examine the role of trapped lubricants in pockets. He used the slip-line field theory to determine the contact pressure with an assumption of a constant bulk modulus of the lubricant. He found that for a given shear stress to shear yield stress ratio, the coefficient of friction decreases with increasing lubricant bulk modulus. Nellemann et al. [29] analysed the real contact area in plane strain deformation with lubricant entrapment taking pressure sensitivity of the lubricant bulk modulus into account. They found that the asperity slope and friction factor have minor importance on the real area of contact compared to normal pressure and lubricant bulk modulus. However, the analytical models in these studies in the 1960s and 1970s did not consider the lubricant escape from the pockets.

Micro Plasto HydroStatic lubrication – Micro Plasto HydroDynamic lubrication. In the early 1980s, a second lubrication mechanism connected to the lubricant entrapment was discovered. At first, Mizuno and Okamato [30] proposed the escape of entrapped lubricants from pockets in order to better understand the interaction between tool and workpiece. They performed a compression-friction test to study the dependency of the surface roughness and lubrication condition on the viscosity and sliding speed. They stated that the lubrication mechanism changes according to the product of the viscosity and sliding speed, ηv. As ηv increases, lubricant escapes from the pocket and penetrates into the contact area forming a thin hydrodynamic film as illustrated in Figure 1.6. In this case, the overall friction does not depend on the boundary film properties but on the bulk properties of the lubricant.

The phenomenon of lubricant escape was confirmed by other researchers [31]. It was later experimentally studied by Azushima et al. [32]. They developed a strip drawing apparatus including a CCD-camera and a transparent die showing that the lubricant is squeezed out from the surface

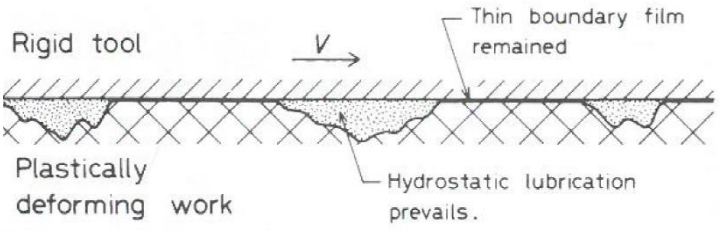

(a)

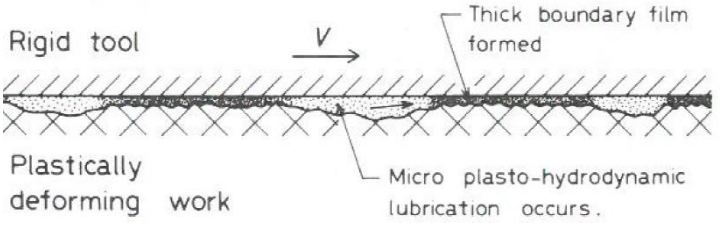

(b)

Figure 1.6: Illustration of (a) a lubricant in the pocket when the the product of the viscosity and sliding speed ηv is low and (b) a lubricant escape when ηv is high. [30].

pockets of the strip during drawing. The speed dependence was investigated and it was found that the friction coefficient increases with drawing speed in the range of 10-200 mm/s [33]. The degree of reduction and the lubricant viscosity are other factors affecting lubricant escape. Using the same set-up, pressure dependency of the coefficient of friction was investigated [34]. It was found that at low pressure, the coefficient of friction is constant, and the lubrication regime is characterised by boundary lubrication. At medium pressure, the coefficient of friction decreases, and the regime is characterised by hydrostatic pressure. Further increase in pressure leads to a lower coefficient of friction due to lubricant escape into the contact areas.

The standardisation and the definition of the terms used for this sec-

ondary lubrication mechanism can be formulated as follows. During deformation, the pressure in the pocket is less than the pressure on the workpiece material surrounding the pocket. Figure 1.7a shows a schematical representation of the Micro Plasto HydroStatic Lubrication (MPHSL) mechanism in which the forward escape of the lubricant occurs when the lubricant pressure p_{liq} in the pocket exceeds the sealing pressure p_f in front of the pocket. Alternatively, Figure 1.7b presents the Micro Plasto HydroDynamic Lubrication (MPHDL) mechanism in which backward escape occurs when the viscous drag of the lubricant creates a liquid pressure p_{liq} at the rear end of the pocket that reaches the sealing pressure p_r at the back of the pocket.

Bech et al. [35] and Shimizu et al. [36] used an experimental set-up

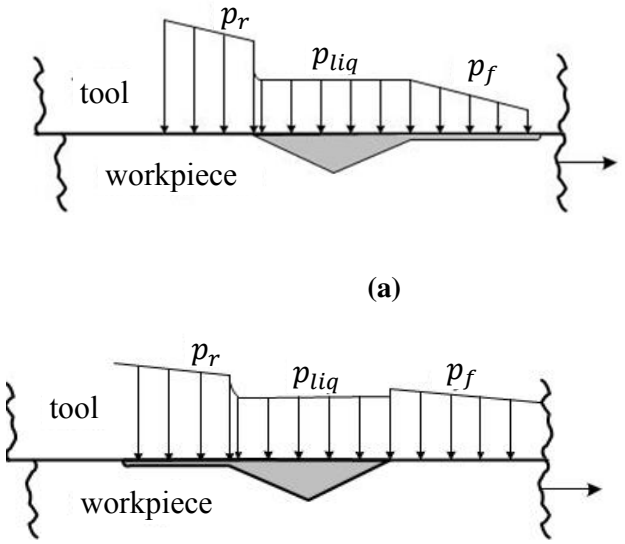

Figure 1.7: Schematical representation of the two mechanisms of lubricant escape: (a) Micro Plasto HydroStatic Lubrication (MPHSL) and (b) Micro Plasto HydroDynamic Lubrication (MPHDL).

similar to Azushima et al.'s set-up [32] and investigated the pocket geometry, drawing speed and lubricant viscosity, among other parameters, on the escape of entrapped lubricants. Experimental results revealed that the MPHDL mechanism is likely to occur at increased lubricant viscosity and drawing speed, whereas MPHSL is initiated at larger lower die friction. They also established an analytical framework capable of modelling the influence of these parameters on the pressure build-up and lubricant escape. Similar work was performed by Lo and Wilson [37]. More recently, Azushima et al. [38] studied pressure build-up and lubricant escape from a central pocket in upsetting test by means of a rigid plastic finite element analysis.

1.1.3 Lubricants

In industry, lubricant selection is mostly based on requirements of a good surface finish of the final part and long tool life. However, the relationship between the lubricant, the environment and the process is complex. During the last decades, realisation of this complexity and increasing environmental awareness have resulted in the development of various new lubricants. Although it is beyond the scope of this subsection to introduce all types of lubricants, it is the aim to give a short overview. Classification of several lubricants in this subsection is mainly based on the activated lubrication mechanism and functional aspects.

Hydrodynamic lubricants

Mineral oils are applied for hydrodynamic lubrication. They are produced from crude oil by distillation and other processes. They are basicaly hydrocarbons with various distributions of paraffinic, aromatic and naphthenic components. Properties such as viscosity, viscosity-temperature-pressure relationships and performance characteristics are determined by these components [1].

Paraffin oil, with straight or branched carbon atoms, is widely used as a

hydrodynamic lubricant carriers in metal forming. Typically, viscosity of paraffin decreases less rapidly with increased temperature, and it has low resistance to oxidation compared to aromatic and naphthenic components [1].

Synthetic oils, formed by long-chain hydrocarbons, are other examples of hydrodynamic lubricants. They are specifically developed for applications under extreme temperatures and pressures. In spite of better performance, they are more expensive than mineral oils. Some of the synthetic oils are synthetic hydrocarbons, chlorinated hydrocarbons, esters, silicones and polyphenyl ethers [2].

Boundary lubricants

Natural oils, fats and derivatives provide molecular layer protection between sliding surfaces and are listed as examples on boundary lubricants. These lubricants are derived from vegetable and animal sources and contain fatty acids, which are effective boundary lubricants used in metal forming industry [1]. When a fatty acid reacts with the oxides on the workpiece surface, metal soap is formed. Metal soap is chemically bonded to the surface and used for boundary lubrication or solid film lubrication. Fats and soaps are especially suitable for low-speed applications [8].

Lamellar solids

Some of the solid lubricants such as graphite and molybdenum disulfide (MoS_2) are lamellarly structured and therefore referred as lamellar lubricants. The atoms are strongly bonded within each layer, whereas the layers are weakly bonded to each other.

Compound lubricants

Most of the hydrodynamic lubricants fail under severe process conditions in metal forming applications. In order to improve the load-carrying capacity of the lubricants under high pressure and temperatures, Extreme Pressure (EP) additives are often added to mineral or synthetic oils. Chlorine, sulphur and phosphorus compounds or their combinations are the most common EP additives. EP additives generate a layer in the form of boundary lubrication with a chemical reaction depending on the interface temperature. The range of effectiveness of EP additives are: up to 205 °C for phosphorus, between 205-700 °C for chlorine and between 700-960 °C for sulphur [7]. When the tribological conditions are so severe that EP additives are not sufficient, lamellar solid additives may be applied. However, removal of these lubricants and the black colour is often an undesirable issue. Soaps and fats may as well be compounded with EP additives.

Coatings

Metal coatings such as zinc, lead and copper combined with non-metallic lubricants were previously applied in cold and warm forming. Today, this lubrication method is very rare [8].

Polymer coatings have the advantage of being formed with substrate material due to their ductility. However, low heat conductivity may not be desirable for the applications when removal of heat is critical.

During hot forming, oxide layers may be formed providing separation between the workpiece and tool. However, depending on the thickness, additional lubrication and materials, the oxide layers may not always be desirable.

Conversion coatings are another type of coating, where an adherent layer from the part of surface is produced by chemical or electrochemical processes. They act as separating agents and lubricant carriers. Typical conversion coatings are oxalate for stainless steel, phosphate for steel and aluminate coatings for aluminium.

Emulsions

In metal forming, it is sometimes necessary to provide oil-in-water. Such a mixture takes advantage of the lubricity of the oil, while the water functions as a heat sink and limits the temperature increase. Emulsions have been used for many years in metal rolling applications [39].

1.1.4 Simulative testing in sheet metal forming tribology

In sheet metal forming applications, friction and lubrication are important. They influence metal flow, temperature distribution, surface quality and tool wear, as well as other properties. With the developments in the metal forming industry, both the materials and processes have advanced. In order to form tribologically difficult materials that are in demand in industry, severe sheet metal forming process conditions are often encountered. Systematical testing of limits of lubrication for various tribowindows is therefore crucial to correspond the industrial demand.

Bay et al. [40] classified the tribological tests in metal forming in two subgroups, namely process tests and simulative tests. Process tests can be applied directly to typical metal forming processes. However, in many metal forming applications, simulative tests are used to model tribological conditions. Simulative tests provide flexibility in variation of parameters. Process parameters such as sliding length, sliding speed, normal pressure, tool temperature as well as the material and surface properties of the workpiece and the tool can be controlled to emulate the industrial process conditions. Such a test set-up enables the control of each parameter and provides the possibility of studying several tribowindows for the actual processes. In both process and simulative tests, direct testing, i.e. the direct measurement of the friction stresses, can be used. Although it is practical, it may be difficult to apply to all processes. In such cases, indirect testing can be utilised. In indirect testing,

measurements are combined with a numerical analysis under controlled conditions. A more comprehensive study of tribological test methods and measurement techniques can be found in literature with emphasis on bulk metal forming [40], sheet metal forming [41] [42] and both [1] [43]. The focus in this subsection is on simulative tests in sheet metal forming.

Figure 1.8 shows a number of simulative tests used in sheet metal forming applications. The tribological conditions in the flange area can be studied using 1. Strip drawing test, 2. Draw bead test and 3. Drawing with tangential compression. The bending under tension test, number 4, emulates the process conditions at the die curvature and 5. Bending

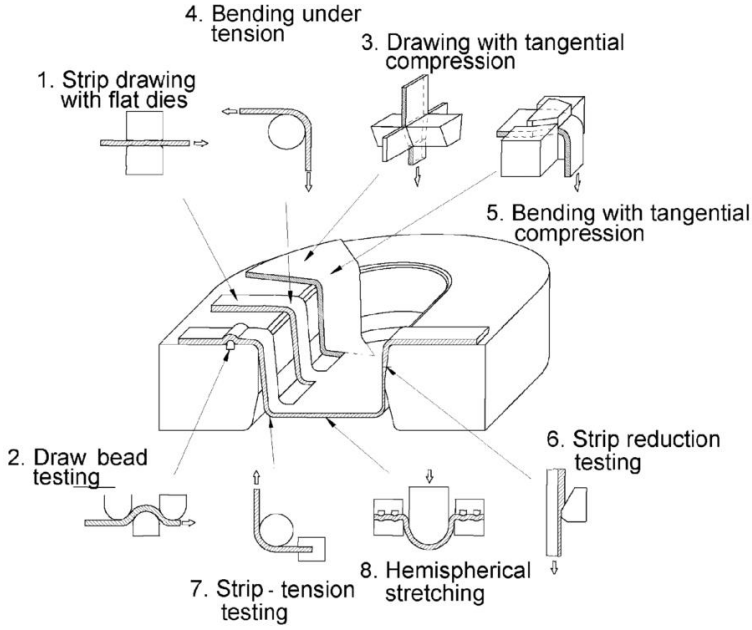

Figure 1.8: Illustration of simulative tests used in sheet metal forming processes [41].

with tangential compression combines the conditions both in the flange and die curvature. In the case of ironing, the wall thickness reduction is emulated by strip reduction test, number 6. The conditions along the punch corner radius is analysed by 7. Strip tension testing and finally, test number 8, hemispherical stretching, may be used for investigations under the punch.

At the Technical University of Denmark (DTU), Department of Mechanical Engineering (MEK), Bay et al. developed the test numbers 1, 3-5 [44] [45], number 2 [46] and number 6 [47] by using the Universal Sheet Tribotester (UST1), which was designed by Lassen and Bay in 1991 (see Figure 1.9). UST1 has a maximum sliding length of 300 mm and a sliding speed of 150 mm/s. Test tools developed to emulate several process conditions can be implemented in UST1 and desired simulative tests can be performed. However, the main drawback of UST1 is the lack of possibility of running multiple consecutive strokes. Due to a high production

Figure 1.9: Photo of the initially developed Universal Sheet Tribotester (UST1).

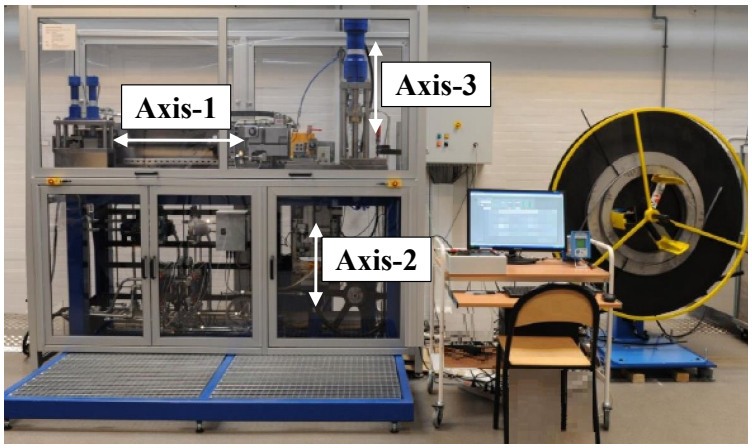

Figure 1.10: Photo of the new Universal Sheet Tribotester (UST2).

rate in industry and its effect on the critical tribo-parameters, DTU-MEK decided to develop a more sophisticated tribotester.

The new Universal Sheet Tribotester (UST2) is shown in Figure 1.10. It was designed by the engineering consultancy company IPU, situated at DTU, and built in 2012.

UTS2 enables the running of repeated tests to emulate progressive forming. Some features of the new tribotester are listed below:

- Possibility of running several simulative tests
- Automatic feeding of the strip
- Automatic cutting of the strip
- Automatic lubrication system
- Running the test with LabVIEW software
- Running the test in manual mode

- Accurate control of position and speed
- Possibility of measuring force on every axis.

More detailed information on design, construction and units of UST2 is discussed elsewhere [48].

Among the simulative tests given in Figure 1.8, the ones selected by DTU-MEK for further investigation were Bending Under Tension test, Draw Bead Test and Strip Reduction Test. These tests are described in the following.

Bending Under Tension (BUT) test

The BUT test is a simulative test where the conditions along the die curvature in deep drawing is emulated. Together with draw bead and strip drawing tests, Schey and McLean [49] performed the BUT test to evaluate sheet metal forming lubricants. Saha and Wilson [50] applied several tool coatings and process conditions such as process speed, contact pressure and lubrication and found the best tribo-system giving the lowest friction coefficient by adopting BUT test. The effect of textured tool surfaces [51], sheet surface topography [52], sheet surface coatings [53] [54] and die materials [55] on the evaluation of tribological characteristics in sheet metal forming using BUT tests have been investigated by many researchers for decades. The traditional way of performing the BUT test consists of two steps: drawing over a stationary die and drawing over a rotating die. Friction is calculated from the difference in the front tension obtained from the above-mentioned two steps. However, the set-up requires a steady system for an accurate calculation.

At DTU-MEK, a BUT test tool was designed with inspiration from Weinmann's design [56]. The main components of the BUT equipment is illustrated in Figure 1.11 [45]. The design enables measuring of the front tension, back tension and the torque on the tool pin. The tool was tested in UST1 and it was shown that an increase in the torque can be related to galling.

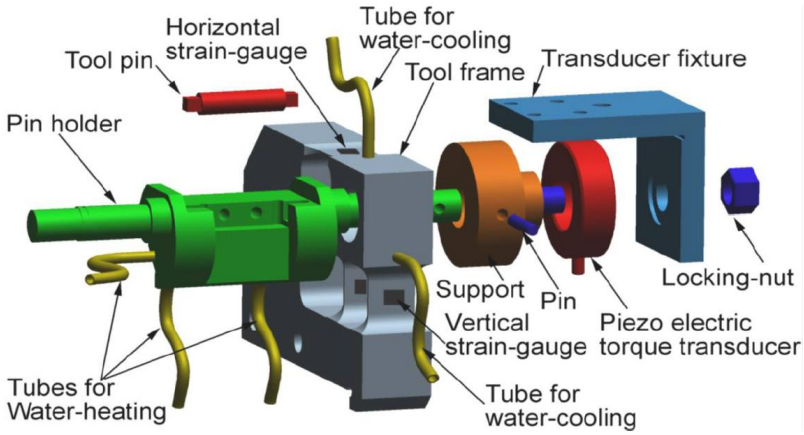

Figure 1.11: Illustration of the Bending Under Tension (BUT) equipment [45].

Ceron and Bay [57] implemented a developed variant of the tool pin into UST2 and claimed that determination of the coefficient of friction combined with an analytical solution can lead to errors due to non-constant contact pressure during the experiment. Later, they developed a methodology for off-line testing of several tribo-systems by means of BUT using UST2 [58] [59].

Draw Bead Test (DBT)

The DBT is used to evaluate the tribological conditions at the flange where the draw beads are used during deep drawing. An illustration of the DBT is given in Figure 1.12.

A comparative study on various sheet materials, tool materials, coatings and lubricants [60] [61], textured sheet surfaces [62] and speed effects in DBT [63] have been reported in literature. Moreover, analytical and numerical modelling of DBTs have been proposed [64] [65]. Groche and Christiany [66] studied wear and wear development of various tool materials and conducted experiments with a machine that can run auto-

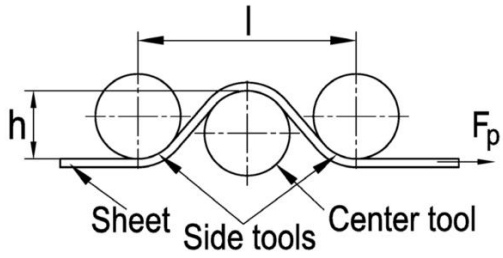

Figure 1.12: Schematical drawing of Draw Bead Test (DBT) [46].

matically for multiple strokes. The tribotester is located at the Institute for Production Engineering and Forming Machines at the University of Darmstadt and has been used also for other simulative tests such as strip drawing test with bending around a drawing edge [67].

Furthermore, a brief literature review indicates that, similiar to the BUT, in DBT it is necessary to perform two experiments, with a stationary tool and with a rotary tool, for determination of friction. The control of the system is therefore critical to maintain the inaccuracy at minimum [68] [69]. Olsson et al. [46] proposed to use a torque transducer for direct measurement of the friction instead. They implemented the tool in UST1 and showed that the sensitive measurement of torque provides an accurate determination of the onset of lubricant film breakdown.

Strip Reduction Test (SRT)

Among sheet metal forming processes, ironing is considered as one of the most severe due to the occurrence of high, localised pressures and large surface expansion. A schematical drawing of industrial ironing of a drawn collar is given in Figure 1.13. The main reduction of the wall occurs during the forward stroke, while during the backward stroke, elastic contraction of the die contributes an additional reduction. The combination of high, localised pressures and stretching of the lubricant film along the tool/workpiece contact interface may give rise to lubricant breakdown, pick-up and galling, resulting in a poor surface finish and high manufacturing costs due to the necessity of repolishing or replacing

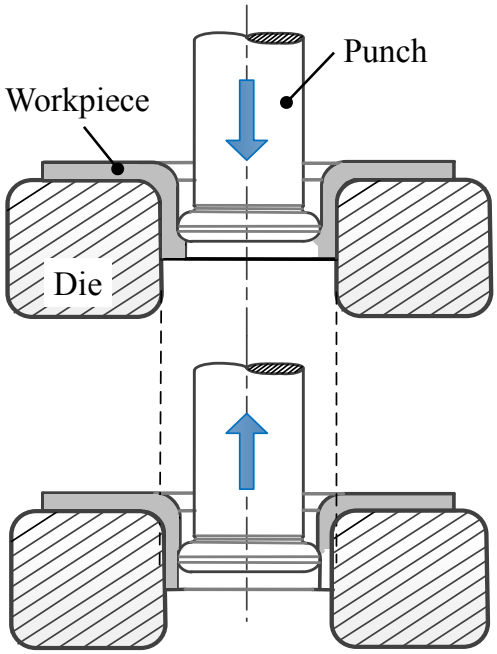

Figure 1.13: Schematical drawing of the ironing process during forward and backward strokes.

the active tool parts.

The SRT is a simulative test in which the process conditions of ironing can be replicated by reducing the thickness of a plane sheet strip. One of the first experimental set-ups for this purpose was developed by Fukui et al. [70]. They performed direct measurements of the friction force during the drawing of a strip, while the strip was reduced between two stationary dies. Dohda and Kawai [71] proposed an alternative design consisting of a bottom plate that is drawn together with the strip through a wedge-shaped ironing die. Andreasen and Bay [47] [72] introduced a new design that makes use of a circular tool pin, which is easy to polish, and furthermore, the design has the advantage of using the same tool four times before repolishing by rotating it 90°. More recently, Aleksandrović at al. [73] proposed a new set-up in which the strip is reduced from both

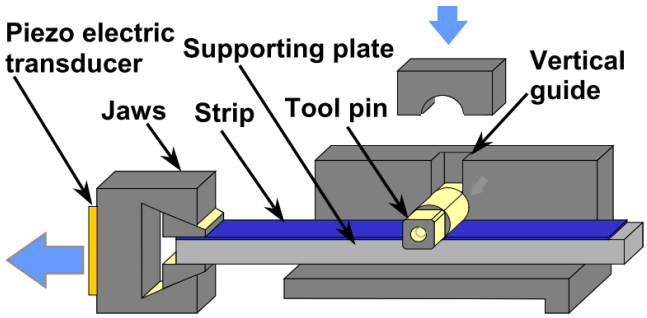

Figure 1.14: Illustration of the initially developed Strip Reduction Test (SRT) equipment [74].

sides through a wedge-shaped die.

The initially developed SRT equipment at DTU is shown in Figure 1.14. The strip is placed on a supporting plate and both are fixed in a jaw. The cylindrical tool is placed on top of the strip and loaded towards a solid stop to obtain a defined reduction. The load is maintained on the reduction tool while the lower plate and strip are pulled at a constant speed.

Using the design presented above, Andreasen et al. [47] investigated the influence of reduction and tool rest temperature on the onset of pick-up for various lubricants. The threshold sliding length before onset of lubricant film breakdown was defined by a certain number of scratches on the strip surface. A more detailed quantitative analysis was performed later [75]. Quantification of galling was determined by surface roughness analysis taken from equidistant intervals along the drawn sheet surface. Based on the measurements, the amplitude roughness parameter R_a and valleys deeper than 1 μm were used as two basic quantitative criteria for determining threshold sliding length. Threshold sliding length was defined as follows: *"If a profile taken at a given sliding length s has more than one significant deep valley (deeper than 1 micrometer) and the following profile has even more significant valleys than the profile*

at s, then the threshold sliding lentgh is s." [76]. The authors investigated several lubricants at the same reduction and temperature. Furthermore, the influence of tool topography and tool coatings were tested. In a further study, 3D roughness mapping of local areas were proposed for the determination of the limits of lubrication [77]. Olsson et al. [74] [78] combined experimental and numerical analysis to determine friction and interface temperature in SRT. They used reverse analysis and determined the friction factor by matching the calculated and measured drawing forces. Similarly, the heat transfer coefficient was found by fitting calculated and measured temperatures.

Later, using the initially developed SRT set-up, Wadman et al. [79] worked with lean duplex and austenitic steel and investigated the effect of surface texture on galling characteristics. Recently, an acoustic emission measuring technique has been developed and implemented in the SRT [80]. Preliminary investigations show promising results relating the severity of galling with generated acoustic emission parameters.

1.1.5 Environmentally benign tribo-systems

In a sheet metal forming production line, the surface quality of the final part and tool life depend significantly on the lubricant performance. Hazardous chlorinated paraffin oils have been widely used by manufacturers throughout the world for many decades. However, with increasing legislative restrictions and growing environmental awareness, the trend is to substitute environmentally hazardous oils with environmentally friendly lubricants [81].

Since 2006 the European Parliament has passed several regulations concerning the registration, evaluation, authorisation and restriction of chemicals [82]. Within the scope of these regulations, certain types of chemicals are either limited in use or restricted. In the United States, the National Institute for Occupational Safety and Health published a crite-

ria document to investigate the health effects of the metalworking fluids and to provide recommendations to overcome related hazards [83].

Parallel to the regulations and growing awareness, several research activities at DTU-MEK have been performed since 1993: an industrial research programme about *Development and testing of environmentally friendly lubricants for sheet metal forming of stainless steel and other sheet metals* ran until 2004 and a framework programme called *Development of new, environmentally acceptable lubricants, tribological tests and models for European sheet forming industry, ENLUB* went on from 2002 to 2006. Most recently, an ongoing research project on *New environmentally benign sheet metal forming tribology systems, SHETRIB* has been running since 2014 and new, environmentally friendly tribo-systems for sheet metal forming applications have been investigated.

Comprehensive reviews of the trends and alternative tribo-systems have been published previously [81] [84]. A way to substitute hazardous lubricants may be to adapt the anti-seizure tool materials. Azushima et al. [85] studied the effects of carbide controlled tool steels in cold rolling of C-steel. They have found a strong correlation between the mean carbide spacing on the rolling tool and the onset of galling [86]. Uddeholm Tooling AB designed a new Powder Metallurgical (PM) cold-work tool steel, Vancron 40, with improved anti-galling properties [87]. Later, the PM tool steel Vanadis 4 has also been improved in terms of thermal properties and commonly used in metal forming. Ceramic materials are also well-known for their high wear resistance and anti-galling properties. Kataoka et al. [88] studied dry deep drawing with various ceramic tools and strip materials. In addition to their claim that only certain tools with specific strip materials such as zinc-coated steel with a SiC tool shows successful results, they reported difficulties in machining the ceramic tool and proposed an electroconductive ceramic tooling manufactured by Electrical Discharge Machining (EDM) [89] [90].

Another alternative to avoid application of hazardous lubricants is the adaptation of anti-seizure tool surface coatings that can be applied by Physical Vapour Deposition (PVD) or by Chemical Vapour Deposition

(CVD). Kim et al. [91] have tested CrN, XNP and TiCN PVD-coated tools in a combined strip drawing and ironing test. They used uncoated as well as galvanized AHSS and found that TiCN is the most efficient coating in terms of preventing galling. Klocke et al. [92] claimed that application of a graded zirconium carbide PVD tool coating allows chlorinated paraffin oil to be replaced by a new environmentally benign lubricant, HIGTO, when deep drawing of stainless steel AISI 304 sheets is performed.

For more than two decades, application of hard Diamond-Like Coatings (DLC) on the tool surface to perform stamping operations under dry conditions has been studied extensively. One of the first applications of DLC coatings in stamping operations was developed by Murakawa et al. [93]. A DLC coating was applied on a WC-Co deep drawing die and it was shown that the tool, compared to TiCN- or CrN-coated tools, lasted longer. The increase in durability was obtained by avoiding adhesion of the sheet material to the die surface. Yet, the drawback of a DLC coating is its low adhesion strength to the tool. This results in peeling off of the coating, especially under severe conditions such as high tool/workpiece interface pressure and elevated temperature. An alternative solution to prolong the coating life is to apply a multi-layer structure coating instead of nano-lamination [94]. The multi-layer coating structure and the thickness of each layer can be adjusted to optimise the hardness, load-carrying capacity and adhesion between the DLC coating and the tool [95].

At DTU-MEK, three DLC coating structures have been investigated recently [96]. These were the single layer DLC, DLC/Hyperlox® and the multi-layer DLC coatings. The tribologically severe SRT was selected to evaluate the coatings. It was concluded that the DLC/Hyperlox® coating, illustrated in Figure 1.15, is a good candidate for dry friction applications. Later, Üstünyagiz et al. [97] have investigated the performance of DLC/Hyperlox®-coated tools in industrial applications. The selected, tribologically critical production stages were deep drawing and ironing in different production lines. The tribologically critical deep drawing operation in production was emulated by a BUT test. To repli-

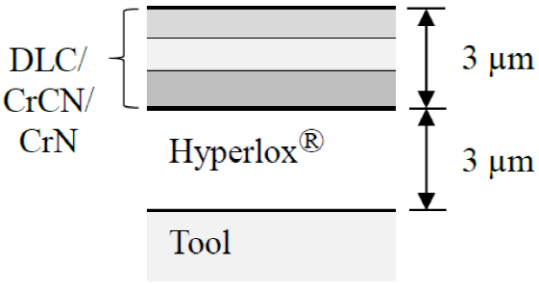

Figure 1.15: Illustration of DLC/Hyperlox® coating structure [96].

cate the industrial ironing of deep drawn parts, the SRT was adopted as laboratory test. Experiments revealed that the coating worked successfully, i.e. with no sign of galling, when it was used with environmentally friendly lubricants, whereas the results were more prone to galling under dry conditions for these specific production cases.

Finally, structured workpiece and tool surfaces can be used to enhance tribological conditions in sheet metal forming. By using various techniques, small cavities in the sheet surface can be introduced. One of the most common techniques is to adapt the skin-pass rolling. The final rolling step of the production can be altered to adjust flatness and surface morphology of cold-rolled products [98]. Different techniques used for structuring the rolls are shot blasting, electrical discharge texturing [99], laser texturing and electron beam texturing [62].

A rather new development in tool surface texturing is the Robot Assisted Polishing (RAP). The RAP technique was developed by Strecon and is shown in Figure 1.16. It is used for polishing metal forming tools. The technique can be combined with machining to texture the surface in different directions with a controlled roughness [100]. The main advantage of using structured surfaces is that, especially when liquid lubricants are used, entrapped lubricants in the structured surface pockets contribute to MPHDL and MPHSL mechanisms. Hence, enhanced tribological con-

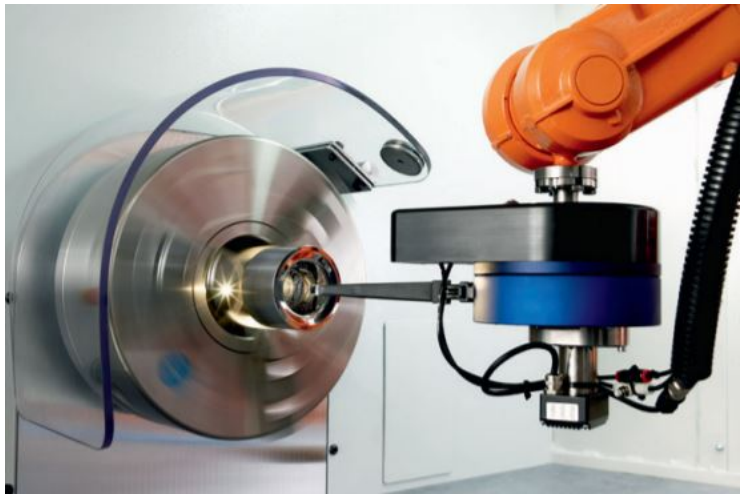

Figure 1.16: Robot Assisted Polishing (RAP) machine [101].

ditions, through changing active lubrication mechanisms, contribute to more efficient adaptation of new environmentally benign tribo-systems.

1.2 Project motivation

Introduction of a new, environmentally benign lubricant in manufacturing requires substantial testing experiments. Testing of a new, environmentally friendly tribo-system in production involves considerable costs and risks due to production stops and possible breakdown of tools. DTU-MEK has therefore developed a system of off-line testing methods during the past years. UST2 was designed and a methodology has been developed for off-line testing of tribo-systems at the metal forming tribology laboratory at DTU-MEK [48].

The UST2 has the ability to run multiple strokes enabling the emulation of the process conditions closely to the ones in an industrial production line. So far, only the BUT test was implemented in the UST2 [48]. However, it is possible to mount specific tool designs to emulate all the common sheet tribo-tests. Being one of the most severe stamping operations,

ironing was selected to be further analysed in this study.

Parallel to the needs of off-line testing, it is vital to understand the active lubrication mechanism during the ironing process. Liquid lubrication mechanisms in sheet metal forming are influenced by a number of parameters including tool and workpiece geometry, surface topography, lubricant bulk modulus and viscosity, which is influenced by pressure, temperature and sliding speed. In order to improve the understanding of the complex influence of these parameters on lubrication, a fundamental numerical approach to the prediction of the limits of lubrication is to be established.

The present project is part of a larger framework programme called SHETRIB coordinated by DTU. The project partners of SHETRIB are Prof. Paulo A. F. Martins (specialist in metal forming and numerical modelling of metal forming operations), Grundfos A/S (Danish manufacturer of pumps), Brdr. Jørgensen Components A/S (Danish sheet and bulk forming company), DFT-Presswork A/S (Danish cold forging company), Strecon A/S (Danish manufacturer of stripwound cold forging tools and robot assisted polishing tools), SSAB (Swedish steel manufacturer) [102].

1.3 Project objective

The SHETRIB project involves one postdoctoral researcher and three PhD students. The overall aim of SHETRIB is to replace environmentally hazardous oils with more environmentally benign oils while focusing not only on development of off-line testing of the tribo-systems through the introduction of new lubricants, laboratory tests, surface texturing technique, tool coatings but also on understanding the fundamental mechanisms of lubrication through numerical analysis.

The objectives of the present work are as follows:

- To predict the performance of new, environmentally benign tribological systems in industrial ironing operations by off-line testing
- To run in and apply a coupled model consisting of a solid mechanical model for the metal forming and a fluid mechanical model for the liquid flow.

1.4 Outline of the remaining chapters

Including the current introductory chapter, this thesis is divided into 9 chapters.

Chapter 1 is the introduction to the thesis. Starting from the basics of tribology in sheet metal forming, the state of the art continues with lubrication mechanism, lubricants, simulative testing and environmentally friendly tribo-systems. An overview of the current literature is followed by the motivation and the objective of this study. In Chapter 2, the selected industrial case study is presented. The problem in an industrial application is defined and the methodology is given. Chapter 3 concerns the emulative SRT. The overall tool design for SRT and the guiding are described. After installation of the tools, setting of the process flow and data acquisition, results of the preliminary tests are discussed. Chapter 4 deals with the analysis of the production platform. After the analysis of the entire platform, attention is then turned to the critical ironing operation. Experimental and numerical analysis of the mechanics are presented. Chapter 5 discusses the thermal analysis of the critical ironing operation. Boundary conditions are identified and used for calculating the tool/workpiece interface temperature. At the end, the identified tribo-parameters of the production line are presented. Chapter 6 aims at analysing the laboratory test platform. By experimental and numerical methods, the critical tribo-parameters of the test set-up are defined and compared with that of the production. In order to achieve the production

temperature, modifications of the SRT tool are presented. In Chapter 7, the experimental results of the selected tribo-systems are discussed. A couple of enhancements are suggested and corresponding results are provided. Chapter 8 concerns fundamental research concentrating on the interaction between fluid flow and metal forming. A fully-coupled numerical approach is proposed. The approach is then applied to a strip reduction case and the outcomes are given. Finally, in Chapter 9, the overall conclusion of the thesis and outlook for the developed numerical and experimental methodology are presented.

CHAPTER 2

Industrial Case Study

In this chapter, an industrial case study is introduced. After a discussion with the industrial partners of the SHETRIB project in December 2015, a production platform of a specific component at Grundfos A/S was chosen to be further analysed. The selected platform is interesting although the current production runs with an environmentally benign lubricant. Due to pick-up on the punch stem after 30000 strokes, the punch is replaced. The company is therefore interested in an off-line testing procedure. In this chapter, the selected production platform and the main process parameters are introduced. The problem is described and finally the testing methodology to the identified problem is presented.

2.1 Project platform

The specific industrial production at the Danish company Grundfos A/S concerns the manufacturing of a stainless steel bearing plate used for a water pump. The bearing plate, shown in the assembly in Figure 2.1,

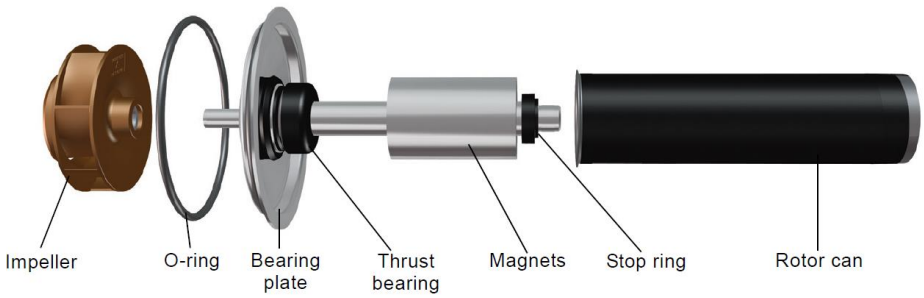

Figure 2.1: Bearing plate and its assembly [103].

carries the thrust bearing which needs to be positioned with precision because the rotor can does not allow any machining after it is mounted.

The process steps related to the progressive tool sequence of the bearing plate are shown in Figure 2.2. The part is produced in thirteen stations. The main shape of the part is determined in the five stages that are marked on the figure. The sheet metal forming operations taking place in these stations are 1. Deep drawing, 2. Reverse drawing, 3. Redrawing 4. Punching and 5. Collar drawing and ironing. The stations between 3 and 4 are either blank stations or the deformation takes place only along the flange.

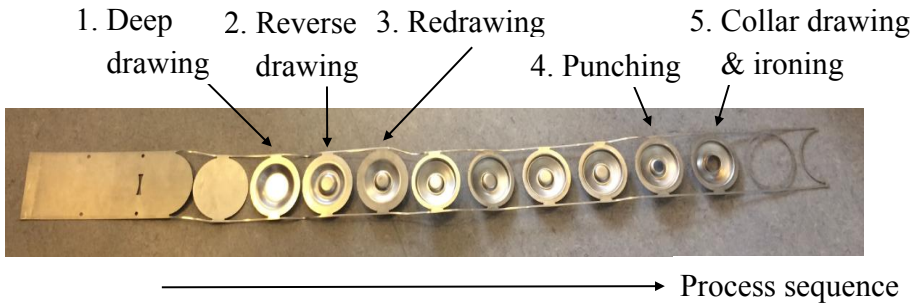

Figure 2.2: Bearing plate production in progressive tool sequence.

2.2 Definition of the problem

The critical operation in this specific production platform is number 5, the combined collar drawing and ironing, where galling occurs if the lubricant is not efficient enough. Especially during the backward stroke, the lubricant film is thinned and the elastic contraction of the die (refer to Figure 1.13) results in severe contact conditions. Unless very efficient boundary lubricants are applied, the lubricant film breaks down, which results in workpiece metal pick-up on the punch stem and scoring of subsequent workpiece surfaces as shown in Figure 2.3 by an example. Due to that, the punch is replaced after each 30000 strokes. The company therefore has an outspoken wish to investigate off-line testing of ironing with consideration of the tribological conditions in both forward and backward strokes.

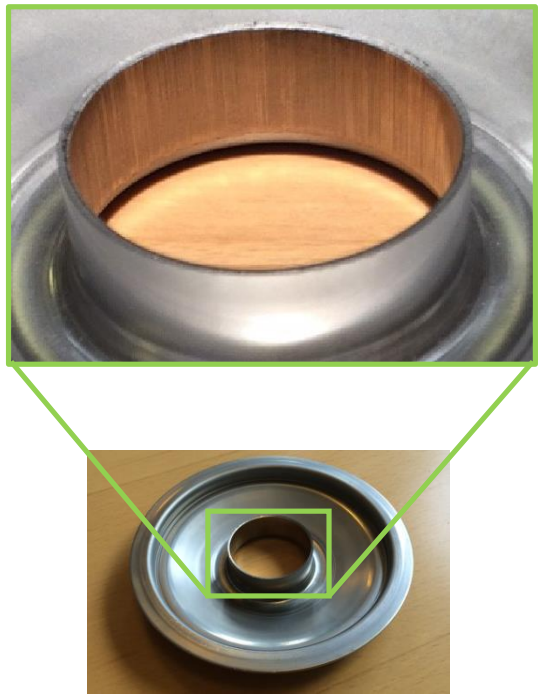

Figure 2.3: Final product with the detail of scoring along the inner wall.

2.3 Process parameters

The workpiece is austenitic stainless steel EN 1.4301 with 150 mm width and 1.5 mm thickness. The wall thickness of the plate is reduced to 1 mm and the ironed wall length is 10 mm. The tool material in the ironing station is PM cold-work tool steel VANADIS 4E (from Uddeholm Tooling AB) with hardness 61 HRC. The tool is coated with AlCrN and the roughness of the punch nose is $R_a = 0.06$. The chemical composition of tool and workpiece materials can be seen in Table 2.1.

Table 2.1: Chemical composition of workpiece and tool steel materials [104] [105]. The composition is given as % by mass.

Material	**C** [%]	**Si** [%]	**Mn** [%]	**Cr** [%]	**Mo** [%]	**V** [%]	**Ni** [%]
Vanadis 4E	1.4	0.4	0.4	4.7	3.5	3.7	
EN 1.4301	0.04			18.1			8.1

The lubricant applied in the ironing station is LA 722086 mineral oil with EP additives and with a kinematic viscosity of 900 cSt at 40°C [106]. The lubricant is applied through channels in the punch. Further details on the lubrication supply are confidential.

The industrial ironing operation uses a Raster 400 ton mechanical press with a link drive operating at 38 strokes per minute (spm). Figure 2.4a and 2.4b show an outline of the ironing operation. The tooling has a bottom plate (die), a punch and a top plate.

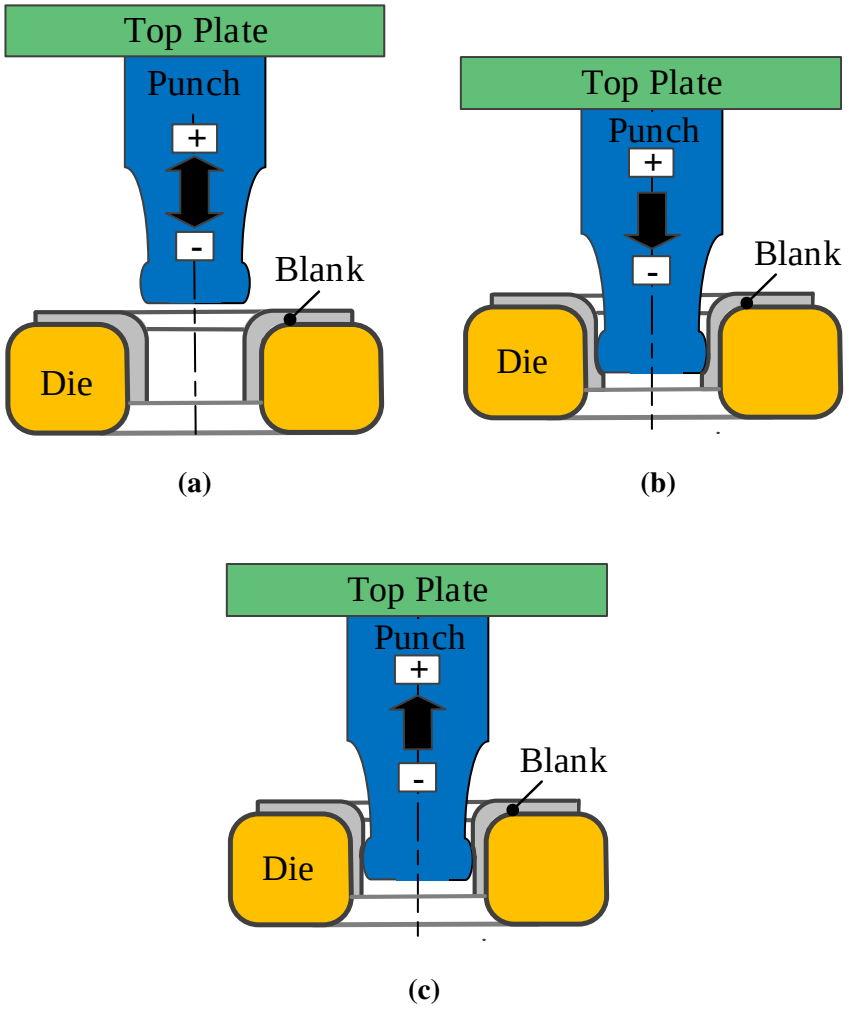

Figure 2.4: Outline of the tool set-up (a) while the tool is open, (b) during the forward stroke and (c) during the backward stroke.

The ram speed of the eccentric press with and without link drive is illustrated in Figure 2.5. The velocity pattern of the eccentric press can be adjusted by introducing a linkage system. Negative ram speed refers to the punch moving downwards until the tooling is closed. Introducing the link drive has the advantage of decreasing the forward forming speed and increasing the backward ejection speed of the punch to increase pro-

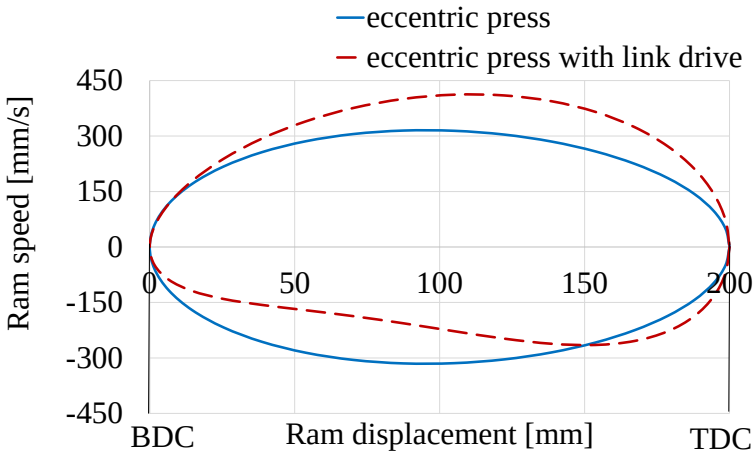

Figure 2.5: Ram speed as a function of ram displacement including the details of Bottom Dead Centre (BDC) and Top Dead Centre (TDC). The direction of the velocity pattern is clockwise.

ductivity. During the forward stroke, in other words, from the Top Dead Centre, TDC, 200 mm, when the tooling is entirely open to the Bottom Dead Centre, BDC, 0 mm, when the tooling is entirely closed, the speed is relatively lower, while it is higher during the backstroke (see Figure 2.5).

2.4 Methodology

The flow chart of the off-line test methodology, modified after [59], is given in Figure 2.6. It starts with the selection of a production platform, that is sought to be improved tribologically. Tribo-parameters in the production platform such as tool/workpiece interface pressure and temperature are determined by numerical analysis as well. After the selection of the suitable laboratory test to emulate the industrial process conditions, similar tribo-parameters are determined for the laboratory test by numerical analysis. If they do not match those of the production platform,

the laboratory test is modified until an acceptable agreement is obtained. The next stage is the laboratory testing. If promising results are obtained after the first screening experiments, the laboratory tests should be completed. At this point, if the selected tribo-system runs satisfactorily, it

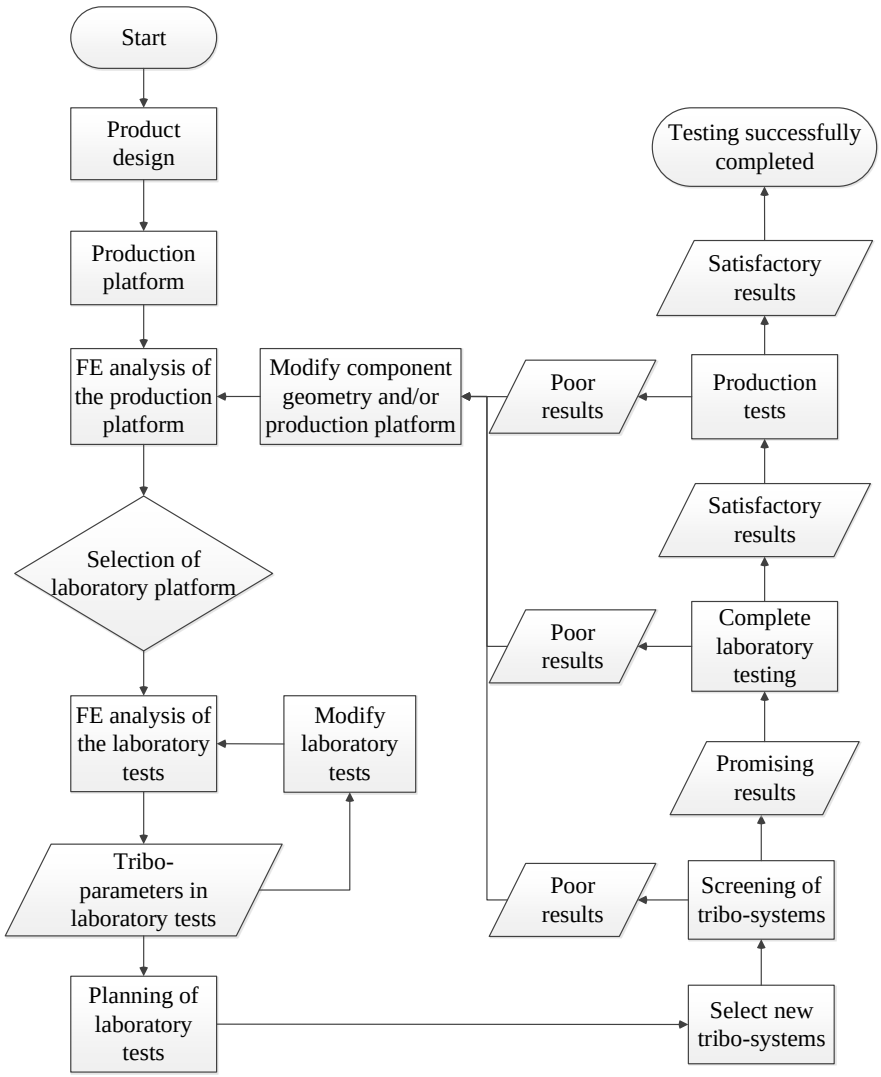

Figure 2.6: Methodology for off-line testing.

can be tested in production. In case of poor results, either the production platform is modified or an alternative tribo-system can be tested.

In order to predict the performance of new, environmentally benign tribo-systems in industrial ironing operations, the above-explained methodology was utilised. The methodology makes use of the UST2, which could only run BUT when this project started. It was therefore necessary to design a new tool applicable for the UST2 to emulate the process conditions in ironing.

2.4.1 Selection of the laboratory test

A suitable laboratory test replicating the ironing operation is the strip reduction process. The simulative SRT was described in Section 1.1.4. Despite the variety of SRT set-ups proposed in literature, they all have either limited numbers of strokes or lack of controlled idle time between strokes. These are two critical issues in the replication of the tribological conditions in ironing since they have a large influence on the actual tool-workpiece interface temperature. Attention should also be paid to high production rates because an increase in temperature results in a thinner lubricant film thickness due to lowering of the viscosity and pick-up, thereby damaging the tools. Furthermore, none of the earlier test designs include replication of the backstroke, which may be tribologically more critical since the lubricant film is thinned to a minimum during this part of the operation.

Two industrial partners, Grundfos A/S and Brdr. Jørgensen Components A/S, expressed their interest in replicating the backward stroke during ironing. Thus, the first step of the project was to design a SRT tool capable of replicating the highly severe tribological conditions that are experienced during both the forward stroke and the backward retraction of the punch in ironing. Additionally, it had to be implemented into the UST2.

2.4.2 Selection of the tribo-systems

Potential tribo-systems were determined together with Grundfos A/S. The sheet material investigated was EN 1.4307 (AISI 304L), an austenitic stainless steel with an initial yield stress of $\sigma_f = 220$ MPa. EN 1.4307 is the lower carbon version of AISI 1.4301 and both materials have similar mechanical and thermal properties [104]. The EN 1.4307 coils were provided by OUTOKUMPU.

Initially, during the development of off-line testing of ironing operations, the Rhenus LA 722086, which is widely used by Grundfos A/S, has been utilised. During the project, a new collaboration with IRMCO, a lubricant company, has been established. After defining the process parameters and discussing these, the following environmentally friendly lubricants were selected: IRMCO 980-323 with a kinematic viscosity of $\nu = 87.3$ cSt at 40 °C, IRMCO 980-156-UK with a kinematic viscosity of $\nu = 177$ cSt at 40 °C and IRMCO 980-080 with a kinematic viscosity of $\nu = 401$ cSt at 40 °C. All lubricants are water-based and metalworking lubricants with additives to improve process performance and do not include any petroleum oil content.

CHAPTER 3

Strip Reduction Test

This chapter is dedicated to the proposed SRT tool design. The initial stages of the tool design, design procedure, final tool and its installation in the UST2 are described. Lastly, the results of the preliminary tests are discussed. The content of this chapter is based on the published study conducted by Üstünyagiz et al. [107].

3.1 Tool design

A schematic outline of the proposed SRT tool is shown in Figure 3.1. The strip is drawn from right to left and reduced at Station A between two stationary cylindrical tool pins. The backstroke during ironing is simulated by the second set of tool pins in Station B. Furthermore, the induced torque on the stationary tool in Station B can be measured.

Several design options were discussed and tested prior to the final design. The initial idea was to emulate forward as well as backward stroke at the

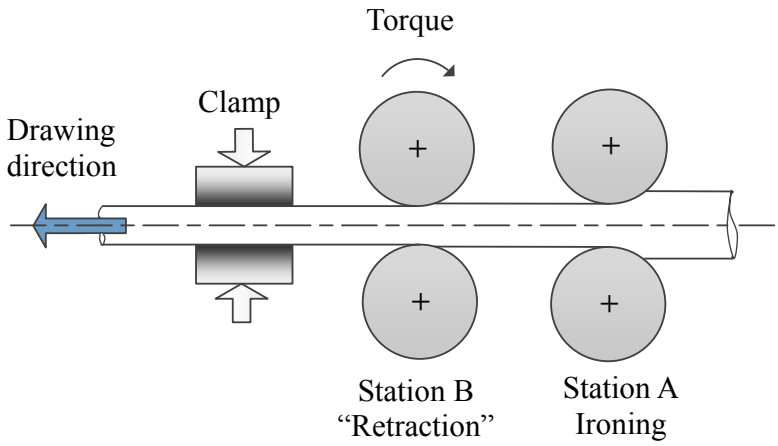

Figure 3.1: Schematical representation of the SRT tool design.

same station. This would require a clamping unit on both sides of the tool pins to pull the strip in opposite directions. However, the UST2 has a single clamping unit that does not allow sliding of the strip towards the right. Instead, the final design includes two sets of tools, the first one, A, representing the forward stroke, the second, B, representing the backward stroke.

After the decision to use two stations was made, the initial design of Station A involved a stationary lower tool pin, while the upper tool pin was free to rotate. The idea was to cancel out the friction between the strip and the rotating tool and avoid the additional polishing of the upper tool, which may occur as a result of the wear-out of the upper tool. However, initial test results showed that pick-up on the upper tool surface was carried into the bearing. As a result, the bearing surface that is in contact with the tool pin was scratched. It was later realised that the upper tool pin got stuck in the bearing when the pick-up reached severe stages. In order to prevent extra time consumption and economical costs by changing the bearing and in order to improve the practicality of the assembly, the upper tool pin was hereafter designed to be stationary.

The main concerns of the design were to ensure the following:

- The vertical load in Station A can be delivered.
- The reduction of the strip can be adjusted.
- The tool pins can be heated.

Station A

Figure 3.2a shows the proposed SRT tool and Figure 3.2b presents a schematical cross-sectional view of its main components.

The tool is designed for 30 % reduction of 0.5 mm strip thickness.

The forward stroke of the ironing process is replicated at Station A by drawing a strip (1 in Figure 3.2b) from right to left. Station A is placed under axis-3 of UST2 (refer to Figure 1.10) to ensure the required vertical load. The maximum vertical load of the hydraulic cylinder in axis-3 is 100 kN. Although the value of the vertical load is not controlled in the current configuration, the maximum load is enough to close Station A and keep a constant reduction defined by a fixed gap running towards a solid stop.

In the following, numbers in round brackets refer to the corresponding numbers of Figure 3.2b. The thickness of the strip is reduced in Station A by means of two stationary cylindrical tool pins (2, 3). The elastic deformation of the upper tool, which undergoes a bending load, is neglected. The upper cylindrical tool pin is located in a housing (4), which is placed on the base (5), and the base is mounted to the UST2 by means of guiding pins (6). The desired thickness reduction can be adjusted by changing the vertical position of the upper tool by placing shims (7) of various thicknesses. Shims are placed between the housing legs and the base. The lower cylindrical tool pin is mounted on a heater block (8) by which the tool temperature can be adjusted by an electric cartridge placed in the centre hole.

Being able to run several tests by turning the pins after use is an economical advantage when investigating lubricant breakdown and pick-up

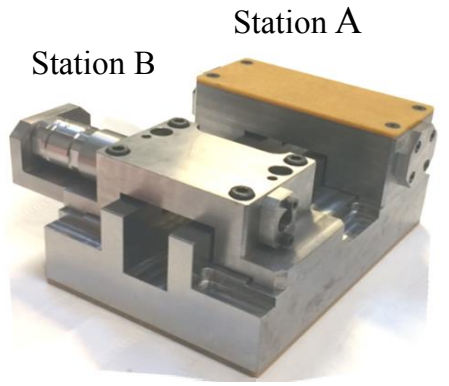

(a)

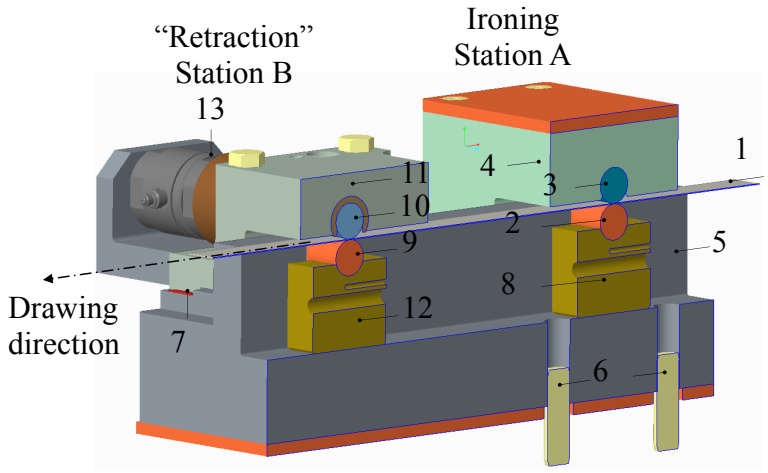

(b)

Figure 3.2: (a) Photograph of the SRT tool design and (b) schematical cross-sectional view of its main components.

under various operating conditions. The SRT tool design allows use of lower (Figure 3.3a) and upper tool pins (Figure 3.3b) at Station A eight times by rotating the tool pins 45°. Detailed technical drawings of the tool pins are provided in Appendix A.

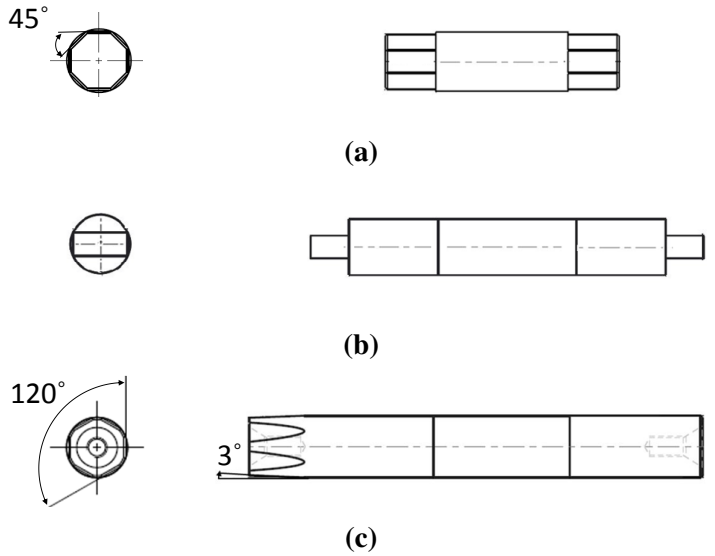

Figure 3.3: Drawing of (a) lower tool pin, (b) upper tool pin at Station A and (c) upper tool pin at Station B.

Station B

The backward stroke of the ironing process is replicated in Station B. Similar to Station A, the second station includes two stationary cylindrical tool pins (9, 10), a housing (11) and a heater block (12). In practical terms, Station B further reduces the strip thickness by adjusting the gap between the two stationary cylindrical tool pins to a value smaller than that utilised in Station A. This is done to emulate the elastic springback of the die during retraction of the punch (refer to Figure 1.13). The tool is closed by four tightening screws. A torque transducer (13) is connected to the upper cylindrical tool pin in Station B through the tool housing shown in Figure 3.2b.

As illustrated in Figure 3.3c, the upper tool pin in Station B has a hexagonal end allowing the tool pin to be removed from the other end with the help of a screw to change the contact surface when it is worn-out. To properly fasten the tool pin, the hexagonal end has 3° inclination from the horizontal line.

The choice of the torque transducer was based on the following overestimating calculations:

$$T = \tau w l a. \tag{3.1}$$

τ is the friction stress, $\tau = m(\sigma_f/\sqrt{3})$. Due to the stripping of lubrication at Station B during reduction, the friction factor m was assumed as 0.1. The flow stress σ_f is around 1000 MPa for strain-hardened steel EN 1.4307 with an equivalent plastic strain of around 0.4 (based on preliminary simulations).

The width of the sheet w is 30 mm. l is the contact length between the tool and the workpiece. It can be calculated with the following equation:

$$l = 2\pi R \frac{\alpha}{360} \tag{3.2}$$

where α is shown in Figure 3.4 and calculated by

$$\alpha = \cos^{-1}\left(\frac{R - \Delta h/2}{R}\right). \tag{3.3}$$

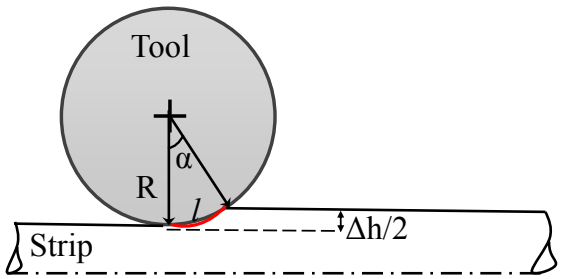

Figure 3.4: Schematical representation of the upper tool pin and strip with details of geometrical parameters used in design calculation of torque transducer selection.

The station is ideally designed for very small reductions. For $\Delta h = 0.04$ mm, and tool radius $R = 7.5$ mm, l equals to 0.55 mm.

Finally, a in Equation 3.1 stands for the lever arm stemming, which is the radius of the tool R.

Based on these parameters and assumptions, the torque equals to 7.1 Nm. For the experimental set-up, a Kistler reaction torque transducer with measuring range ± 25 Nm was chosen. The sensor has been calibrated and the calibration factor was provided by Kistler Group, company specializing in the field of measurement technology. Recalibration is recommended every two years [108].

Furthermore, both stations are positioned by tool pins to ensure accurate positioning. Two springs with an unloaded height of 25 mm are placed at each station in between housings (4, 11) and base (5) (refer to Figure 3.2b), in order to ease the positioning of the shims. The idea is that when the force is released at Station A or bolts are loosened at Station B, the upper parts lift and provide space for changing shims.

The tool pins are made by PM, chromium-molybdenum-vanadium alloyed, cold-work tool steel, hardened and tempered to 63 ± 1 HRC and polished to $R_a = 0.06$ mm. The commercial designation of the tool pin material is VANADIS 4 Extra. The other parts of the SRT tool are made of EN 1.0503 medium carbon steel.

It should be noted that, in this new concept, the tool design does not entirely replicate the common deformation that occurs in an ironing process. In production, the workpiece material slides on the punch and the thickness is reduced, while in the laboratory the strip is reduced from both sides through cylindrical tool pins. Basically, the idea is to replace any flat bottom holder (replicating the stable die) by a rotary or stationary cylindrical tool pin and thereby reduce the friction, which affects the drawing force measurement.

3.2 Guiding tool design

A guiding tool for accurate feeding of the strip into the strip reduction tool was designed and is shown in Figure 3.5.

The design includes two bearing pairs made of stainless steel. The first pair receives the strip coming from the coil reel and feeds it through the lubrication rolls. The second set of bearings following the lubrication rolls ensures alignment of the strip before it enters the SRT tool. With the current design, it is possible to use coil dimensions of 15 mm and 30 mm in width and up to 1 mm thickness.

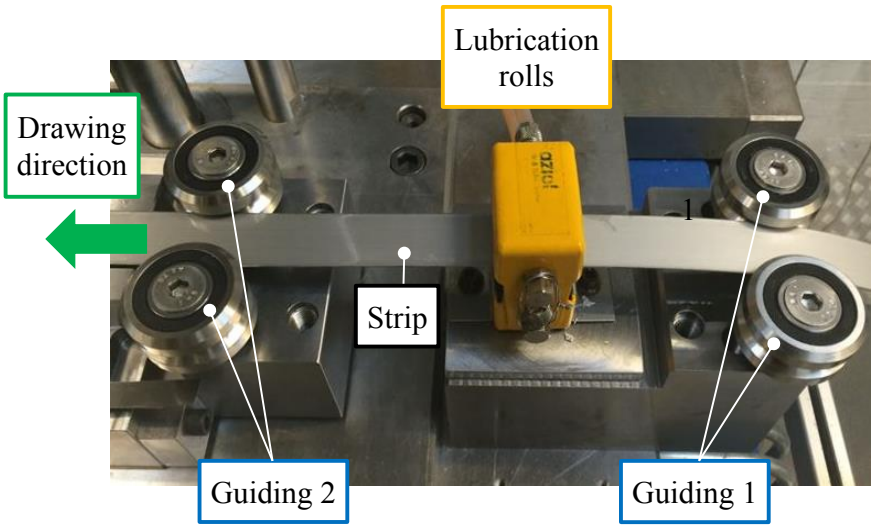

Figure 3.5: Guiding tool and lubrication equipment.

3.3 Installation of the tooling in the tribotester

Figure 3.6 shows the new proposed SRT tool set-up installed in the UST2 at the Technical University of Denmark.

The operation of the SRT makes use of two axes. The horizontal axis, axis-1, draws the strip to a maximum 500 mm before returning to its original position (homing) to continue drawing the strip. It includes a clamping system to hold the strip and a force transducer. The vertical axis, axis-3, supplies the force necessary to keep the tool in position for the given reduction in Station A. Automatic cutting of the strip at the exit of the working region is performed by the 'Cutting Station', while the 'Holding Station' located next to it holds the strip during cutting and homing of the horizontal axis. As described in Section 3.2, the strip passes through a guiding tool for accurately feeding the strip into the SRT tool and through the lubrication rolls before entering Station A. The strip is drawn stepwise for a specified sliding length until reaching the desired number of strokes.

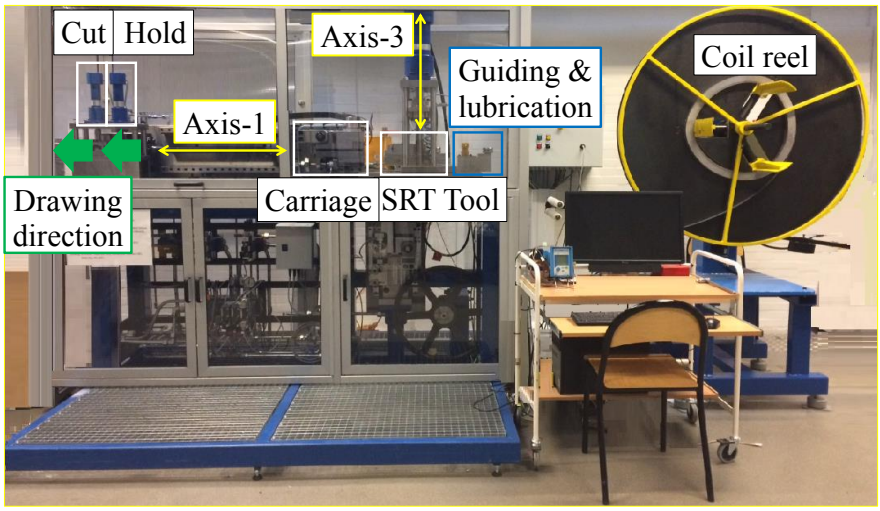

Figure 3.6: The UST2, equipped with the proposed SRT tool set-up.

Table 3.1: General specifications of the new SRT tool installed in UST2.

Parameter		Value
Reduction (for 1 mm thick sheet)	[%]	0-65
Drawing speed	[mm/s]	0-150
Sliding length per stroke	[mm]	0-500
Strip dimensions [width]x[thickness]x[length]	[mm]	[0-30]x[0-2]x[limited by the coil length]
Number of strokes		Limited by the coil length

The specifications of the proposed SRT tooling installed in the tribotester are summarised in Table 3.1.

3.4 Process flow and data acquisition

The block diagram of the process flow is shown in Figure 3.7. The experiment starts with clamping the strip (axis-1), releasing the 'Holding Station' and closing the reduction tool, Station A, with force provided via axis-3. The strip is then drawn a defined sliding length. The drawing of the strip continues either until reaching the defined number of strokes or until reaching the maximum length of axis-1. After reaching the maximum travel length of axis-1 (500 mm), the strip is held by the 'Holding Station', the clamp in the carriage in axis-1 is released and the homing takes place. The loop continues until the desired number of strokes is reached. The lubrication system and the 'Cutting Station' can be activated and deactivated during the experiment.

The process flow was implemented in a LabVIEW code. The UST2 is equipped with a PLC system that communicates with load cells, PC, lubrication system and coil reel. The LabVIEW code sends instructions to the PLC system and receives measured data. The PLC exchanges information and acts like a bridge between the tribotester and the LabVIEW. Detailed information on the PLC system can be found in [48]. The out-

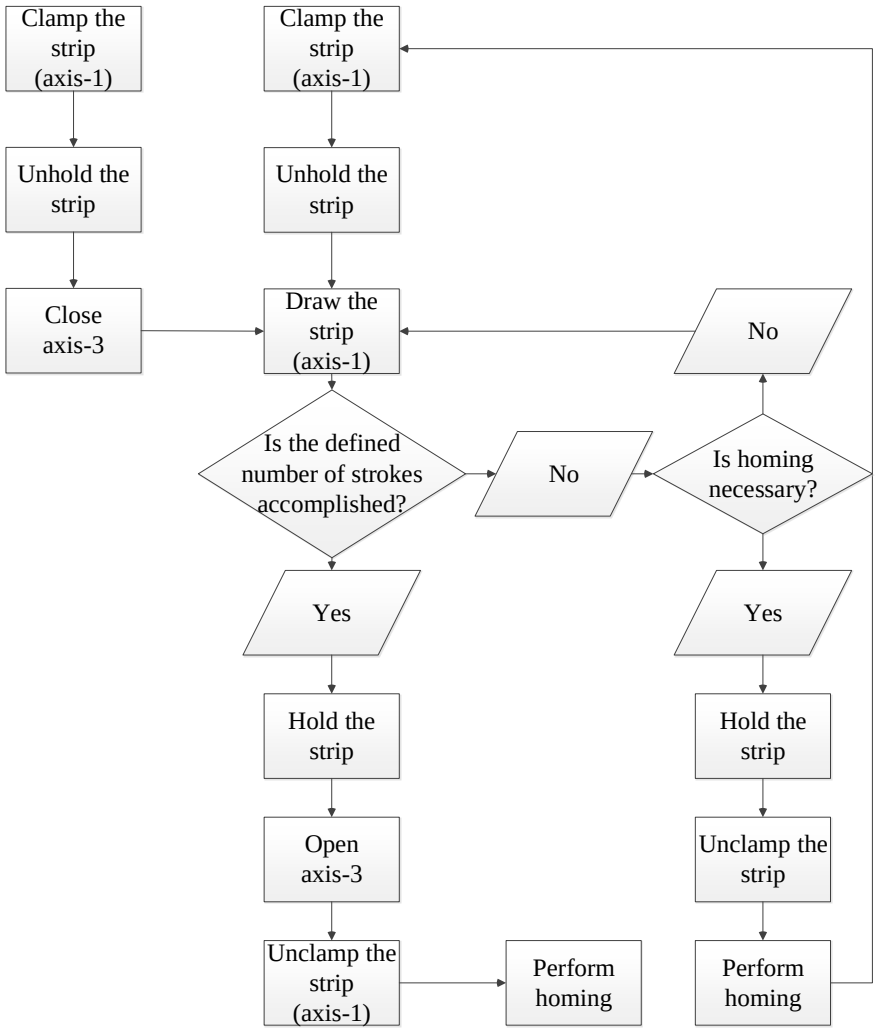

Figure 3.7: Process flow of the continuous SRT.

puts of the developed LabVIEW code for the SRT are drawing force, torque and temperature.

The picture of the programme interface is given in Appendix B. The LabVIEW code developed in this study also gives the flexibility to use the same code for other tests where axis-1 and/or axis-3 are active such

as strip drawing or draw bead testing.

3.5 Preliminary testing

The potential and performance of the new SRT tool set-up were investigated by means of preliminary experiments performed with EN 1.4307 stainless steel strips with 1 mm thickness and 30 mm width. Before each test, the cylindrical tool pins were cleaned with alcohol using a soft tissue after which they were placed in the test tool. The desired strip thickness reduction was achieved by adjusting the tool set-up with shims. The remaining testing parameters such as the drawing speed, the sliding length and the total number of strokes were chosen as close as possible to the industrial case, i.e. the sliding length was 10 mm and the sliding speed was 50 mm/s. Rhenus oil (LA 722086) was used during the entire investigation.

3.5.1 Verification

The first series of tests focused on replicating a thickness reduction of 20 % during the forward ironing stroke and therefore only Station A was utilised. The second series of tests was aimed at replicating both the combined forward and backward ironing strokes. For this purpose, after performing the 20 % thickness reduction in Station A, the resulting thickness was reduced a further 4 % of the initial sheet thickness in Station B. The second reduction was based on production data showing a similar reduction during the backward stroke. Furthermore, the test rate was chosen as 125 spm.

Figure 3.8a shows the experimental evolution of the drawing force F_d with the number of strokes. As seen, F_d is greater for the second set of tests involving both Station A and Station B because the total thickness

reduction is larger. However, Figure 3.8a also reveals an increase of F_d after 40 strokes for both sets of tests and that this increase is very steep in case of the second test series. By combining these results with the strip surface roughness measurements shown in Figure 3.8b, it is concluded that the onset of galling takes place after 40 strokes for both series of tests and that the second series terminates with an abrupt growth of pick-up in the last five strokes.

The above-mentioned results are due to the increase in thickness reduc-

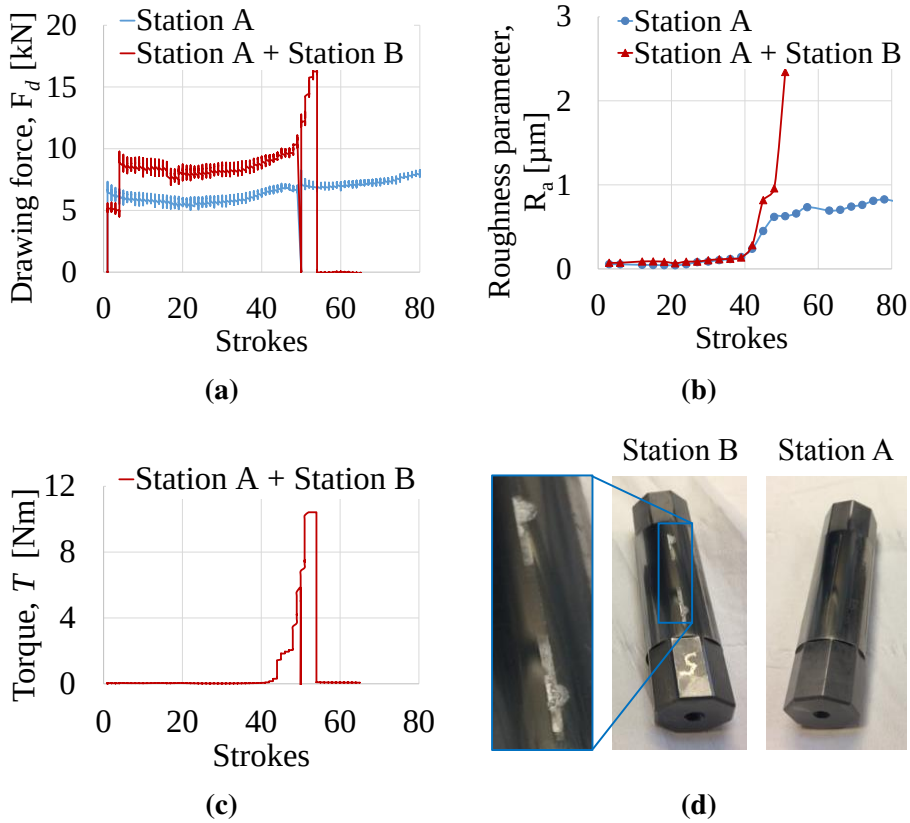

Figure 3.8: Evolution of the (a) drawing force, (b) average strip surface roughness and (c) torque as function of number of strokes. (d) Photographs showing pick-up formation on the tool surface at the end of the experiment.

tion and also due to the fact that the majority of the lubricant is scraped off from the strip when passing through Station A. This explains the increasing rate of galling. The risk of pick-up is much more critical in Station B, where the backward ironing stroke is replicated. This phenomenon also leads to the abrupt increase in torque T, measured on the tool pin in Station B, shortly after the onset of galling that is shown in Figure 3.8c.

Finally, Figure 3.8d discloses the differences in pick-up on the surfaces of the lower tool pins of Station A and Station B. As a result of severe tribological conditions in Station B, the pick-up there is much more critical in comparison with Station A.

The test, replicating the combined forward and backward ironing stroke, in other words using both Station A and Station B, was performed again under the same conditions to test the repeatability of the set-up. Figure 3.9a shows the experimental evolution of the drawing force F_d with the number of strokes. The increase of F_d after around 40 strokes was obtained for both tests. A similar tendency is observed for the torque T, as well (see Figure 3.9b).

The above-mentioned tests were performed to discuss the capabilities of

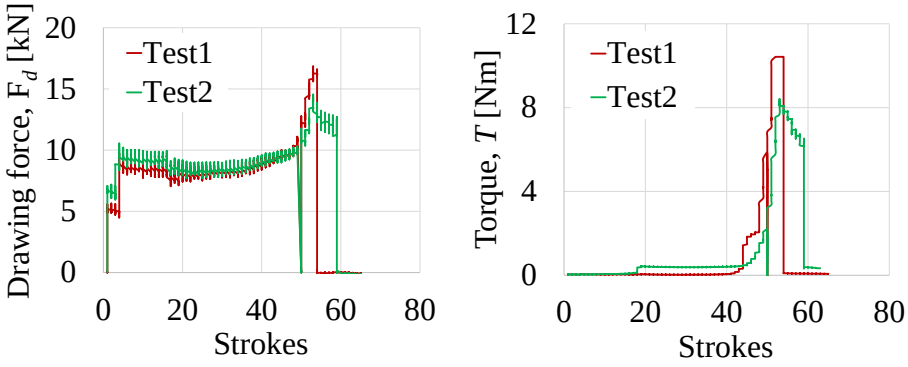

Figure 3.9: Repetition of the evolution of the (a) drawing force and (b) torque as function of number of strokes.

the new design. Achieving an indication of lubricant film breakdown at a similar number of strokes for various measured values, i.e. torque, drawing force and strip roughness, it can be concluded that the proposed design operates well for emulating both forward and backward strokes of ironing.

3.5.2 Influence of the Station B

In consequence of the abrupt increase in the experimentally measured values while emulating the backstroke, it was a question of whether or not the lubricant was entirely scraped off. Station A was set to 4 % reduction to simulate Station B and the test was run twice without any lubricant. In both experiments, severe galling appeared and the strip fractured after around 10 strokes (see Figure 3.10). However, when running with lubrication and using both stations, the tests were performed up to 55 strokes (refer to Figure 3.9a). This shows that the lubricant is not entirely scraped off in Station A before reaching Station B. A boundary layer may have formed, keeping some lubrication throughout both stations.

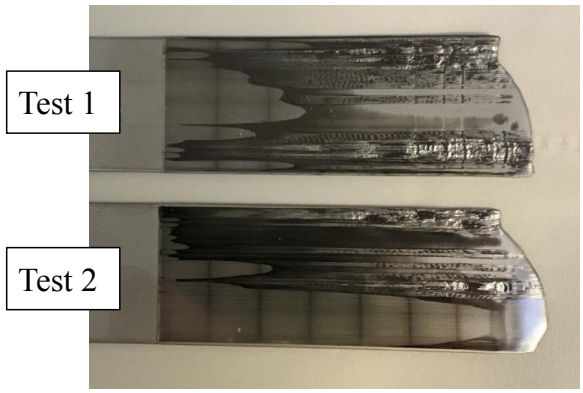

Figure 3.10: Picture of the strips reduced 4 % at Station A under dry condition.

3.5.3 Effect of the tool coating

The influence of tool coating on the onset of lubricant film breakdown was analysed by performing laboratory tests with and without tool coating. The laboratory test was run in accordance with the testing parameters used for verification analysis.

In severe sheet metal forming processes, wear or damage normally occurs at the tool/workpiece interface, which could be caused by galling, thermal load and/or plastic deformation. In order to improve the tool life, the tool surface may be coated. PVD-based AlCrN coatings are characterised by good wear protection at high temperatures due to high hot-hardness and low thermal conductivity [109].

The industrial partner Grundfos A/S uses AlCrN coating for the ironing tool. To have the similar conditions in the laboratory, the SRT tool pins were coated with AlCrN by the same provider, Oerlicon Balzers.

Figure 3.11 shows the average strip roughness as a function of strokes obtained with AlCrN-coated and uncoated tool pins. From these results,

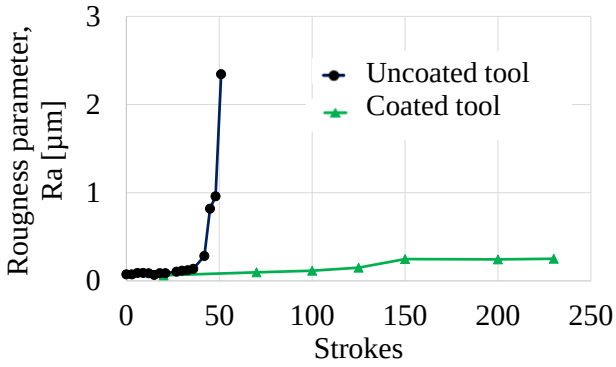

Figure 3.11: Evolution of the average strip roughness as a function of the number of strokes for the experiments performed with coated and uncoated tool pins.

it is concluded that the onset of lubricant film breakdown is delayed significantly by the AlCrN coating, as expected.

3.5.4 Effect of the test rate

The effect of the production rate on the onset of lubricant film breakdown was analysed by performing laboratory tests with three different test rates. In addition to the previously performed test with the test rate of 125 spm, tests were performed at 30 spm and 38 spm. Constant values of sliding speed, 50 mm/s, and sliding length, 10 mm, were chosen in accordance with previous verification tests.

In metal forming, the heat is generated due to plastic deformation and friction. At higher production rates, the time allowed for heat dissipation is limited. As a result of high temperatures, not only the material properties of the tool and the workpiece, but also the viscosity of the lubricant changes.

Figure 3.12a shows the drawing force F_d and torque T as a function of number of strokes. It is shown that the drawing force and the torque increase after 150 strokes for the test rate of 125 spm. By putting together these results with the strip surface roughness measurements shown in Figure 3.12b, it is concluded that the onset of galling takes place after 150 strokes under a test rate of 125 spm. Furthermore, Figure 3.12b indicates that the experiments conducted at test rates of 30 and 38 spm worked well enough because all the experimentally measured values - drawing force, torque and strip surface roughness - remain at a constant level.

From the above, it is concluded that there are not any indications of onset of galling via experimentally measured values for test rates of 30 and 38 spm. However, visual inspection points towards a light wear in the form of scoring along the strip surface.

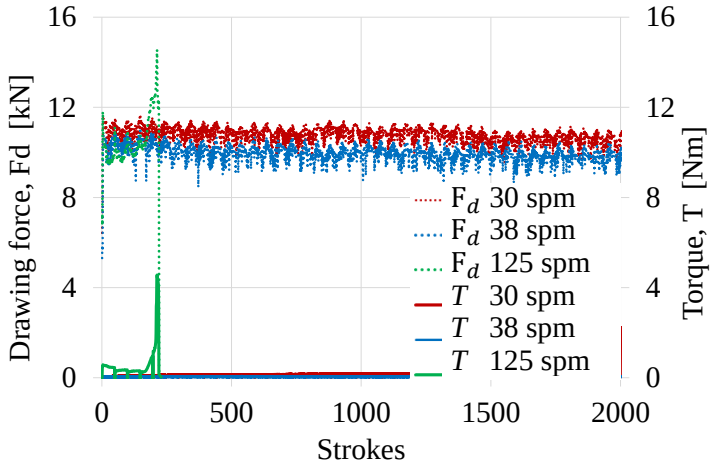

(a)

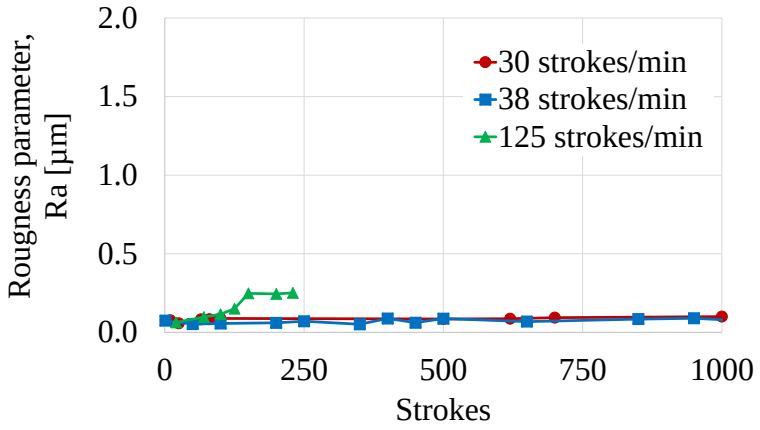

(b)

Figure 3.12: Evolution of the (a) drawing force and torque and (b) average strip surface roughness as a function of the number of strokes for various test rates.

For further examination, the experiment with the lowest test rate, 30 spm, was selected. Figure 3.13a shows pictures of the strip surface taken after stroke number 10, 500 and 1000. Scratches within the blue rectangle were investigated by Scanning Electron Microscope (SEM) and the images are shown in Figure 3.13b. The pictures taken at a magnification of 100 μm shows widening of the scratches with increasing number of strokes. Finally, the upper tool pin of Station B was examined by microscopy. Figure 3.13c shows local pick-up on the tool surface corresponding to the places where the scoring on the strip occurred. However, the degree of adhesive wear is not critical enough to affect the overall strip surface roughness.

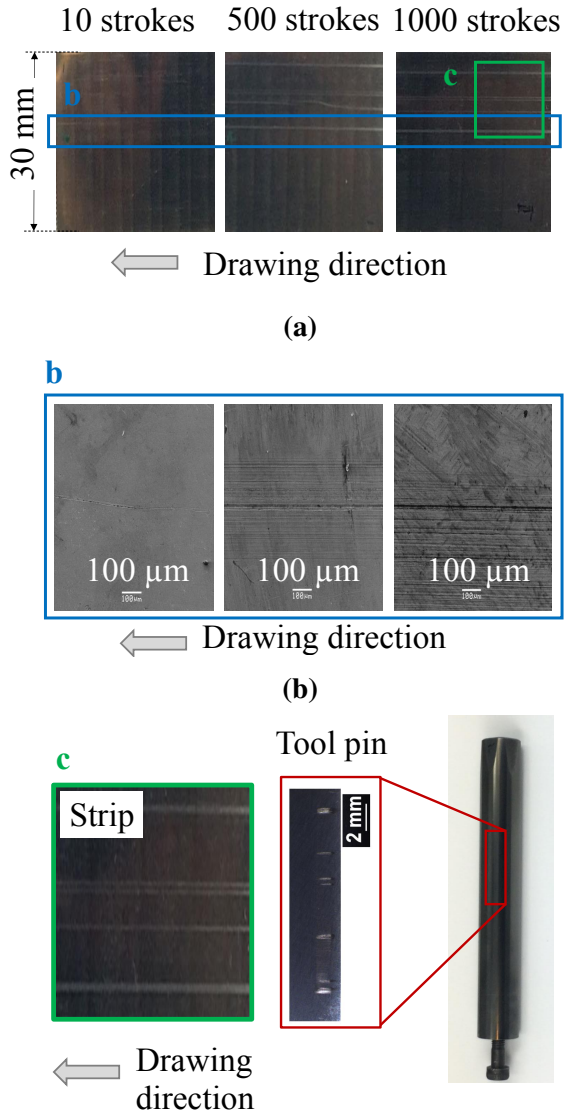

Figure 3.13: (a) Pictures of the strip surfaces taken after 10, 500 and 1000 strokes with details of (b) scanning electron microscope images of the strip surfaces and (c) scoring along the strip surface with corresponding scratches on the tool surface.

3.6 Conclusion

In this chapter, results of screening tests using the new SRT tool were presented and discussed. The design consists of two stations replicating not only the main ironing process but also the backstroke of the punch. During the backstroke in the production process, the lubricant is partially scraped off, and the elastic contraction of the die may cause pick-up on the punch. The tribotester enables running of the test for several strokes under specified conditions including emulation of the backstroke. Therefore, implementing the new tool into the tribotester provides the possibility of studying any selected industrial ironing case in the laboratory. Preliminary tests have shown promising results with regards to the identification of lubricant film breakdown. It was found that the risk of pick-up is much more critical in Station B where the backstroke is emulated. This is due to an increasing rate of galling as it is reported by the industrial partner. Further test campaigns were performed with coated tools and various test rates in accordance with the industrial case. The SRT runs successfully with AlCrN-coated tool pins and a test rate of 38 spm up to at least 1000 strokes. However, the current test set-up must be enhanced in order to ensure the same tribological parameters, such as interface pressure and temperature, as in the industrial production case.

CHAPTER 4

Analysis of the Production Platform

This chapter deals with the numerical analysis of the production platform. Firstly, the development of the 2D numerical model of the production platform using commercial FE software LS-DYNA is described. The model was utilized in order to determine one of the tribologically important parameters, contact pressure. Secondly, the validation of the numerical model through profile and thickness measurement of the final part is discussed. Finally, sensitivity analysis of the numerical model is presented. A part of the content of this chapter was published previously by Üstünyagiz et al. [110].

4.1 2D numerical analysis

The progressive die used to produce the bearing plate has thirteen stations. As discussed previously in Section 2.1, blank stations and the stations where the deformation only occurs in the flange are not relevant to

this study. Therefore, among those stations, the numerical models were developed for three drawing stations (Operations 1-3), one blanking station (Operation 4) and one collar drawing and ironing station (Operation

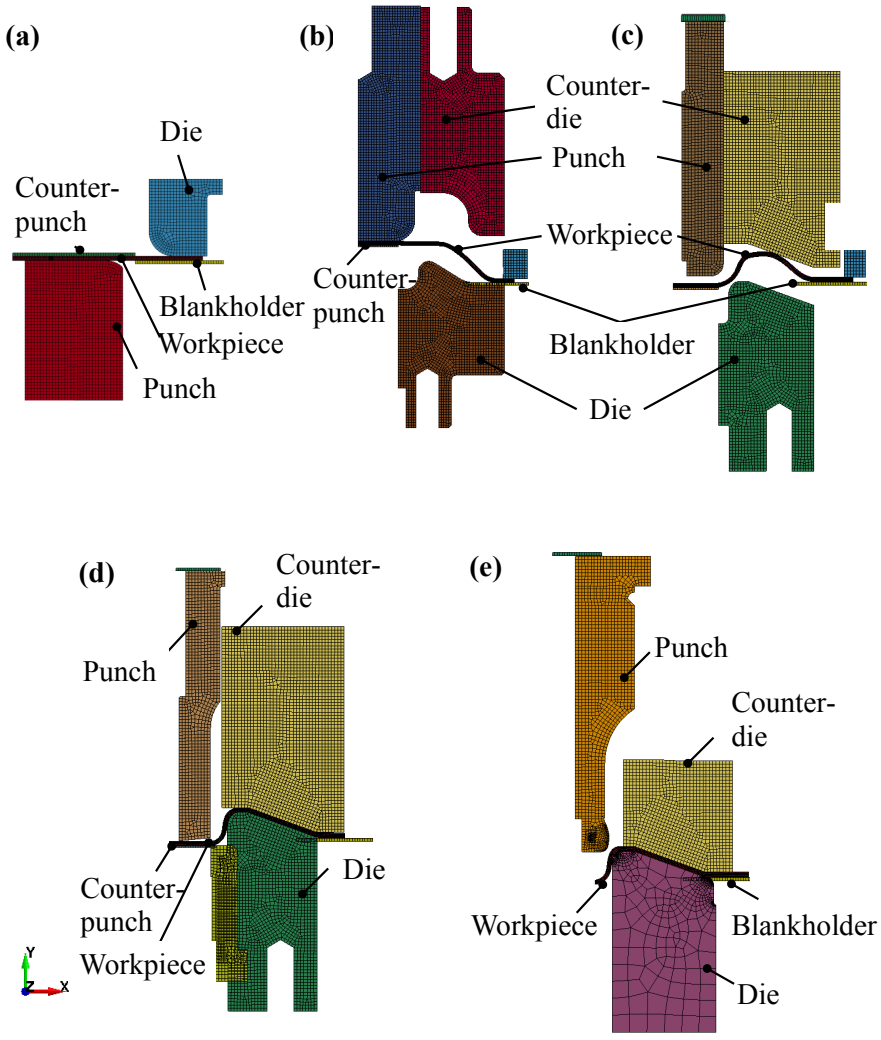

Figure 4.1: Finite element 2D axisymmetric models of (a) deep drawing, (b) reverse drawing, (c) redrawing, (d) blanking and (e) ironing.

5) (refer to Figure 2.2).

Figure 4.1 shows the discretisation of the numerical model before the start of each process. The geometry of the critical parts were provided by the industrial partner and further used for numerical modelling. The numerical model consists of 2D axisymmetric solid elements. The dynamic effects such as inertia and damping were neglected. Thus, implicit analysis were used to solve the equilibrium.

4.1.1 Material model

The flow curve of the material used in this study is based on plane strain compression test. The test was performed previously for four coil materials: EN 1.4301, EN 1.4162, DP 800 and 1200 MZE [48]. In the numerical analysis of the current project, the flow curve obtained previously for EN 1.4301 was implemented.

Initially, the flow curve obtained from tensile test was provided by the coil provider Outokumpu. However, the provided flow stress goes only up to strain values of 0.3. Instead of extrapolating, it is desirable to obtain flow stress values for larger strains by testing. Due to lack of necking, the compression test is one of the more suitable material testing methods to determine the stress-strain curve for larger strains. If the raw material is in the form of sheets, the stack compression test may be utilised for evaluation of the flow curve. This test was originally developed by Pawelsky [111]. Later, Merklein and Kuppert [112] and Alves et al. [113] performed the stack compression test utilising cylindrical sheets to show that the stack compression test can be successfully used for determination of material flow curves.

Inspired by the stack compression test, for testing sheet material at high strains, plane strain compression test was used [48]. During this test, the strip is compressed between two long flat tools. In order to satisfy the plane strain condition, the width of the strip should be at least five times

larger than its thickness. Additionally, the strip thickness to tool width ratio must be in the range of 0.25 to 0.5 in order to limit the influence of friction and inhomogeneous deformation. Due to limitation in the press capacity, it was necessary to use a smaller tool width to achieve higher stresses as a result of larger deformation. Three tool sets with widths of 10 mm, 5 mm and 2.5 mm were used. The initial, total thickness of the stacked sheets was 5 mm. The incremental deformation of the same region was obtained using three sets of tools.

Figure 4.2 shows the flow stress curve of EN 1.4301. The plotted flow stress when $\varepsilon_{eqv} < 0.3$ comes from tensile test data provided by Outokumpu. For larger strains where $\varepsilon_{eqv} > 0.3$, the results of the plane strain compression test are plotted.

In numerical analysis, material model number 24, Piecewise Linear Plasticity was selected. The model allows the assigning of eight pairs of stress-and-strain values, in order to define the flow stress curve. By using seven segments, the model has the capability of approximating a realistic, non-linear stress-strain behaviour. The input pairs of the numerical

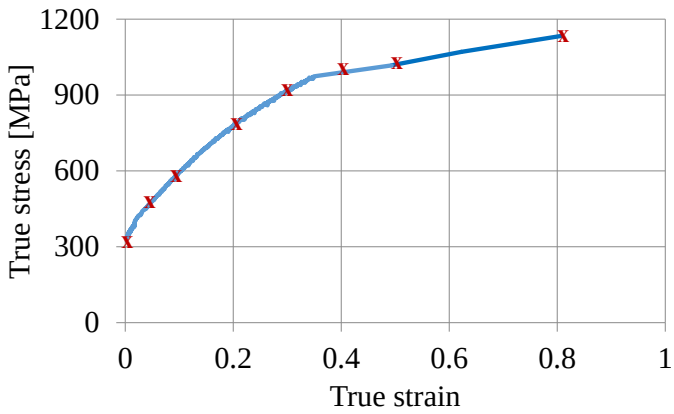

Figure 4.2: Flow stress curve for EN 1.4301 obtained from plane strain compression test with the details of inputs (marked with red cross) used in the numerical model.

Table 4.1: Mechanical material properties used in the numerical model.

Parameter		Tooling Vanadis 4E	Workpiece 1.4301
Structural density	[g/cm^3]	7.7	7.9
Young's modulus	[GPa]	206	200
Poisson's ratio		0.3	0.3

model are shown by red crosses in Figure 4.2. The material properties used in the numerical model in addition to Figure 4.2 are presented in Table 4.1. These were used for numerical modelling during the entire project (if not stated otherwise).

4.1.2 Drawing and blanking stations

The punch, die and blankholder were assumed rigid materials. The stainless steel 1.4301 strip was modelled as an elasto-plastic material with a defined stress-strain curve as discussed in Section 4.1.1. The 1.5 mm thick strip was discretised with 8 elements through the thickness with an aspect ratio of 1.

In operations 1-4, the counter-punch was modelled as a simple plate. In the real production, the counter-punch plays a role during the ejection of the part after each operation. In numerical modelling, displacement of the counter-punch was determined by the displacement of the punch. In operations 2-4, counter-punch force was 1000 N. The blankholder force was 644 N for the first operation and it was increased to 1000 N for the following stages. The small part at the flange end was designed as a simple representation of the tooling at the flange end. The accuracy of the flange region is less significant as the point of interest is the inner wall where the ironing takes place. For the blanking operation, a maximum failure criterion was defined. It was done by implementing a maximum plastic strain value of 1.2 in the material keyword.

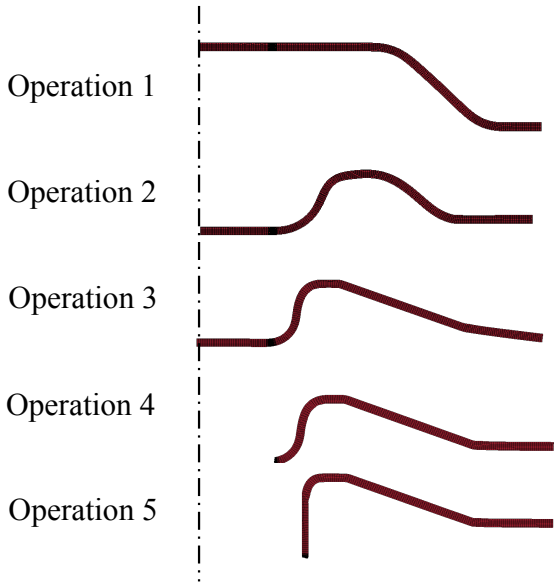

Figure 4.3: The shape of the deformed parts after each operation.

The ram motion was provided by Grundfos A/S and later used in numerical modelling. After the first operation was completed, the strain distribution of the part was saved in a file and imported to the second simulation. The procedure was repeated for operation 3, i.e. an output file from operation 2 was used as input for operation 3. The procedure was followed until operation 5. The simulated deformed workpiece shapes after each forming step are shown in Figure 4.3.

4.1.3 Ironing station

The 2D axisymmetric model of the ironing operation is shown in Figure 4.4. The nodes on the top of the punch inside the blue rectangular box were used to assign the displacement curve along the y-axis. As a boundary condition, other rotational and translational degrees of

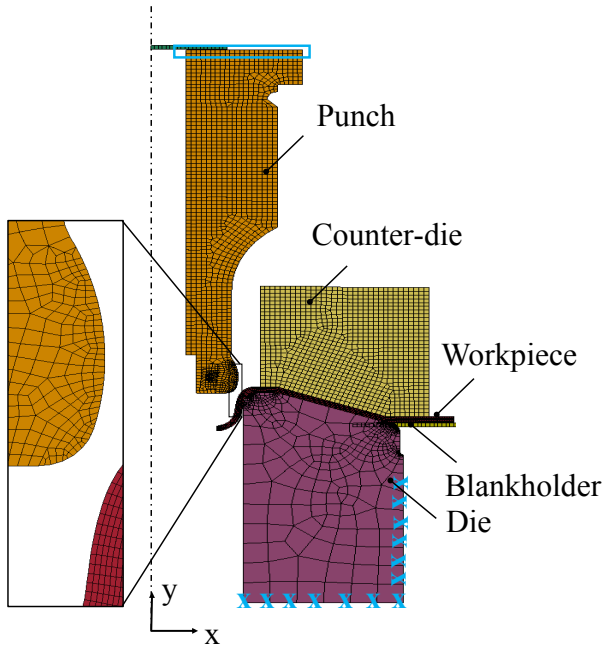

Figure 4.4: Finite element 2D axisymmetric model of the ironing operation with the details of the workpiece and punch nose mesh and boundary conditions.

freedom were constrained. The counter-die and the blankholder were constrained in all directions. As the elastic deflection of the die was important, constraints were applied to the die locally. For that, the vertical movement of the nodes on the bottom of the die along the x-axis were constrained and similarly the nodes on the outer edge of the die were constrained horizontally.

It is clear that the tribologically critical region is where the contact between the punch and workpiece occurs. The normal pressure and the temperature will be investigated at this interface. It is therefore important to ensure the optimal mesh size. The detail in Figure 4.4 shows the mesh at the punch nose and the workpiece. The mesh length at the punch nose is similar to the workpiece mesh length.

For the analysis of the ironing operation, the punch and the die were assigned as elastic materials. The contact between the parts was modelled with the penalty method. The contact pressure is one of the most prominent factors in identification of the tribo-parameters. The selection of the penalty factor is therefore critical. The current model uses automatic surface-to-surface contact. In the software, it is possible to scale the penalty factor. The default value of the scale factor is 1.0. The higher the value is, the smaller the penetration in contact. A very high value of penalty, however, causes ill-conditioning of the equation systems. A small value leads to large penetration. Large penetration results in lower normal pressure. In this study the scale factor was 1.0.

The time-displacement curve was obtained from the kinematic curve of the press given in Figure 2.5 and used as an input. The mechanical problem was solved by implicit solution with an automatically adjusted time step that varies in the range of 10^{-3} and 10^{-5} seconds. As an initial assumption, the friction coefficient between the parts was set to 0.1.

The model was run to investigate the normal pressure at the punch nose. For this purpose it was necessary to define local normal pressures on the elements along the periphery of the punch, where punch/workpiece contact takes place.

In LS-DYNA, the x-axis of local elements is in the direction given by local node 1 and local node 2, and the direction of the local y-axis is perpendicular to the local x-axis [114]. The concept is schematically illustrated in Figure 4.5.

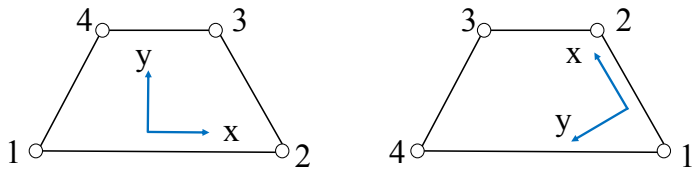

Figure 4.5: Schematical drawing showing the definition of local coordinates.

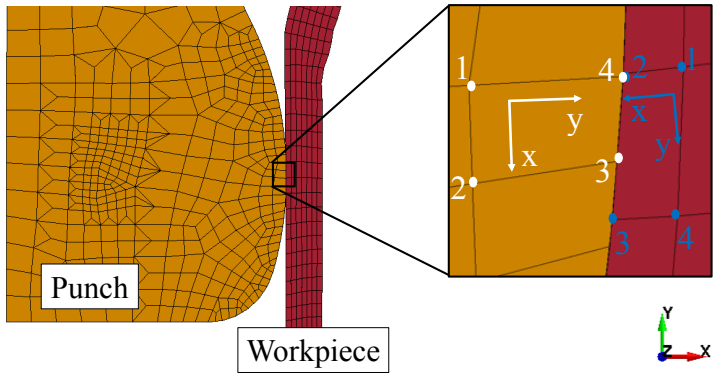

Figure 4.6: Punch/workpiece contact interface with a detailed view of the local coordinates.

As the local coordinates are decided depending on the positioning of the nodes, it is important to be aware of the node sequence of each part. Figure 4.6 shows the punch/workpiece interface with a detailed view of the mesh along the contact region. At the periphery of the punch, only 4-node elements were used. If the shape of the mesh is irregular, the connectivity between elements can change and the results may differ. The positions of the nodes were checked and local coordinates were decided.

The details of the node sequence and corresponding local coordinates of both punch and workpiece are given in the detailed view of Figure 4.6. It was found that the local coordinates of the punch were almost inverse to the global coordinate system. It means that when looking for normal pressure on the punch nose, local-y stress must be chosen. Due to a different node sequence, contact pressure of the workpiece can be seen when choosing the local-x coordinates.

The normal pressure at the punch interface during forward and backward strokes is shown in Figure 4.7. The normal pressures were in fact the normal stresses along the local y-axis. The negative value of local normal stress indicates compressive stresses. The maximum pressure exceeds 1000 MPa during the forward stroke and it increases to about

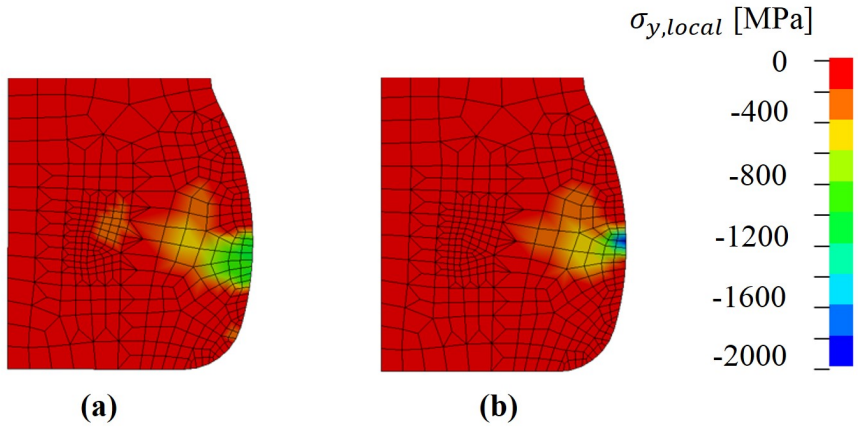

Figure 4.7: Maximum normal pressure at the punch nose during (a) forward and (b) backward stroke.

2000 MPa during the ejection of the ironing punch.

4.2 Validation of the numerical model

In order to validate the numerical model, the thickness and the part profile along the ironed zone were measured.

Figure 4.8a shows the tactile coordinate measurement tool used for the validation of thickness. The spherical tool head measures the coordinates along the inner and outer diameter at the same level of height. For each circle, thirty measurement points were collected. The differences between measured diameters were used for the calculation of the thickness. The measurements were performed for three different levels at 6, 10 and 14 mm distances from the zero level as illustrated in Figure 4.8b. Those measurement points correspond to the beginning, middle and end of the ironed wall. The procedure was repeated for three different workpieces.

The results of the experimental and numerical wall thickness measure-

(a)

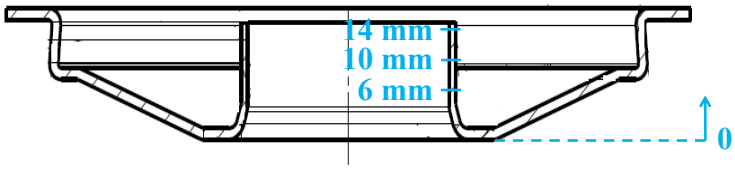

(b)

Figure 4.8: (a) Thickness measurement test set-up and (b) the part profile with the level of heights where the measurements were taken.

ments are summarised in Table 4.2. The thickness of the drawn cup decreases towards the pierced edge of the part. The difference between the results is 1 %, which is enough to verify the thickness.

For the comparison of the part profile after the ironing operation, the MAHR 2D contour measuring system was used. The sample was placed

Table 4.2: Experimental and numerical wall thickness taken from various heights.

Measurement level	[mm]	6	10	14
Experimental thickness	[mm]	1.04	1.04	1.03
Numerical thickness	[mm]	1.05	1.05	1.02

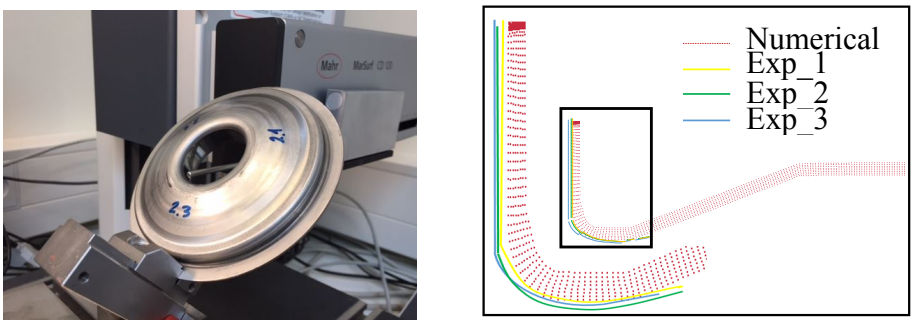

(a) (b)

Figure 4.9: (a) Profile measurement test set-up and (b) numerical and experimental part profile.

with a 45 ° inclination to the contour measuring device as shown in Figure 4.9a and three outer profiles were measured. As the interest lies at the ironed inner wall, the profile measurements were performed for that region. In total, three samples were used for the validation. For each part, the average of three measurements were taken. The profiles obtained from numerical simulation and experimental measurements are compared in Figure 4.9b. Results show that the numerical profile corresponds to the experimental findings.

4.3 Sensitivity analysis of the mechanical model

Effect of the penalty scale factor

The calculated normal pressure at the interface can be highly affected by the penalty factor. The mechanical model was run with three different scale factors for adjusting the penalty factor. The used scale factors were sfact = 1 (suggested as default in LS-DYNA), sfact = 0.5 and sfact = 0.1.

Figure 4.10 shows a comparison between the selected sfact values. The average of the normal pressures taken from the three elements with highest compressive stresses are plotted with respect to time, corresponding

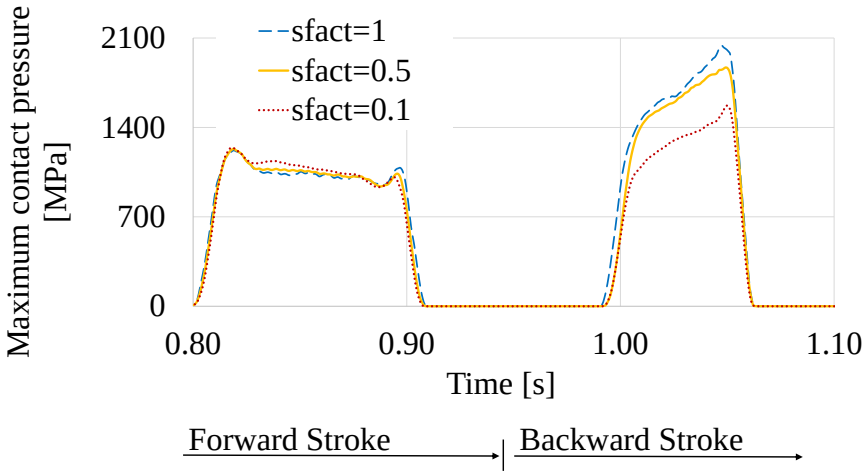

Figure 4.10: Maximum contact pressure on the punch nose with the following penalty scale factors: sfact = 1, 0.5 and 0.1.

to one full stroke of the ironing operation. The pressure increases when the punch touches the part and deformation starts. It decreases to zero when the contact vanishes and the punch reaches the BDC. During the backstroke, the pressure increases again. The normal pressure is highest when sfact = 1. Decreasing the constant to sfact = 0.5 results in about 150 MPa decrease in the pressure during the backward stroke. The decrease is observed only during the backward stroke. It may be due to the fact that the contact area is larger during the forward stroke. For that pressure level, i.e. 1000 MPa, the forward stroke is less sensitive to the penalty scale factor than the backward stroke, where very high normal stresses are observed due to very small contact area.

Figure 4.11 shows the penetration between the parts with various sfact values. The contact is well preserved for sfact = 1 and sfact = 0.5. When decreasing the penalty scale factor to sfact = 0.1, the pressure decreases considerably. However, a very low penalty scale factor results in penetration between the parts, which is not acceptable. Although sfact = 0.5 can be a good compromise, sfact = 1 is used in this study as recommended in the FE software. However, the additional pressure increase of about

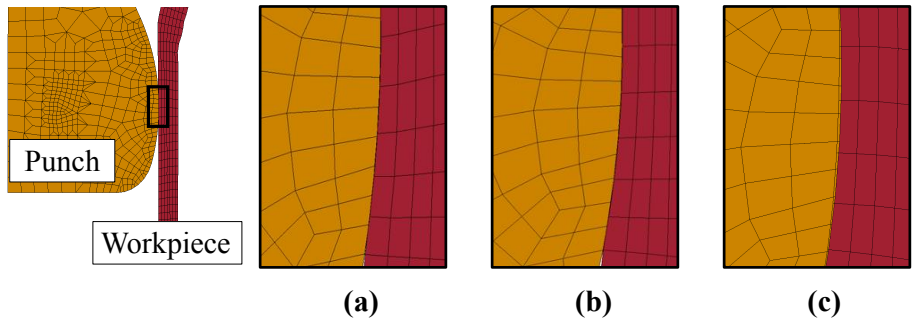

Figure 4.11: Penetration between punch and workpiece with the following penalty scale factors: (a) sfact = 1, (b) sfact = 0.5 and (c) sfact = 0.1.

150 MPa should be kept in mind while defining the tribologically critical parameters.

The effect of mesh size

A sensitivity analysis was performed with various mesh sizes to investigate its effect on the normal pressure. The current element length at the outer periphery of the punch is about 0.25 mm, and the element length of the workpiece at the contact is about 0.4 mm. In order to test a finer mesh, the current mesh was discretised further by a factor of two, meaning that the mesh size at the outer periphery of the punch was 0.125. For the coarser mesh, the outer periphery mesh size was 0.5 mm. The normal pressure of the contact was the stress along the local y-axis illustrated in Figure 4.12. As seen, a smaller mesh size increases the accuracy of the desired contact normal pressure. Smaller meshes allow smaller sections from the curvature and the resulting y-axis becomes perpendicular to the periphery.

It is worth mentioning that another way of shifting the local coordinate system to 90 ° increments regardless of the element shape is to implement Invariant Node Numbering (INN). However, it can be implemented only when using a fully implicit or fully explicit analysis and is not suitable for switching between an implicit method and explicit method. Fur-

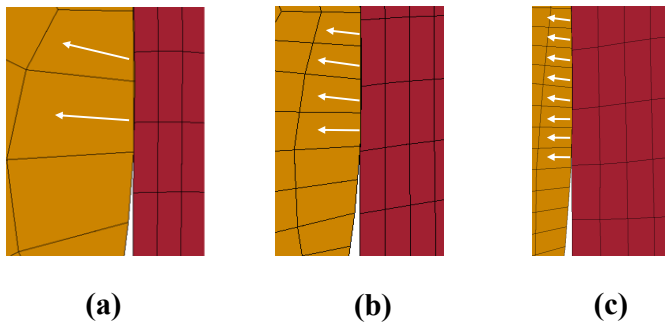

Figure 4.12: Representation of (a) coarse mesh, (b) current mesh and (c) fine mesh of the punch nose with the details of local y-axis.

thermore, the CPU time increases by up to 15 %.

The normal pressure with respect to time for various mesh sizes are shown in Figure 4.13. Simulation with the coarser mesh underestimates the overall pressure. The finer mesh gives similar results to the current mesh during the forward stroke and the normal pressure increases about

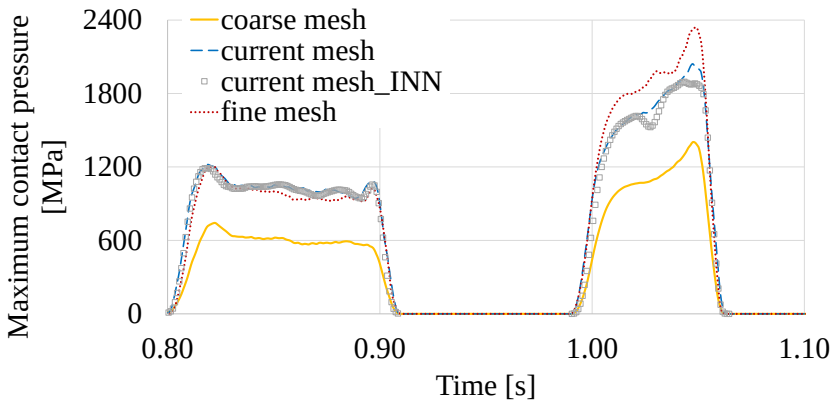

Figure 4.13: Contact pressure on the punch nose with various mesh sizes of punch nose.

250 MPa when using the finer mesh during backward stroke. Considering the fact that the selected sfact may overestimate the normal pressure, preserving the current mesh is a well-founded compromise.

Finally, Figure 4.13 shows that the pressure level when using the INN keyword, is in the same level with the current proposed model. Thus, the assumption, that the local-y axis is perpendicular to the punch nose curvature, is valid.

CHAPTER 5

Thermal Analysis of the Ironing Operation

Tribological conditions in forming operations depend on several parameters, among which the most influential one is the tool/workpiece interface temperature as it directly influences the lubricant performance. The interface temperature in metal forming is commonly identified by either combined experimental and numerical analysis or numerical simulations of several strokes. In any methodology that uses numerical analysis, it should be kept in mind that regardless of the field of application, the reliability of numerical simulations depends on correct descriptions of the boundary conditions.

The present chapter focuses on the thermal analysis of the selected industrial ironing operation where severe process parameters lead to lubricant film breakdown and galling. First, a combined experimental and numerical analysis is applied for determination of the Heat Transfer Coefficient (HTC) between an AlCrN-coated Vanadis 4E tool and Rhenus LA 722086 oil in an unloaded condition, i.e. without the tool being in contact with a workpiece. The analysis is based on experimental mea-

surement of the temperature development in the tool, when dipping it in a warm oil bath, and on an inverse analysis by numerical modelling. A sensitivity analysis of the numerical model is performed to verify the effects of mesh discretisation, temperature measurement location and tool geometry. Afterwards, the tool/workpiece interface temperature in the industrial ironing operation is determined while defining the previously determined HTC between tool and lubricant as a boundary condition. Influencing parameters such as the predicted steady-state tool temperature, friction coefficient and HTC between punch and workpiece on the contact temperature are analysed. The chapter is finalised by a summary on the identified tribological parameters for the selected industrial case study. The content of this chapter is based on the published studies conducted by Üstünyagiz et al. [110], [115] and [116].

5.1 Background

In metal forming about 90-95 % of the mechanical energy used in the process is converted to heat. Some of the heat remains in the deformed region and some flows into the undeformed material. The remaining heat flows into the tooling and to the environment [117]. The temperature distribution in a forming process depends on the following points:

- The initial temperature of each part
- Heat generation due to plastic deformation and friction
- Heat transfer between the parts
- Heat transfer between the parts and/or the lubricant and the environment.

Heat transfer across the interfaces depends on the HTC. For determination of the HTC in an unloaded condition, Semiatin et al. [118] used

two steel dies with different initial temperatures and brought them together under varying pressures. Burte et al. [119] used ring tests with preheated dies to compress AISI 304 stainless steel rings. Two thermocouples were embedded in the lower die with different distances to the die/workpiece interface. The ring compression test was then simulated and the temperature history of the two nodes having the same location as the actual thermocouples was stored. The experimental temperature history was then used to calibrate the numerical results with various HTCs. These studies concluded that at the contact interface in the free resting condition, i.e. without being subjected to load, the HTC is around 1 kW/(m^2·K). For aluminium alloy 2024-0 in an unloaded case, the HTC at 50 °C is, however, 1.5 kW/(m^2·K).

For forging applications, Jain [120] studied the effect of lubricants on the HTC and concluded that changes in HTC are closely related to the chemistry of the lubricant with varying temperatures. He also stated that the HTC is an order of magnitude lower in the unloaded condition. Bariani et al. [121] analysed the thermal conditions between tool and workpiece in hot forging. They determined the HTC as a function of deformation and cooling phases during hot forging cycles. More recently, Asai et al. [122] proposed a low-speed hot-ring compression test to identify the performance of the lubricants at elevated temperatures when considering the heat transfer between air/workpiece and die/workpiece. In an additional study, they have implemented the HTC between lubricant/die and lubricant/workpiece [123]. The results showed that the friction coefficient was underestimated when heat transfer and the effect of velocity are not taken into account when producing calibration curves for the ring test by numerical simulation. In other words, lubricant heat transfer affects the metal forming process and should be taken into account.

Another important issue in metal forming is to predict the tool/workpiece interface temperature as it affects the lubrication, tool life and the final product properties. Pereira and Rolfe [124] studied sheet stamping of high-strength steel on a single-action, mechanical press to investigate the friction- and deformation-induced heating. They developed a thermo-mechanical, numerical model and validated their predictions

against temperature measurements at low speeds. Then, the numerical model was used to replicate the production-type operation condition with 32 spm. They found that frictional heating was the primary factor in reaching the peak temperature at the die surface. However, the developed model did only emulate single stroke operations. Fallahiarezoodar et al. [125] investigated the temperature increase in the tool/workpiece interface in U-channel drawing and deep drawing for single as well as multiple strokes. They found that the maximum temperature in the tool/workpiece interface reached 120 °C in only nine strokes.

It is vital to ensure that the process is in steady-state conditions before determining the interface temperature. Nielsen et al. [126] predicted the tool/workpiece temperature for an industrial deep drawing and ironing operation of AISI 304 stainless steel performed in five stages in a progressive tool. They measured the tool temperature 2 mm from the contact surface in the final ironing operation, where the wall thickness is reduced by 25 %. The developed thermo-mechanical model simulated 100 strokes. The numerically calculated temperature was then compared with the experimental measurements for validation of the model. They determined the maximum interface temperature to be 110 °C in the production test at 100 spm using a PM tool steel, Vancron 40, as tool material and a chlorinated paraffin oil, Castrol PN226, as lubricant. Afterwards, they tested various tribo-systems in laboratory tests using the previously found industrial interface temperature. However, they reported very long CPU time and convergence problems when using DEFORM 2D.

State of the art shows that determination of interface temperatures in industrial metal forming is performed either for a limited number of strokes without ensuring steady-state production conditions or by inefficient numerical modelling. The recently developed combined numerical and experimental approach given in [127], however, offers a more efficient way to determine the interface temperature and is further developed in this current study. Determination of the range of HTC, on the other hand, is complicated and varies with the tool material, workpiece material, lubricant properties and the process. It is therefore important to

determine the value of the HTC for each specific process.

5.2 Punch design

Figure 5.1a shows the ironing punch used in the production process introduced in Section 2.1. During the forming operation, the workpiece/punch contact occurs along the punch nose, marked with the lower ellipse in Figure 5.1a, and the aim was to measure the temperature as close as possible to the contact interface. Additionally, the design of thermocouple holes must ensure a way out of the tool and the press for the electric wires, when the punch is mounted.

Due to the geometrical restrictions, the only way to reach the punch nose was from the upper side. Using multiple measurement points located at various positions would contribute to the accuracy of the numerical model when comparing the numerical and experimental temperature values. On the other hand, the design must also ensure that the stiffness of the tool will not be affected by introducing additional holes. Two thermocouple holes were therefore selected and the diameter of the holes were kept as small as possible. The cross-sectional view of the punch with its thermocouple holes is shown in Figure 5.1a. The holes are 86.3 mm deep and placed with 4.2 mm distance from the bottom end of the punch. The diameter is 2.2 mm, which is the same as the diameter used in the earlier work [126]. The distances from the centre of the hole to the inner surface of the punch nose are 2.9 mm and 3.9 mm (see Figure 5.1b). The flat bottom holes were machined by EDM.

The flatness of the bottom of the hole is especially important for the thermocouple insert in order to define the exact temperature measurement location. However, it is difficult to ensure a flat bottom surface for deep holes. For identification of the actual geometry, Computed Tomography (CT) scanning was used. The punch was scanned using a Scanning XT H 225 ST Industrial CT machine. The CT scanning parameters used in this study are listed in Table 5.1.

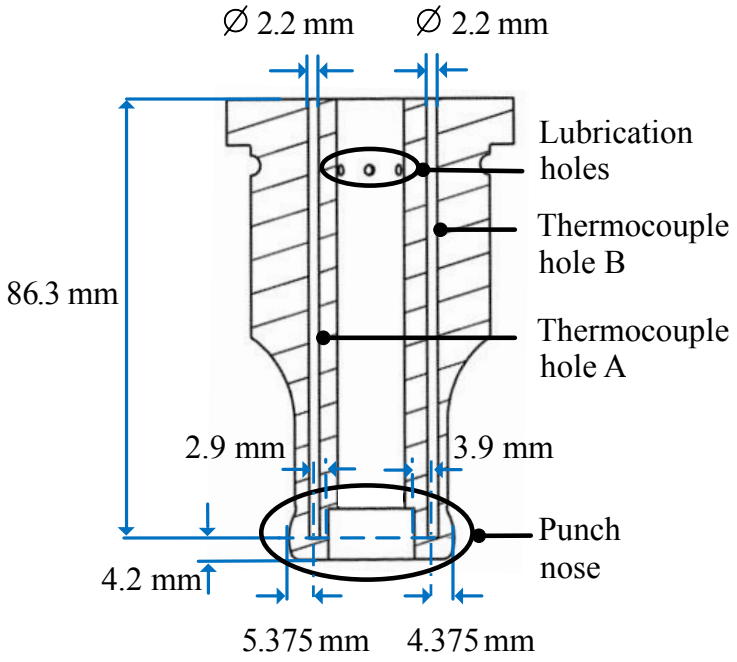

(a)

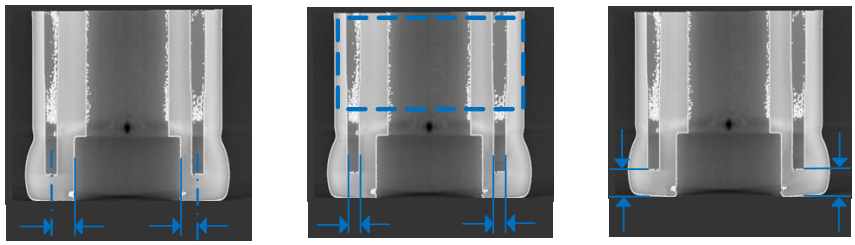

(b)

Figure 5.1: Punch with the details of thermocouple holes shown by (a) a cross-sectional view and (b) computed tomography scanning images of the actual punch.

Table 5.1: CT scanning parameters

Parameter		Value
Current	[μA]	20
Filter material		Copper
Filter thickness	[mm]	2.5
Integration time	[s]	2
Number of projections		1500
Voltage	[kW]	203
Voxel size	[μ]	43

In total, 1500 images with a resolution of 43 μm were obtained. VGStudio MAX software was used to construct a 3D volume set from the images. The critical dimensions are shown in Figure 5.1b. The scanned dimensions show that the bottoms of the holes are flat and that the diameters are 2.17 mm. For the calculation of the margin of error, the diameter of the punch in the region identified by the dashed blue rectangle in Figure 5.1b was measured and compared with the corresponding measurement by using a calliper. The accuracy of the measurement was calculated as $\pm\,0.1$ mm. Based on this, the chosen diameter of the thermocouple is 2.0 mm, which ensures sufficient space for mounting in the holes.

5.3 Thermocouple design

A thermocouple consists of two different, electrically conducting wires that are connected at the hot spot, where the temperature is to be measured (see Figure 5.2). The temperature at the hot spot affects the voltage across the two conductors, which is measured in the cold end of the wires. The voltage difference generated by the two materials, also known as Seebeck voltage, can be related to the temperature.

The type of thermocouple changes with varying thermo-wires. Some of the common types are summarised in Table 5.2. Typically, with a larger

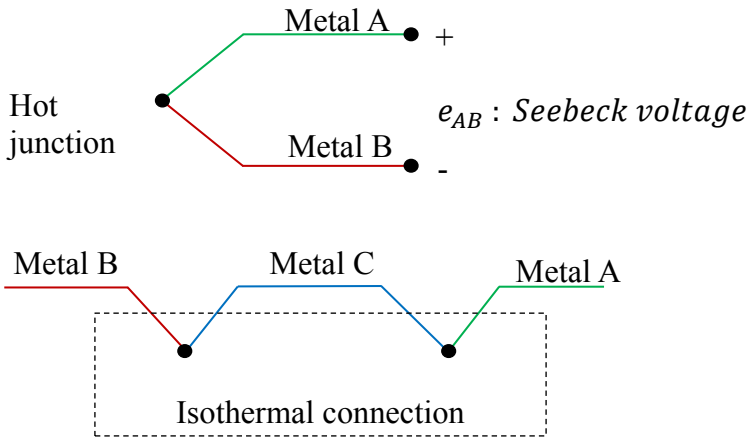

Figure 5.2: Illustration of Seebeck effect and temperature measurement across a third material.

temperature measurement range, the standard limit of error increases. As seen from the table, thermocouple type T has the lowest standard limit of error of $\pm$ 1.0 °C. Furthermore, the range of temperature measurement is within the predicted temperature limits of this study. Being more stable, the T-type thermocouple, with pure Cu as the positive wire and a Cu-Ni alloy as the negative wire [128], was chosen.

A way to measure the critical tool temperature in sheet metal forming operations is capacitor discharge resistance welding of the hot spot junction in the die or punch [129]. Alternatively, the two conductor metals

Table 5.2: Various types of thermocouples with temperature ranges and error [128].

Type	**Temperature range** [°C]	**Standard limits of error**
J	0 to 750	2.2 (0.75 %)
K	-200 to 1250	2.2 (0.75 %)
E	-200 to 900	1.7 (0.50 %)
T	-250 to 350	1.0 (0.75 %)
N	-270 to 1300	2.2 (0.75 %)

can be placed onto a surface (metal C in Figure 5.2) if this third element has a uniform temperature and it is conductive [130] [131], which is also illustrated in Figure 5.2. In fact, the arrangement of the conductor metals individually gives a higher response rate than using a hot spot junction. However, welding the thermo-wires into the bottom of the hole requires several trials until the weld is ensured. Furthermore, the distance between the hot solder point and the surface is not ensured. If the thermo-wires are welded separately, the temperature between the welded points is assumed to be constant, meaning that Seebeck voltage generation of the tool is neglected.

For this study, spot welding of the thermo-wires has considerable risks. The technique may require several trials before a successful weld is obtained. In case of an unsuccessful weld, the flat surface of the hole may not be sustained. As a consequence, the weld can mislead the actual temperature measurement point. Due to the mentioned risks and limited access to the bottom end of the holes, thermocouples with steel inserts were utilised.

Depending on the junction type, thermocouple probes can be grounded, ungrounded or exposed [132] (see Figure 5.3). In grounded probes, the thermocouple wire junction is physically attached to the inside of the probe wall, providing good heat transfer to the thermocouple junction. In an ungrounded probe, the thermocouple junction is detached from the probe wall resulting in slower response time. In exposed junction

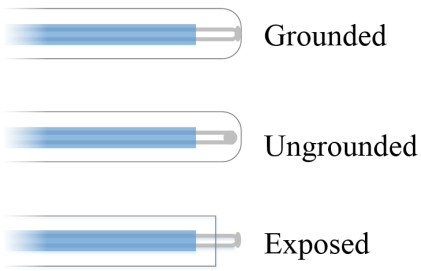

Figure 5.3: Illustration of the thermocouple junction types.

probes, the junction is located beyond the metallic sheath ensuring a fast response rate. However, the junction is not protected and this is recommended when measuring static or flowing non-corrosive gas temperatures. Since the grounded junction type has the fastest response for non-fluid applications, the study was conducted with grounded thermocouple.

Finally, the thermocouples were calibrated. Although the thermocouple supplier promises an accuracy of $\pm$ 1.0 °C, a set of experiments were performed to find the calibration constants. The initial assumption was that the relation between calibrated and uncalibrated temperature is linear in the form of $T_{actual} = x\ T_{measured} + y$, where x is the calibration slope and y is the calibration offset. The thermocouples were exposed to two reference temperatures: room temperature and the boiling temperature of water. Two thermometers with high accuracy, calibrated and certified at DTU Risø, were used to measure the room temperature. The boiling temperature of water was calculated analytically and is given in detail in Appendix C. With two reference temperatures, linear regression for each thermocouple was performed. The calculated calibration constants x and y for the thermocouples are listed in Table 5.3.

Table 5.3: Measured room and boiling temperatures for six thermocouples and respective calibration constants a and b.

	TC$_1$	**TC**$_2$	**TC**$_3$	**TC**$_4$	**TC**$_5$	**TC**$_6$
T_{room} [°C] (ref:20.12)	20.14	20.10	20.10	20.10	20.12	20.09
$T_{boiling}$ [°C] (ref:100.58)	100.43	100.15	100.15	100.52	100.34	100.00
Calib. slope, x	1.002	1.005	1.006	1.000	1.003	1.007
Calib. offset, y	-0.056	-0.082	-0.097	0.017	-0.052	-0.108

5.4 Determination of the heat transfer coefficient between lubricant and punch

In numerical simulations of metal forming operations, a thermal boundary between the tool and workpiece, where the heat transfer occurs due to plastic deformation and friction, is defined. The HTC between the tool and workpiece is usually adjusted to match the numerical results with experimental measurements in addition to other assumed parameters such as friction [74]. Those assumptions influence the accuracy and reliability of the numerical model.

Additionally, the heat transfer between tooling and environment is either neglected or heat transfer directly between tool and the air is considered [133] while neglecting the influence of lubricants on the tool surface. This may give rise to large errors when analysing a production process, where lubrication is provided by flushing over tools and workpieces. In this case, the lubricant will act as a coolant so the heat flux on free surfaces becomes an important boundary condition.

An accurate definition of boundary conditions in Finite Element Method (FEM) is essential for the correct prediction of process parameters, so it is necessary to include the thermal effect of the lubricant in the process and thus to determine the HTCs between the tool and workpiece and the tool and lubricant.

The present section is dedicated to the determination of the HTC between an AlCrN-coated Vanadis 4E tool material and Rhenus LA 722086 mineral oil. The analysis is based on experimental measurement of the temperature development in the tool, when dipping the tool in a warm oil bath, and an inverse analysis by numerical modelling. The results of the sensitivity analysis, performed to estimate the effect of the mesh discretisation, actual location of the temperature measurements and the importance of the punch geometry in the numerical simulations, are discussed.

5.4.1 Experimental set-up

The experimental set-up used in this study is illustrated in Figure 5.4. A container was filled with approximately 500 mL Rhenus oil and heated up to 80 °C. The oil was heated and circulated by a hot plate stirrer to maintain a uniform temperature distribution. The two thermocouple tips were covered with thermally conducting paste and inserted in the holes. When the temperature of the oil was constant, the punch was dipped 20 mm into the bath as shown in Figure 5.4. The two measured temperatures in the punch and the oil temperature were sampled with an acquisition rate of two per second.

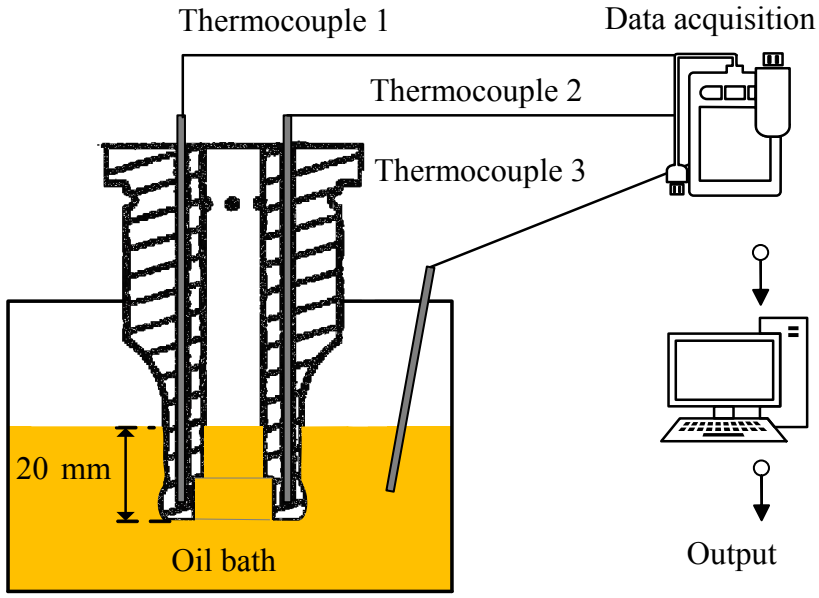

Figure 5.4: Schematical representation of the experimental set-up used for determination of the heat transfer coefficient in an unloaded condition.

5.4.2 Numerical model

Figure 5.5 shows the finite element mesh of the punch with dimensions given in Figure 5.1a. The punch was discretised by approximately 260000 tetrahedral elements and 51000 nodal points. The elements subjected to heat transfer from the lubricant are highlighted in Figure 5.5. For those elements, a convection boundary condition with the lubricant was defined. For the rest of the punch, which was in contact with the air, convection as well as radiation boundary conditions were specified.

The thermal material properties used in the numerical model are presented in Table 5.4. The punch had an initial temperature of 20 °C. The heating of the punch was achieved by fictitious lubricant contact by assigning a final temperature of 80 °C.

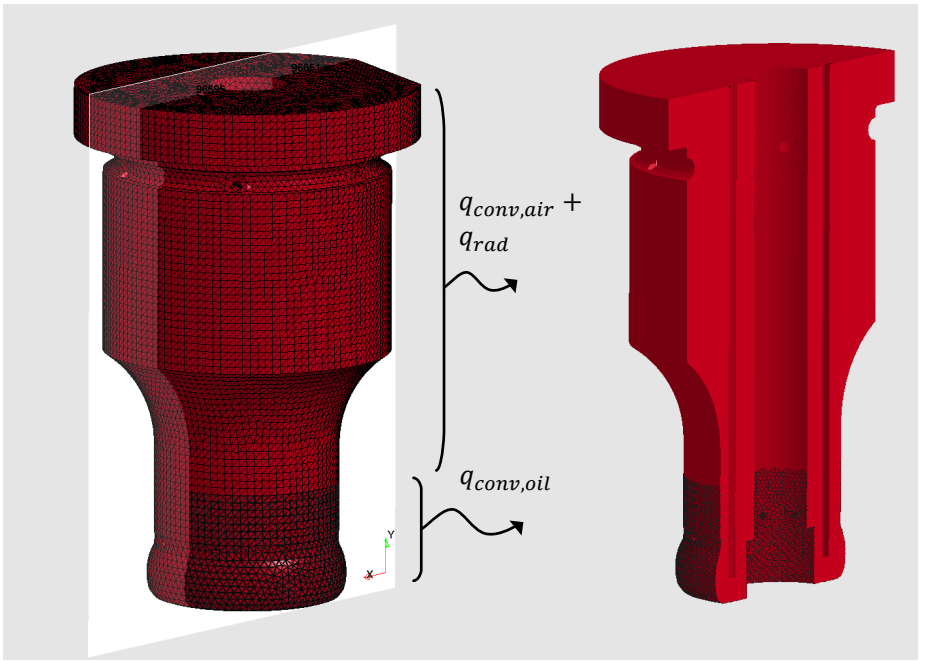

Figure 5.5: Representation of 3D discretisation of the punch for thermal modelling with cross-sectional details and indication of convection and radiation boundary conditions.

Table 5.4: Punch properties and process parameters used in numerical simulations.

Parameter		Value
Thermal conductivity [105]	[W/m·K]	30
Heat capacity [105]	[J/kg·K]	460
Air temperature	[°C]	20
Heat transfer coefficient with air [134]	[W/m^2·K]	10
Stefan-Boltzmann constant	[W/m^2·K^4]	5.6703 10^{-8}

5.4.3 Results and discussion

Figure 5.6a shows the measured temperature during the experiment. As seen, there is no significant difference between the temperatures measured in the punch with Thermocouple 1 (TC_1) and Thermocouple 2 (TC_2).

A preliminary numerical analysis was performed and the temperature evaluations for the nodes, where the TC_1 and TC_2 are situated, were obtained. The results are presented in Figure 5.6b. Similar to the experimental results, the two temperature curves are very close to each other. For simplicity, only one thermocouple, TC_2 was selected for use in the comparison with the results of the numerical analysis.

FEM simulations were carried out with three different heat transfer coefficients: h = 125, 150 and 175 W/(m^2·K). In Figure 5.6c, the numerically computed temperature history of the node taken from the TC_2 location is compared with the experimental evolution of temperature. The results suggest that the best match between numerical and experimental results is obtained when the HTC is 150 W/(m^2·K). The curves also show that the HTC is greater in the beginning of the experiment, whereas it converges to 150 W/(m^2·K) after 20 seconds. The initial variation in HTC is a result of the boundary layer that is established on the punch surface as it is immersed in the liquid. There is a transitional period where the

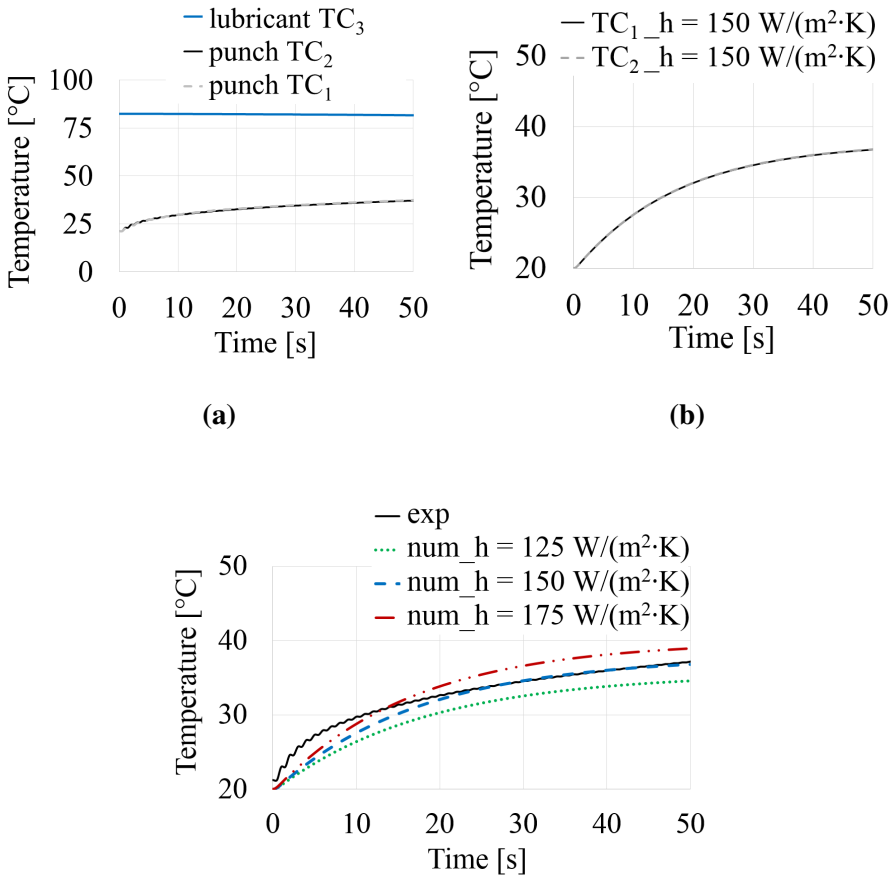

Figure 5.6: Temperature evolution with time representing (a) experimental results taken from thermocouples 1, 2 and 3, (b) numerical results taken from Thermocouple 1 and Thermocouple 2 positions for a specific heat transfer coefficient, h = 150 W/(m^2·K) and (c) comparison of experimental findings and numerical results taken from Thermocouple position 2 using various heat transfer coefficients.

boundary layer builds up and becomes stable giving a constant HTC.

The aim of this study is to define an HTC value which is going to be

used as a boundary condition in a steady-state system. Therefore, the HTC value should be determined after the temperature curves are stable.

5.4.4 Sensitivity analysis

Effect of mesh size

A number of numerical analyses were performed to determine the influence of the finite element mesh discretisation on the level of convergence. The current model uses approximately 260000 tetrahedral elements and 51000 nodal points. The mesh was regenerated by using a finer mesh with twice as many elements and a coarser mesh by using half as many elements as in the current model. The numerical simulation was run using the same parameters listed in Table 5.4. The temperature curves determined in the same TC_2 node are given in Figure 5.7.

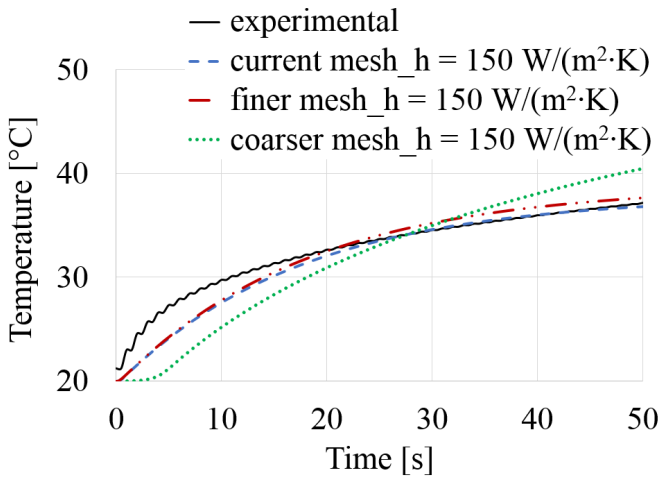

Figure 5.7: Temperature evolution with time taken from Thermocouple position 2 using various discretisations of the punch.

The results indicate that using coarser mesh for determination of the HTC can be deceptive. When the punch was discretised to the current size, the HTC is found to be 150 W/(m^2·K). When the mesh was further refined by a factor of two and the same HTC is used, similar temperature curves with both 'current mesh' and 'finer mesh' were obtained. The current simulation takes 2 minutes, whereas finer mesh increased the CPU time to 20 minutes. The current mesh size may thus be regarded as suitable for this study.

Effect of measurement location

A number of numerical analyses were performed to determine the sensitivity of the location of the thermocouple measurement point. Selected nodes are shown in Figure 5.8a, and the corresponding temperature evolutions are given in Figure 5.8b.

Ideally, the experimental set-up would be designed to measure the temperature on the flat bottom surface of the hole. The flatness of the bottom was verified by CT scanning. However, the exact position of the temperature measurement point, where the thermocouple junction touches the surface during the experiment, is unknown. The temperature history of the three different nodes, A, B and C, which are lying on the thermocouple contact surface (see Figure 5.8a), were therefore calculated and compared with the experimental results. Figure 5.8b shows that the temperature evolutions of the three nodes A, B and C are very close to each other. This may be due to the heat flow from both sides of the punch nose. However, the temperatures of the nodes, D and E, which are lying above the ideal thermocouple contact surface, are lower. At a distance of 2.6 mm above the contact surface, the maximum overall temperature decrease is 1.5 °C (3.6 %).

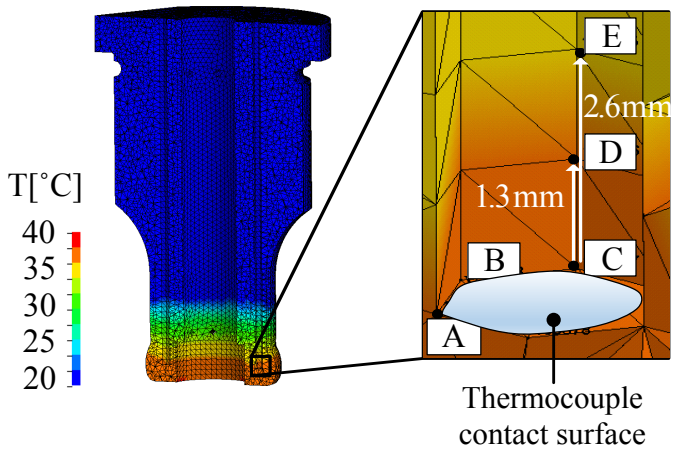

(a)

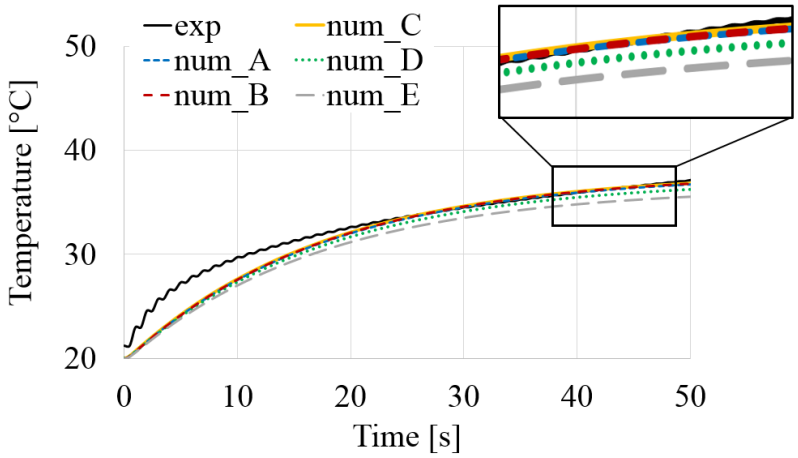

(b)

Figure 5.8: Sensitivity analysis of measurement position shown by (a) punch mesh and position of nodes and (b) temperature evolution with time for the selected positions.

Effect of punch volume

To assess the influence of the thermocouple holes in the numerical results, the 3D mesh of the punch was regenerated without thermocouple holes. A numerical simulation was run using the parameters listed in Table 5.4 and the HTC was kept at 150 W/(m^2·K) as had been previously estimated. The temperature history was taken from the nodes with similar coordinates for the full mesh of the punch and for the model neglecting thermocouple holes.

Figure 5.9 shows the temperature evolution of the numerical results and the comparison with experimental findings. The results indicate that, for this specific heat flow condition, the modelling of thermocouple holes has no significant influence on the temperature prediction.

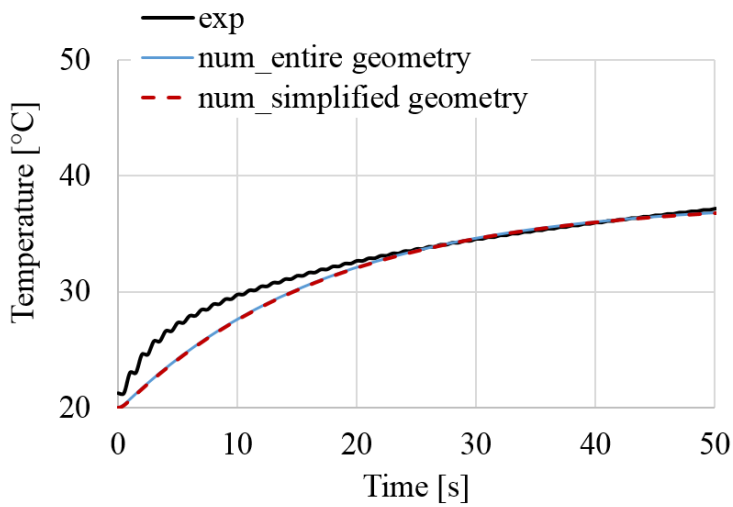

Figure 5.9: Temperature evolution with time for two punch meshes and comparison with experimental results.

5.5 Determination of tool/workpiece contact temperature

The present subsection is dedicated to the determination of the contact temperature at the tool/workpiece interface. The analysis is based on a combined numerical and experimental approach. The experimental measurements of temperature in a few points of the tool are input to a thermal modelling of steady-state conditions. The determined temperature distribution in the tool is used as a boundary condition in the subsequent thermo-mechanical analysis. In this way, the thermo-mechanical model simulates the stage when the production is already in a steady-state condition, thereby avoiding the simulation of the preceding hundreds of strokes, which leads to steady-state conditions. The model is validated by experimental measurements and furthermore, it is tested both with and without inclusion of frictional heating to evaluate the reliability of the thermo-mechanical coupling. Finally, the sensitivity of the model is checked to estimate the effect of initial steady-state temperature distribution of the tool, varying friction coefficient and heat transfer coefficient.

5.5.1 Experimental set-up

The cross-sectional view of the ironing punch was given in Figure 5.1a. The tribologically critical region is the punch nose encircled by an ellipse, where the punch/workpiece contact occurs.

The aim is to measure the temperature as close to the contact interface as possible. Figure 5.1a shows the location of the holes for thermocouples. The distance from the centre of the holes to the outer surface of the punch nose is 4.375 mm and 5.375 mm, respectively.

Figure 5.10a shows the punch from above after mounting the thermocou-

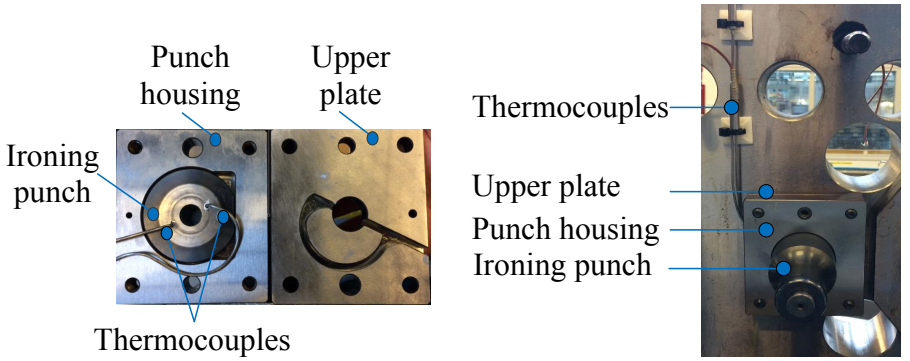

(a) **(b)**

Figure 5.10: (a) Top view of the ironing punch with the main components used in the assembly and (b) assembled ironing punch and main components seen from below.

ples. The punch foot was provided with a plane side matching a plane side on the right hand side of the punch housing in order to prevent the punch from rotating during production. The punch base was supported by an upper plate provided with grooves for the thermocouple wires. Figure 5.10b shows the assembly of the parts. Temperature acquisition was conducted using a National Instruments NI-9212 input module with 8 channels, a maximum sampling rate of 95 measurements per second (per channel) and an accuracy of $\pm 0.71\,^{\circ}\mathrm{C}$.

5.5.2 Numerical model

The numerical analysis includes two steps:

i. Steady-state thermal analysis of the punch.
ii. Transient thermo-mechanical analysis of the ironing process.

The geometry of the problem and the corresponding finite element model was given in Figure 4.4. The thermal model was built upon the mechan-

ical model described in Chapter 4. The model is rotational symmetric and neglects the volume of the thermocouple holes, since it corresponds to less than 3 % of the entire volume of the ironing punch and since the previous investigation given in Section 5.4.4 corroborates this assumption showing no significant difference in the distribution of temperature obtained with a full 3D model with thermocouple holes and a simplified 3D model without holes.

i. Steady-state analysis

The first step of the numerical analysis is to estimate the temperature distribution in the ironing punch when the steady-state condition is reached. The aim of this model is to determine a temperature field for the punch without simulating the multiple steps before the steady-state is obtained.

Figure 5.11a shows the 2D-axisymmetric finite element mesh of the punch. The punch was discretised by approximately 1650 quadrilateral solid elements and 2400 nodal points. The nodes subjected to a fixed input temperature value are highlighted in yellow in Figure 5.11a. During the actual production, the punch was mounted in the tooling system which restricted direct access to the punch. The yellow nodal points at the punch base were assumed to have a constant temperature $T_{base} = 40\,°C$ at steady-state. This assumption was chosen between a lower limit of 28.2 °C representing the measured environmental temperature in production and an upper limit of 50 °C representing the punch nose temperature measured by a laser gun two seconds after production stop. Two thermocouples were inserted into the tool with varying distances to the punch nose. The position of the nodes where the temperature was measured are shown in Figure 5.11a. In the production tests, it turned out that thermocouple A gave no signal. Due to limitations in the allocated time for testing in production, it was not possible to fix this problem. The temperature of thermocouple B was measured as $T_B = 112\,°C$ at steady-state. The input temperature of node B in the steady-state model was therefore assigned to 112 °C.

The steady-state thermal analysis was run for thermal isotropic punch material using the implicit solver of the finite element software LS-

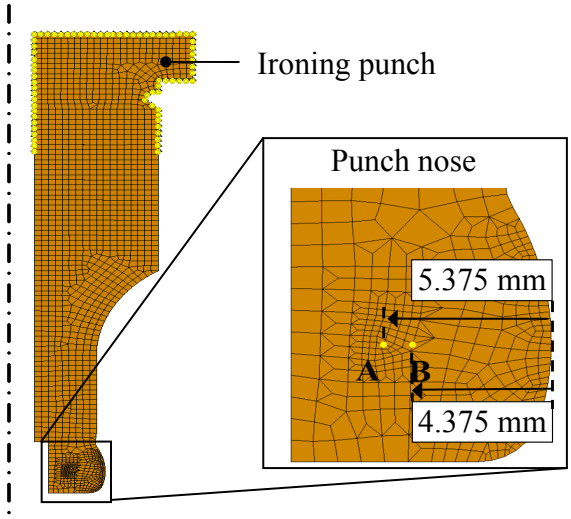

(a)

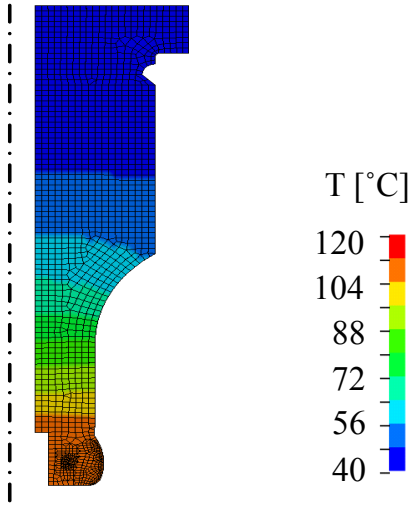

(b)

Figure 5.11: (a) 2D-axisymmetric finite element model of the ironing punch and location of the prescribed temperature boundary input nodes A and B and (b) steady-state temperature distribution in the punch.

DYNA. The resulting temperature field is shown in Figure 5.11b. The heat capacity and the thermal conductivity of the tool material Vanadis 4E were previously given in Table 5.4. The temperature of each node was saved in an output file which was subsequently used as input temperature of the punch for the transient thermo-mechanical coupled analysis.

ii. Transient thermo-mechanical analysis

The second step of the numerical analysis is based on a thermally and mechanically coupled approach of the ironing process calculating the heat generation due to plastic deformation and frictional work and the heat transfer and heat loss. In this way the temperature dependency of the mechanical properties of the workpiece and the tool can be taken into account.

The tools were assumed rigid. The overall system was assumed to be thermal-isotropic. The thermal material properties of the tool are those in Table 5.4. The input parameters for the workpiece used in the numerical model are presented in Table 5.5.

Measurements with an infrared digital temperature gun with a laser point showed an initial temperature of the workpiece of 40 °C before ironing. The accuracy of the measurement was $\pm$ 1 °C. The lower die temperature was similarly measured to be 42 °C. These values were used as input for the numerical simulations. The initial temperature distribution in the punch was taken from the steady-state analysis. The elements along the punch nose were subjected to heat transfer by flushing of the punch nose with a 30 °C lubricant. The constant HTC between lubricant and punch was 0.15 kW/(m^2·K). The constant HTC between the punch and the workpiece strip and between the die and the workpiece strip were 100

Table 5.5: Input workpiece properties used in numerical simulations [135].

Parameter		**Value**
Thermal conductivity	[W/m·K]	15
Heat capacity	[J/kg·K]	500

kW/(m^2·K) [74]. In production, the lubricant in the ironing operation is flushed over the punch before as well as after the forward stroke. Friction was modelled by means of the Coulomb friction law and a friction coefficient of $\mu = 0.04$ was selected [7], which also matches with experimental temperature measurements as seen later. The maximum shear stress applied in the Coulomb friction law was taken from the material flow stress at an equivalent strain of 0.7.

The ram speed with respect to ram displacement was given in Figure 2.5. The displacement curve in the forward and backward strokes and the corresponding velocity curve are shown in Figure 5.12. The corresponding process window, where the ironing process takes place, is identified with a blue rectangle. This determines the velocity input in the numerical analysis.

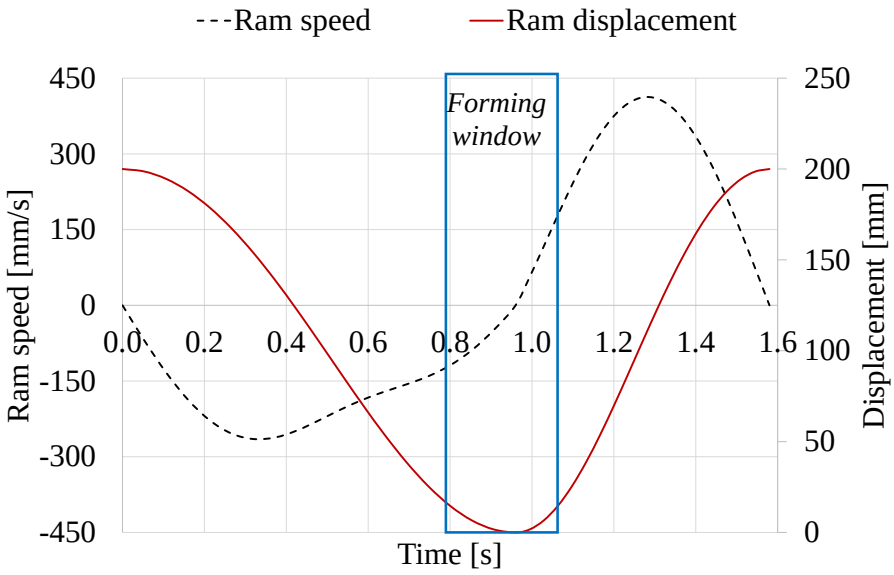

Figure 5.12: Ram speed and displacement as a function of time with identification of the ironing process window.

5.5.3 Results and discussion

Figure 5.13a shows the experimental temperature development T_B in position B. T_B increases rapidly in the beginning of the production and reaches 110 °C after 100 strokes, i.e. within three minutes. Afterwards, the temperature increases very slowly to 112 °C at 150 strokes and reaches the maximum value of 114 °C after 300 strokes. Stroke number 150 is assumed as the beginning of the steady-state regime.

The experimental measurement of three consecutive temperature cycles after stroke number 150 is shown in Figure 5.13b together with the corresponding numerical simulation. In order to take into account the elastic expansion and deflection of the lower die, its radial displacement was calculated by the numerical model using elastic tools. The lower die expands 0.03 mm radially during the forward stroke and 0.015 mm during the backward stroke. These elastic tool displacements were implemented in the model with rigid tools and the temperature T_B was calculated, since this turned out to provide a more stable temperature calculation than running with elastic tools. The output of the calculated temperature distribution in the punch was used as input for the following stroke. The calculated temperature T_B in three consecutive strokes is shown in Figure 5.13b. The difference in the maximum standard deviation between experimental and numerical temperatures is 0.04 %. Including elastic contraction of the lower die during the backward stroke predicts the temperature evaluation accurately and will be used in the parametric study in the following.

To analyse the validity of the numerical model, heat generation due to plastic deformation and friction and its effect on the temperature distribution within the workpiece and in the punch were studied. For this purpose, the simulations were performed with two friction coefficients, $\mu = 0$ and $\mu = 0.04$. The frictionless condition was chosen to determine the heat generation due to plastic deformation only. The friction coefficient $\mu = 0.04$ is the value proposed for this specific ironing application.

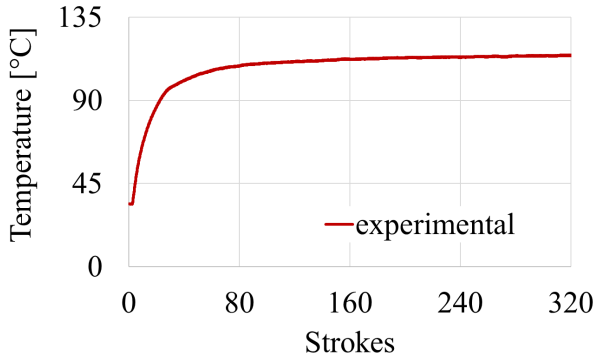

(a)

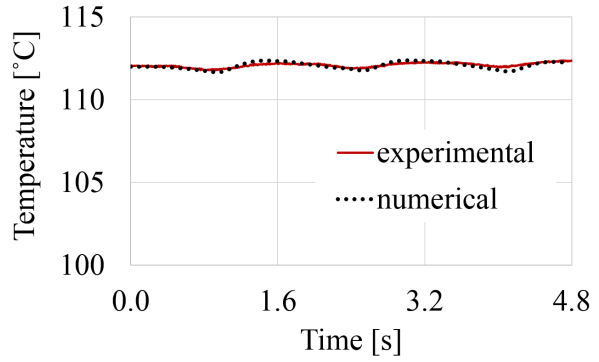

(b)

Figure 5.13: (a) Experimental temperature evolution of thermocouple B in the production test and (b) numerical and experimental temperature evolution of thermocouple B for three consecutive temperature cycles after stroke number 150.

Figure 5.14a shows the forming window in terms of the ram displacement and time when the ironing process takes place. The cross signs represent the times when the temperature values were taken from the specific nodes along the radial axis. The temperature values were read when the maximum temperature appeared during the forward stroke at $t = 0.88$ s and during the backward stroke at $t = 1.04$ s. Along the radial axis with a constant z-coordinate, four nodes in the punch and four nodes in the strip were selected. These nodes are shown with black points under each figure in Figure 5.14b and 5.14c. The temperature distributions are shown for $\mu = 0.04$.

Figure 5.14b and Figure 5.14c show that frictional heating, when $\mu = 0.04$, results in considerably larger temperature gradients along the cross section of tool and workpiece than when $\mu = 0$ with a steep rise towards the tool/workpiece contact. During the backward stroke, the temperature along the workpiece cross-section becomes more even.

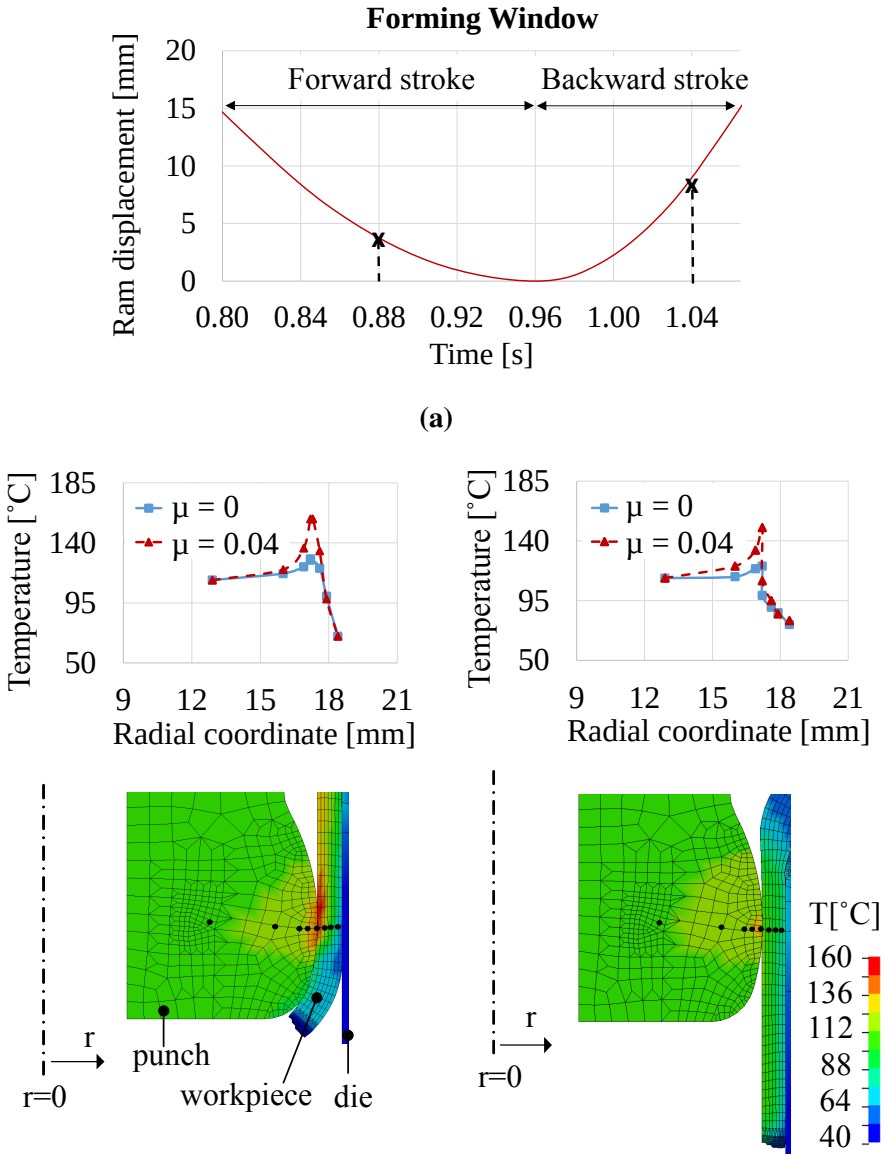

Figure 5.14: (a) Ram displacement versus time with identification of points where the temperature distributions are shown. Temperature distribution with respect to the r-coordinate during (b) forward stroke at t = 0.88 s and (c) backward stroke at t = 1.04 s.

Figure 5.15 shows the instantaneous maximum temperature along the punch contact surface as a function of time. For this specific ironing process, the thickness reduction during the forward stroke is 20 % and 4 % during the backward stroke. The contribution from deformation heating during the forward stroke should therefore be expected to be considerably higher than during the backward stroke. However, it was realised that the collar drawing results in a thinner wall at the lower edge of the workpiece, whereas the wall was thicker towards the die corner (see Figure 5.14c). As a result, higher strains and consequently higher temperatures were observed right before the ejection of the punch when t = 1.03 s.

The results show that the deformation-induced heating gives rise to a temperature of up to 130 °C during the forward stroke, while the maximum temperature during the backward stroke reaches 120 °C. The instantaneous maximum temperature curve taking both deformation and

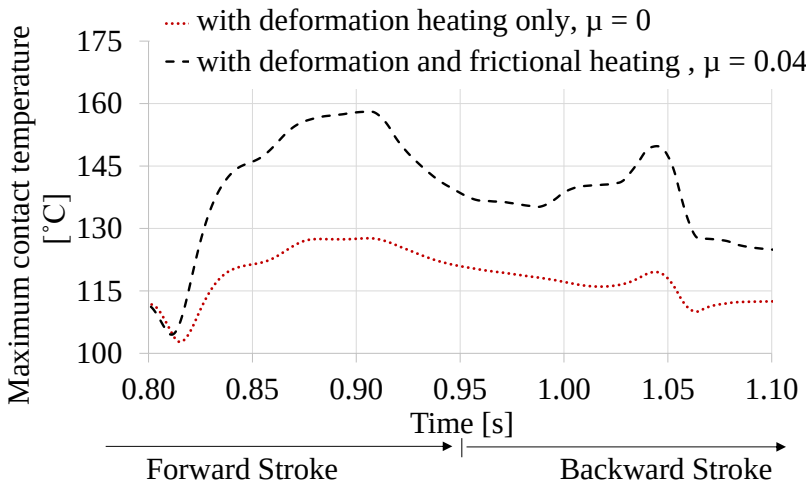

Figure 5.15: Instantaneous maximum punch temperature in the contact interface versus time obtained with deformation heating only and with deformation and frictional heating for $\mu = 0.04$.

frictional heating into account increases to a peak temperature of 158 °C during the forward stroke and 150 °C during the backward stroke.

Furthermore, the numerical model was run to analyse the temperature development within the tool at various distances from the contact surface. Figure 5.16 shows the calculated temperature of nodes B, C and D with the distances 4.375 mm, 1.3 and 0.4 mm to the contact surface, respectively. Node E is located on the surface of the punch. The temperature response of the contact node, E, is the fastest node as a consequence of the direct contact with the workpiece undergoing plastic deformation. As regards node D located 0.4 mm below the punch surface, the peak temperatures for both forward and backward strokes appear slightly later than observed in contact node E. Moving further away from node E to node C, the fluctuations are almost vanishing and replaced by a slight, monotonic increase in temperature and in node B, representing the location of the thermocouple, the temperature is almost constant.

Overall, it can be stated that the delay in the temperature response increases with the distance to the contact zone. Furthermore, while the

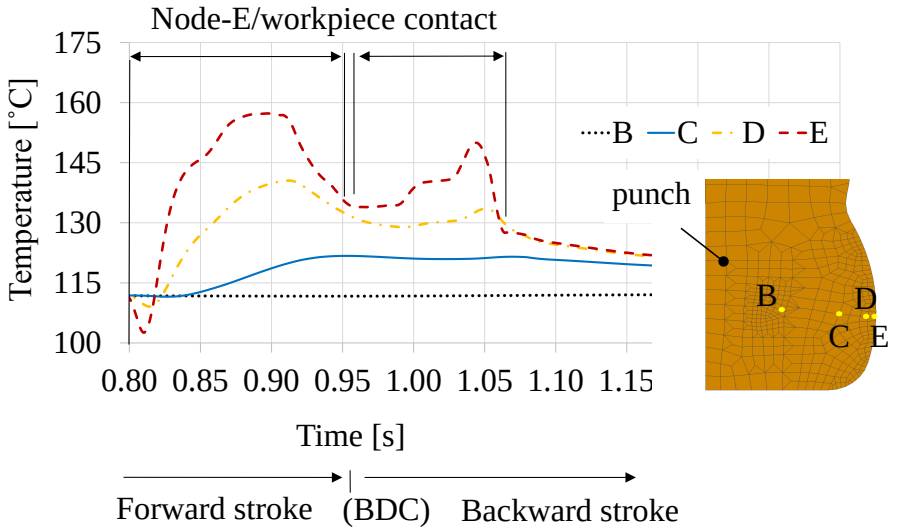

Figure 5.16: Numerical temperature evolution of nodes B, C, D and E.

temperature response and corresponding delay are significant when measured close to the contact zone, the temperature remains almost constant around the inner side of the punch including the thermocouple B region.

5.5.4 Sensitivity analysis

In the previous section, the calculated maximum contact temperature was 158 °C during the forward stroke and 150 °C during the backward stroke. This section investigates the influence of the predicted tool temperature distribution in steady-state conditions, the selected friction coefficient range and the heat transfer coefficient on the calculated contact temperature.

Influence of predicted steady-state tool temperature distribution

The calculated steady-state temperature distribution in the punch was given in Figure 5.11b. As indicated before, a constant temperature of 40 °C was assigned to the nodes along the punch base. The referred nodes in the upper region are marked in yellow within the rectangular box in Figure 5.17a. The steady-state temperature distribution of the punch was recalculated by assigning two new punch base temperatures, 28.2 °C and 50 °C. These values were selected as extrema, since the environmental temperature in the production was 28.2 °C and the maximum temperature at the tip of the punch nose two seconds after the production stop was measured to be 50 °C. After obtaining the steady-state temperature distribution of the punch adopting the two new boundary temperatures, 28.2 °C and 50 °C, the thermo-mechanical calculation was performed again with the new, corresponding initial punch temperature distributions.

Figure 5.17b shows the maximum interface temperature along the punch nose with respect to time after ironing starts until the end of contact. The two new boundary conditions are compared with the earlier one of 40 °C. The results indicate that the temperature of the punch base does not have

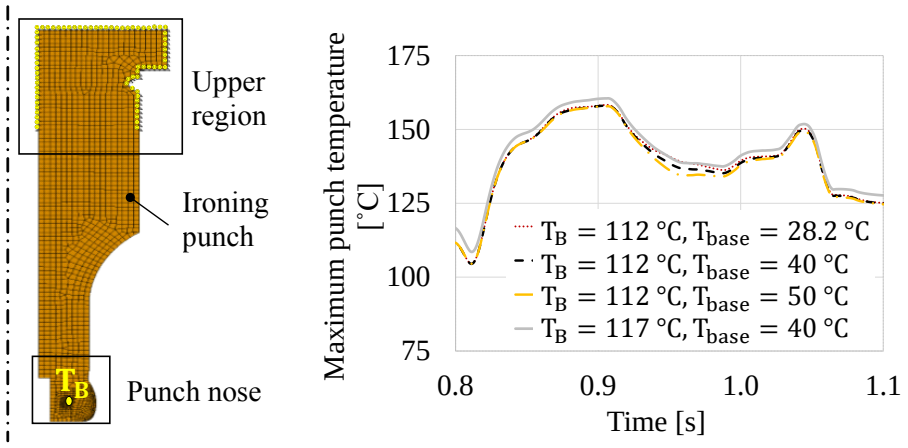

(a) **(b)**

Figure 5.17: (a) 2D-axisymmetric finite element model of the ironing punch with prescribed boundary nodes for temperatures indicated in yellow and (b) instantaneous maximum punch temperature in the contact interface versus time obtained with different predicted steady-state punch temperature boundary conditions.

any significant effect on the maximum punch temperature.

To ensure the repeatability of the experimental results, the temperature in production was measured again. The steady-state temperature T_B was 117 °C, while it was previously 112 °C. The steady-state temperature distribution in the punch was recalculated by assigning a temperature of 117 °C in node B, which is indicated with a yellow dot in the punch nose region in Figure 5.17a. A recalculated temperature distribution was used as input to the thermo-mechanical model. All other parameters were the same. Figure 5.17b shows that an increase of T_B has a larger effect on the maximum contact temperature than an increase of the temperature in the punch base. The peak contact temperature increases around 2 °C when T_B is raised from 112 °C to 117 °C in the steady-state analysis.

Influence of the friction coefficient

In the previous calculations, a friction coefficient of $\mu = 0.04$ was assumed. To investigate the influence of the friction coefficient, FEM simulations were carried out with two alternative values: $\mu = 0.03$ and $\mu = 0.05$.

Figure 5.18a shows the numerically computed temperature of node B versus time and the corresponding experimental temperature curve. The

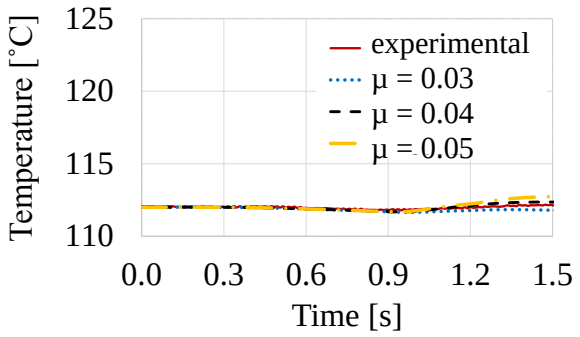

(a)

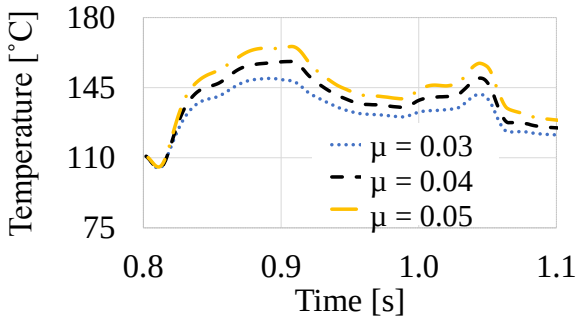

(b)

Figure 5.18: (a) Numerical and experimental temperature evolution at thermocouple B and (b) maximum contact temperature evolution with the following friction coefficients: $\mu = 0.03$, 0.04 and 0.05.

numerical simulations show that a friction coefficient of $\mu = 0.05$ overestimates the temperature increase, whereas $\mu = 0.03$ results in a lower temperature increase than experimentally measured. Although the current study suggests that the friction coefficient is $\mu = 0.04$, one may claim that depending on the model assumptions and other process parameters, the friction coefficient may change slightly. However, in this study the main interest is to determine the contact temperature. Figure 5.18b shows that the maximum temperature of the punch surface is $158 \pm 8\,^{\circ}\mathrm{C}$ in the forward stroke and $150 \pm 6\,^{\circ}\mathrm{C}$ in the backward stroke, when the friction coefficient is in the range of $0.03 \leq \mu \leq 0.05$.

Influence of heat transfer coefficient

To investigate the influence of the HTC, calculations were performed with three different values: h = 50, 100 and 150 kW/(m^2·K). The selection of HTCs was based on the values proposed by Olsson et al. [74], who investigated a single-stroke strip reduction test at various reductions. The assumption of a constant HTC along the tool/workpiece interface is considered acceptable since the HTC is insensitive to the pressure in forging above a threshold pressure as shown by Burte et al. [136] for a deformation process with a pressure range similar to that of the present ironing. The friction coefficient was $\mu = 0.04$, and as Burte et al. [136] have found, the effect of the friction coefficient on the HTC calibration curves is small. The heat transfer and the friction may therefore be decoupled in the sensitivity analysis.

In Figure 5.19a, the numerically computed temperature curves of node B versus time and the experimental temperature curve are given. The overall temperature distribution inside the punch at the thermocouple position is not sensitive to the changes in HTC. Figure 5.19b shows the instantaneous maximum punch temperature. The results indicate that the instantaneous contact temperature increases slightly with increasing HTC. The peak temperature along the interface of punch/workpiece is $158 \pm 1\,^{\circ}\mathrm{C}$ during the forward stroke and $150 \pm 1\,^{\circ}\mathrm{C}$ during the backward stroke. In general, the HTC affects the peak temperature only slightly. Since the transient thermo-mechanical analysis starts with a pre-

viously calculated temperature distribution corresponding to the steady-state, the HTC has less effect on temperature increase at higher speeds.

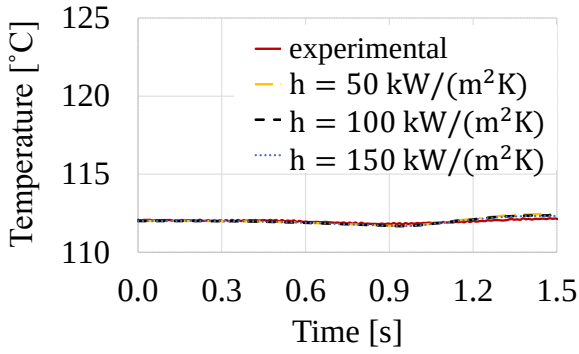

(a)

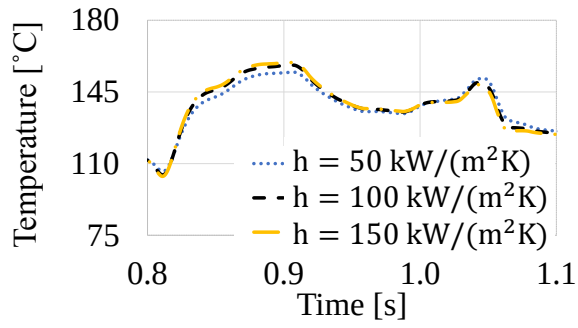

(b)

Figure 5.19: (a) Numerical and experimental temperature evolution at thermocouple B and (b) maximum contact temperature evolution with the following heat transfer coefficients: h = 50, 100 and 150 kW/(m^2·K).

5.6 Identification of the tribo-parameters

Chapter 4 and the current Chapter 5 present a systematic approach on how to analyse a given production process of a progressive die sequence before off-line laboratory testing. A combined finite element analysis and experimental measurements were used to determine tool/workpiece interface pressure and temperature of the critical station, whereas other tribologically important parameters such as sliding speed, sliding length and tool roughness were predefined. These identified parameters will later be used in off-line testing of various tribo-systems. Critical tribo-parameters can be summarised in three main categories: process parameters, analysis of pressure distribution and analysis of tool/workpiece interface temperature.

The normal pressure on the punch nose is around 1050 MPa during the forward stroke. During the backward stroke, the normal pressure reaches up to 2050 MPa. This is due to large strain hardening after the main wall reduction. Elastic contraction of the lower die results in additional reduction during ejection of the punch, and very small contact length between the workpiece and die leads to large pressure gradients especially at the end of the backward stroke where the local wall thickness is relatively larger.

Combined experimental and numerical analysis was conducted to determine the heat transfer coefficient between an AlCrN-coated tool steel and a mineral oil used for the industrial case study. An inverse analysis suggested that the heat transfer coefficient in unloaded conditions at 80 °C oil temperature is 0.15 kW/(m^2·K). In thermo-mechanical analysis, the determined heat transfer coefficient was used for the boundary where no workpiece contact appears. Finally, the thermo-mechanical analyses revealed that the peak temperature in the tool/workpiece interface is approximately 158 °C in the forward stroke and 150 °C in the backward stroke.

CHAPTER 6

Analysis of the Laboratory Test Platform

This chapter deals with the experimental and numerical analysis of the laboratory test platform. The developed comprehensive test set-up, emulating the production platform, was previously described in detail in Chapter 3. This chapter presents the modifications and further improvements in the test set-up for conducting experiments at elevated temperature. First, the mechanical numerical model is introduced and the determined contact pressure is presented. Afterwards, the developed thermo-mechanical numerical model is described and the calculated interface temperature between the tool and workpiece is discussed. The chapter is finalised with a summary including the identified tribo-parameters.

6.1 Numerical model

The numerical model is based on LS-DYNA implicit analysis version R9. For the modelling of 2D SRT, plane strain deformation was assumed. The discretised finite element model is shown in Figure 6.1. The tool pins were modelled as elastic material. The initial thickness of the strip was 1 mm. The stress-strain curve of the strip material and other mechanical material properties given in Chapter 4.1.1 were further used in this model.

The overall tooling system and the blank were discretised by approximately 3600 and 9600 elements, respectively. The aspect ratio was kept close to 1. The mesh towards the tool/workpiece interface was refined and it is shown in the detailed view of Figure 6.1.

The constraints of the tools were defined for a few nodes around the

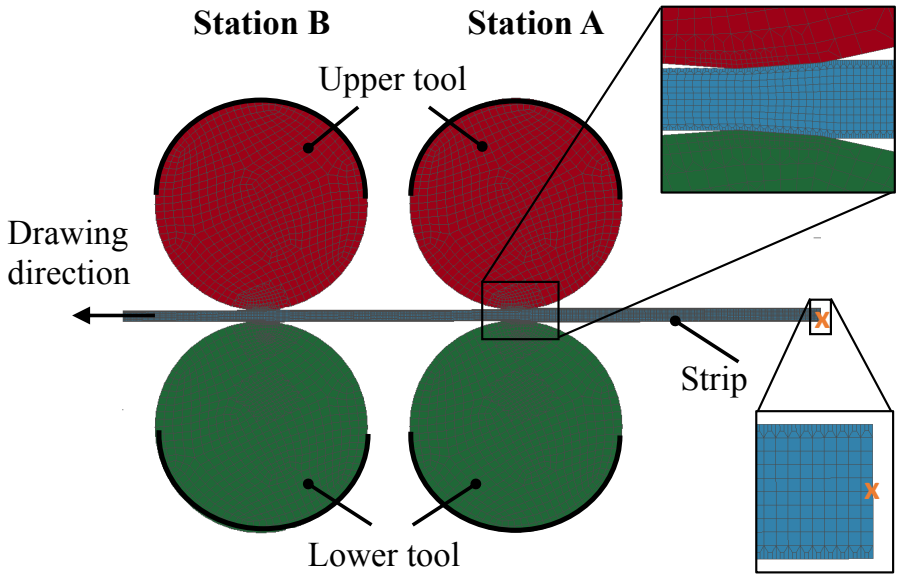

Figure 6.1: 2D model of SRT with detailed view of the contact interface.

outer periphery of the tool as shown with black semicircles in Figure 6.1. Displacement curves were defined for the upper tools to achieve the 20 % thickness reduction at Station A and 4 % at Station B. In order to reduce the workpiece thickness by 4 % at Station B, it was necessary to deform the strip initially. For that, in an initial numerical model that uses only Station A, the strip thickness was reduced from an initial thickness of 1 mm to 0.8 mm. The strain distribution of the strip obtained through this initial model was then used as input in the model shown in Figure 6.1. The strip front edge was pulled 10 mm from the right to the left. In order to prevent the right end of the strip to move freely, y-translational motion of the middle node of the strip taken from the rightmost end was constrained (see detailed view in Figure 6.1).

In accordance with the previous sensitivity analysis given in Chapter 4.3, the penalty scale factor sfact was selected as 1.

The coefficient of friction was determined in two steps. First, the experiment and the simulation with Station A was performed. The coefficient of friction was calibrated to obtain a match between the experimental and numerical drawing forces. As seen from Figure 6.2 when the friction

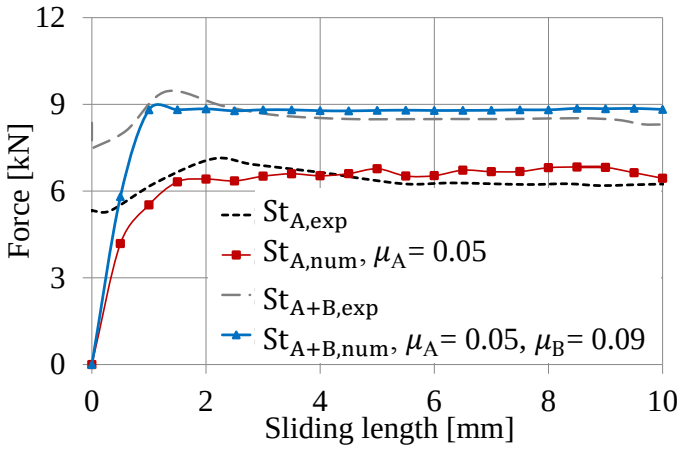

Figure 6.2: Comparison of numerical and experimental drawing force obtained by using Station A only and Station A and Station B together.

coefficient is $\mu = 0.05$, the numerically calculated drawing force is very similar to the experimentally measured curve. Secondly, the experiments with both stations were performed. In the numerical model, using both stations, the friction coefficient at Station A was fixed to $\mu = 0.05$. The friction coefficient at Station B was then calibrated. As seen from Figure 6.2, the numerically calculated and experimentally measured drawing forces are in good agreement when the coefficient of friction μ at Station B is 0.09. The maximum shear stress applied in the Coulomb friction model was taken from the material flow stress at an equivalent strain of 0.3.

Figure 6.3 shows the maximum contact pressure at the tool/workpiece interface of Station A and B for a single stroke. The calculated values were taken from the three elements with the highest normal pressures. The numerical calculations reveal that the normal pressure on the tool pin at Station A that emulates the forward stroke of the ironing operation is around 1100 MPa. This value is very close to 1050 MPa which was

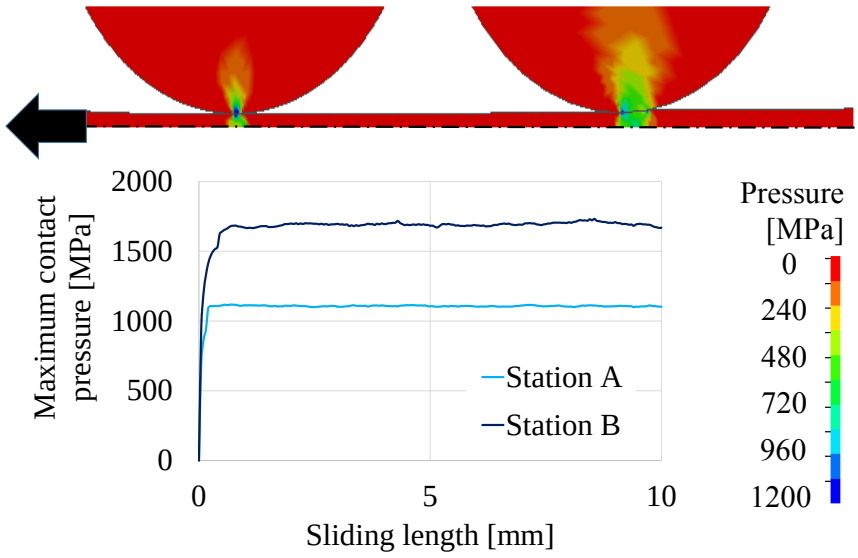

Figure 6.3: Calculated maximum value of tool/workpiece interface pressure during SRT.

found in production (refer to Chapter 4).

At Station B, which emulates the backward stroke, the normal pressure reaches up to 1700 MPa. It may be explained by the small contact area at Station B and higher flow stress of the strip due to strain-hardened material after the main wall reduction that takes place at Station A. Yet, it is somewhat lower than the normal stress found in the backward stroke of the industrial ironing operation in which the normal pressure reaches up to 2000 MPa (refer to Chapter 4). This is mainly due to the fact that in production, the short contact length between workpiece and die leads to large pressure gradients, especially towards the end of the backward stroke where the local wall thickness is relatively greater.

6.2 Design for experiments at elevated temperature

The combined numerical and experimental methodology, similar to the one used for the analysis of the production case, was adopted to determine the tool/workpiece interface temperature. Firstly, the tool set-up was modified to perform experiments at high temperature. Then, the experimental measurements taken from several positions within the tool were used as input for the thermo-mechanical numerical model. Finally, the interface temperature was determined. The modified experimental set-up, thermo-mechanical model and the results of the numerical calculations are discussed in the following.

6.2.1 Positioning of the thermocouples

Figure 6.4 shows the temperature measurement locations in the lower tool pin and the tool pin support. For simplicity, the tool pins are de-

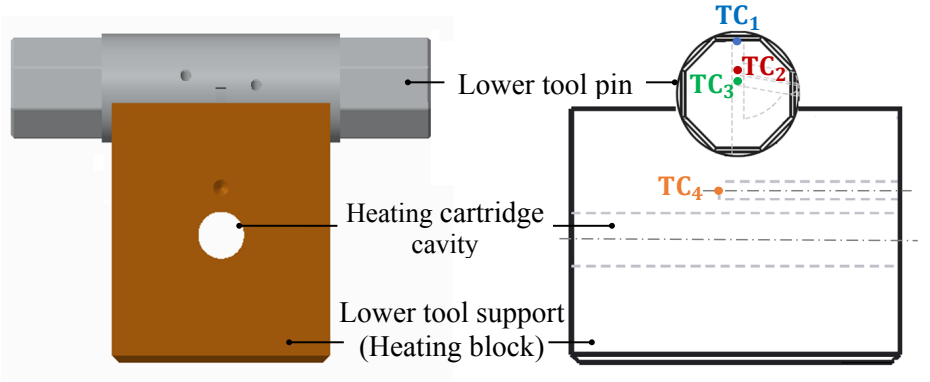

Figure 6.4: Temperature measurement positions in SRT tooling.

signed to be heated through the lower tool support, which includes a hole for a heating cartridge. Thermocouple holes were therefore designed for the lower tool pins and the lower tool support. Similar to the production tests, multiple thermocouple holes located at various positions were introduced. They are shown in Figure 6.4. The distances from the lower tool pin/workpiece interface to the thermocouple measurement points TC_1, TC_2 and TC_3 are 1.2 mm, 4.4 mm and 5.7 mm, respectively. The holes were machined by EDM to ensure flat bottoms of the holes. For the detailed dimensions, refer to the technical drawing in Appendix D.

6.2.2 Preheating

Preheating the strip

The measurements in production suggested that the strip temperature before entering the ironing station is 40 ° C. For preheating the strip, a heating gun was utilised. After preliminary trials, it was decided to place the heat gun at the entrance of the strip to the tribotester, before the strip goes through the first set of guiding rolls as shown in Figure 6.5. The actual temperature of the strip was ensured via measurements taken from both a tactile thermometer and an infrared thermometer.

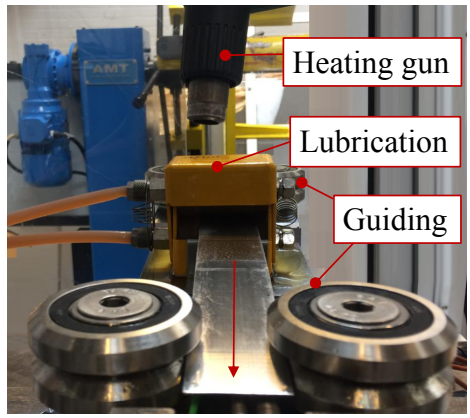

Figure 6.5: Set-up for heat gun placement.

Preheating the tool

In order to perform the tests at a temperature corresponding to the production, the tool pins have to be heated. Initial tests were carried out to determine the capability of the current SRT design. A heating cartridge was inserted in the lower die support and the temperature was increased step by step up to 230 °C. The thermocouples were placed in the holes presented in Figure 6.4. The overall final set-up is shown in Figure 6.6a. Figure 6.6b presents the temperature evolutions read by each thermocouple. The results conclude that the temperature in the tool (TC_1, TC_2 and TC_3) reaches only 60 °C after 20 minutes. The periodic increase in the temperature measured by TC_4 took place due to manually adjusted target temperature input. The initial preheating test revealed that with the above-given design, heat dissipates mainly to the base block on which the lower tool support is mounted. As a result, the tool cannot be preheated to above 100 °C efficiently and rapidly.

A solution may be using a heating cartridge with higher heating capacity or alternatively, the heated parts can be isolated from the rest of the design.

To test whether or not the isolation would solve the problem, before

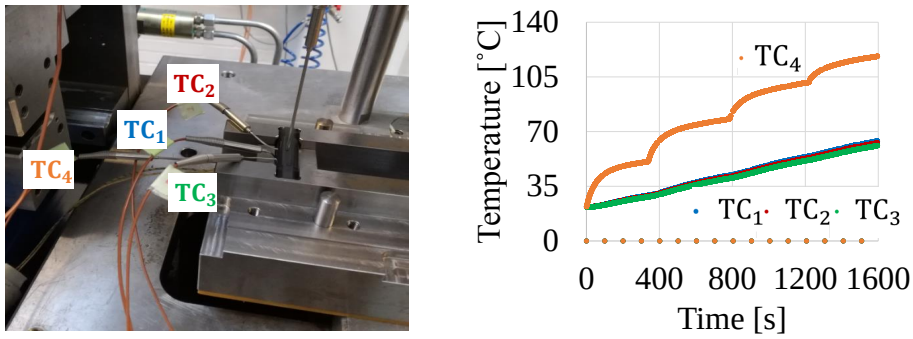

(a) (b)

Figure 6.6: (a) Picture of set-up with inserted thermocouples and (b) temperature evolution at the thermocouple measurement points during preheating.

changing the heating cartridge design, preheating of the lower tool support and the tool pin was performed in an isolated environment by separating them from the rest of the SRT tooling. The heating cartridge was heated up to 250 °C. The results shown in Figure 6.7 conclude that it is possible to preheat the lower tool pin to above 200 °C in less than 10 minutes.

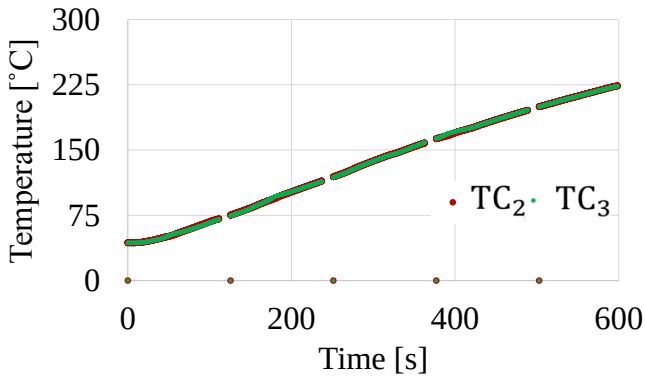

Figure 6.7: Temperature evolution at the thermocouple measurement points during preheating with an isolated set-up.

The overall final design of the SRT tool is shown in Figure 6.8a. In the final set-up, the lower tool support, indicated in Figure 6.8b by the red box, was fabricated in brass MS 58, providing higher thermal conductivity. Furthermore, isolating plates made from the HASCO-Z121 series thermal sheets were used for thermal isolation. The dimensions of the lower tool support were changed to enable the insertion of isolation plates to the sides and the bottom of the base (see Figure 6.8b and 6.8c).

Figure 6.8c shows the lower tool pin sitting on the support and three thermocouples mounted inside the tool pin. The heating cartridge was inserted in the tool support. All the thermocouples and the heat cartridges were coated with thermal paste before insertion to secure a high level of heat transmission.

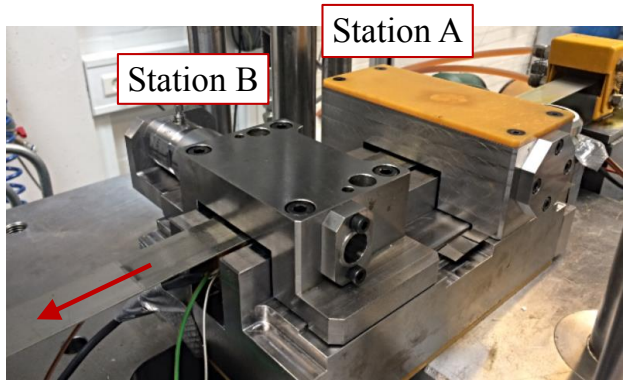

(a)

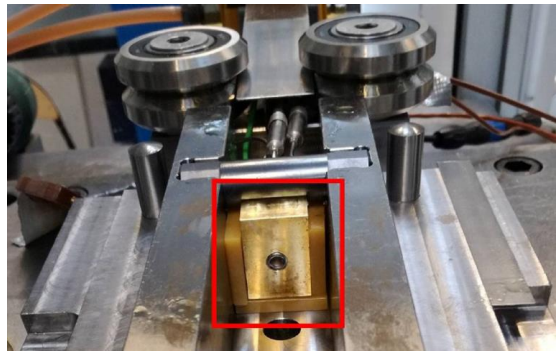

(b)

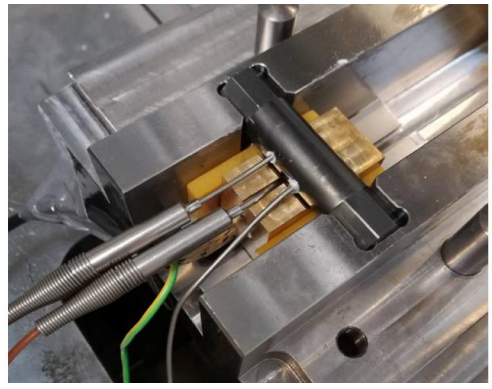

(c)

Figure 6.8: Picture of (a) the back of the tool with stations A and B, (b) the final set-up for lower tool support (heating block) and (c) Station B with inserted thermocouples.

6.2.3 Automated tool temperature control

The set-up used for testing at elevated temperature takes advantage of a PID controller to control the temperature accurately. The block diagram of the control loop used for heating the tool is given in Figure 6.9. The PID controller receives the measured temperature and compares it to the set temperature. The relay allows the current flow to the heating cartridge whenever it is needed. The power is supplied through an isolated transformer for safety. The isolation transformer enables adjusting the voltage between 0-230 V.

Analysis of the production line revealed that the temperatures during the forward and backward strokes are different. Therefore, it is necessary to control the temperature at Station A and Station B separately. Figure 6.10a shows the PID unit for temperature control. First, the temperatures are set to the desired value. Afterwards, the power is provide to the trans-

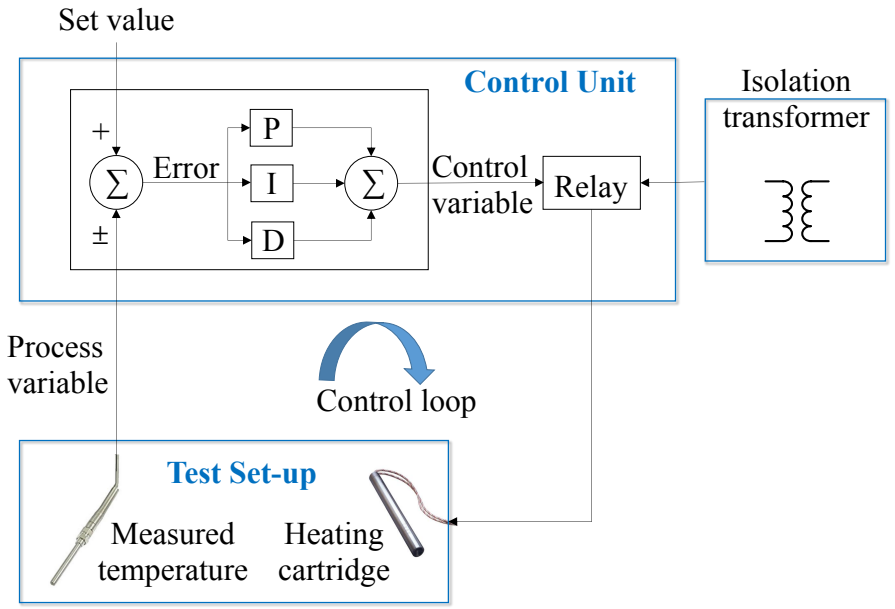

Figure 6.9: Block diagram of the tool heating system.

former and the voltage is adjusted. A picture of the isolation transformer is given in Figure 6.10b. Through the interface in the PID controller, it is possible to read the measured temperature throughout the experiments. The set and the measured temperatures in Figure 6.10a were chosen for illustrative purposes.

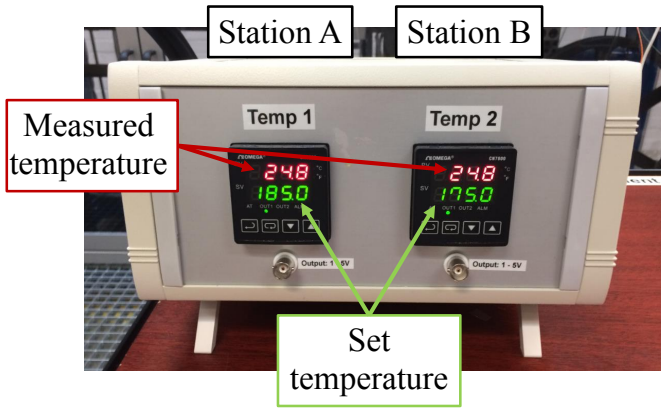

(a)

(b)

Figure 6.10: Picture of (a) the PID controller for Station A and Station B and (b) the isolation transformer.

6.3 Thermal analysis of the strip reduction test

6.3.1 Preliminary testing at elevated temperatures

In order to determine the desired tool/workpiece interface temperature, it is necessary to predict the preheating tool temperature. The methodology followed for the prediction of the preheat temperature is given in Figure 6.11. It starts with an initial tool preheating temperature and followed by performing the experiment with the initial estimation. Measured temperatures during the experiment, taken from various points are then used in thermo-mechanical numerical analysis to calculate the interface temperature between tool and workpiece. If the contact temperature is around the one determined in the production tool in Chapter 5, i.e. 160 °C, it means that the initially estimated preheating temperature

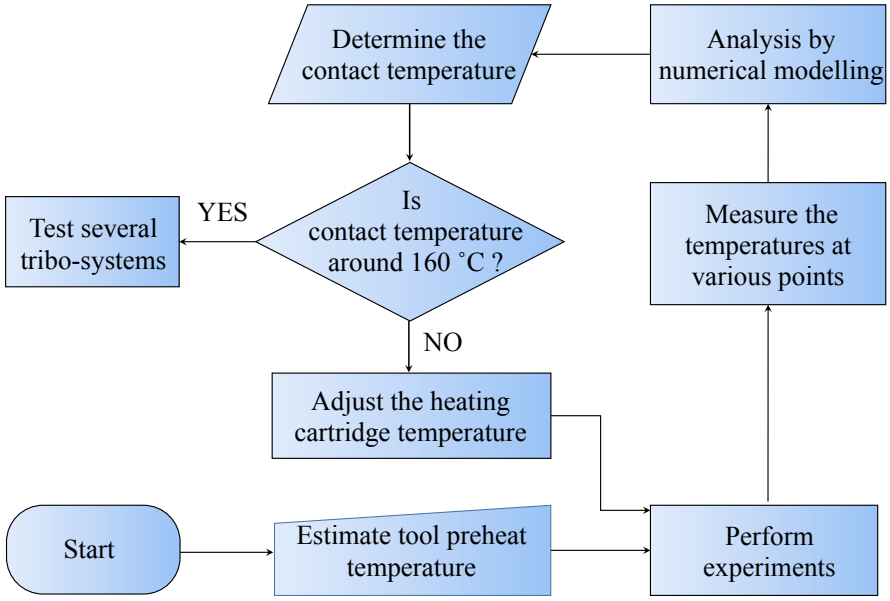

Figure 6.11: Flow chart for determination of tool/workpiece contact temperature.

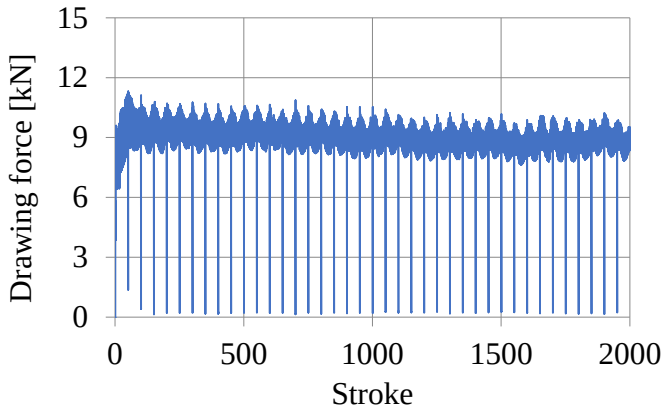

Figure 6.12: Measured drawing force as a function of the stroke number for the tribo-system using TDN 81 oil.

is adequate for further testing of candidate tribo-systems.

As an initial assumption, the preheating temperature of both stations was estimated as 140 °C. The tools were heated from room temperature to 140 °C as soon as the experiments begin.

In order to ensure stable process conditions without lubricant film breakdown, experiments were carried out with Iloform PN 226, a mineral oil with chlorine-based EP additives. The experiments were performed with both stations and 2000 strokes. Similar to the production, the test rate was 38 spm and the sliding length was 10 mm.

Figure 6.12 shows the evolution of the drawing force. The drawing force follows a stable pattern throughout the experiment with no indication of lubricant film breakdown.

In Figure 6.13 measured temperatures inside the tools at Station A and Station B are given. The controlled temperature by PID was TC_3. In both stations, the temperature evolutions at the TC_1 and TC_2 positions been acquired during the experiments. The position of the each of the thermo-

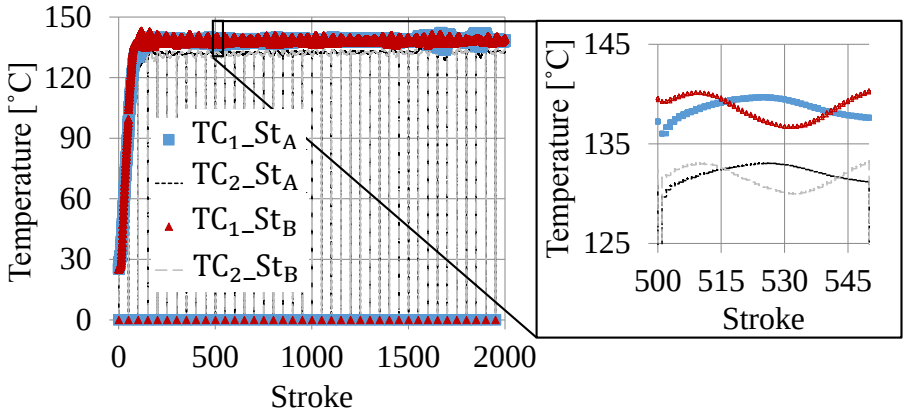

Figure 6.13: Measured temperature as a function of the stroke number for the tribo-system using TDN 81 oil and detailed view of 50 consecutive strokes after a homing operation.

couples was provided in Figure 6.4. The temperatures within the lower tool pins rise from room temperature to above 130 °C within 150 strokes. In both Station A and B, the measured TC_1s reach 140 °C, whereas TC_2s rise up to 133 °C. These values will be used in the numerical model to predict the tool/workpiece interface temperature.

The detailed view of 50 consecutive strokes, given in Figure 6.13, presents a sinusoidal behaviour of all measured temperatures. The reason is probably the PID control set-up which turned on and off the current supply for the heat cartridge to keep the controlled temperature of TC_3 at 140 °C.

6.3.2 Thermo-mechanical numerical model

For determination of the interface temperature, the previously developed mechanical model was extended by a thermal coupling. The thermal process parameters were summarised in Table 5.4 and Table 5.5.

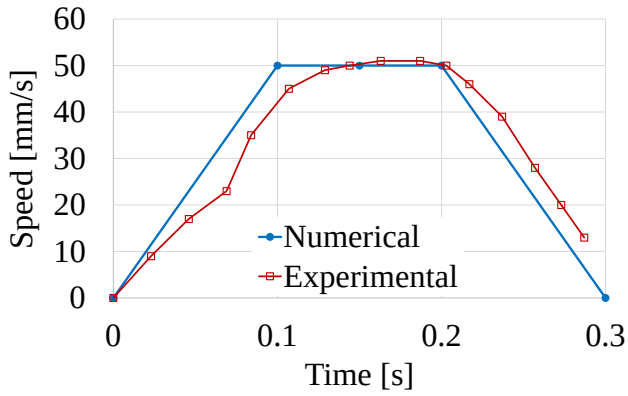

Figure 6.14: Experimental and numerical drawing speed for one stroke in SRT.

In the thermal analysis, an accurate definition of the speed curve is important. For 10 mm sliding length, it was necessary to have a short acceleration time to achieve the high speed, varying from 140 mm/s to 220 mm/s, which was identified for the industrial case. However, preliminary tests showed that short acceleration time results in fluctuations in speed and complicates the performance of the tribotester. To have a stable process, the speed during SRT was limited to 50 mm/s while fixing the sliding length to 10 mm and the test rate to 38 spm. The acceleration and deceleration time were 100 ms. The speed curve used as input in numerical modelling and the actual speed curve measured experimentally are given in Figure 6.14.

Another critical parameter in the thermal analysis is the distance between the two stations because the strip temperature when entering Station B depends on the distance from the first set of tool pins at Station A as it directly affects the dissipated heat. Considering the fact that the distance between the two stations is longer than 150 mm, such a modelling requires a discretisation of a long strip which results in high memory and CPU time. Hence, to simplify the model, Station A and Station B were analysed in two separate models.

For both stations, the temperature of the TC_1, TC_2 and TC_3 were defined as input boundary conditions and fixed to the following experimentally measured values: 133 °C, 140 °C and 140 °C, respectively. The lower periphery of the tool pin, indicated with a black window in Figure 6.15, was assigned to 160 °C. This initial estimation was based on the temperature measurement of TC_4, positioned just above the heating cartridge in the lower tool support (refer to Figure 6.4), reaching up to 170 °C. The initial temperature distribution within the lower tool pins were therefore calculated in the beginning of the thermo-mechanical analysis as shown in Figure 6.15.

The initial temperature of the workpiece strip before the forward stroke was 40 °C. The temperature of the strip before entering the Station B was measured as 70 °C and this information was used for numerical modelling of Station B. Initial temperature of the upper tool pin was assumed to be 130 °C. This assumption was based on the upper limit of the lower tool/strip contact temperature of 160 °C at a steady-state and a lower limit of the strip temperature of 70 °C. When modelling with two extremes, the lower tool/strip interface temperature changes less than 4 %.

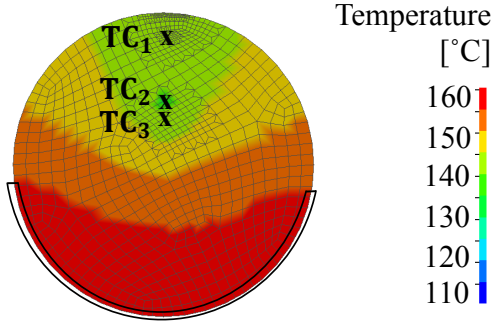

Figure 6.15: Temperature field in the lower tool pin obtained from steady-state analysis. The boundary nodes with an assigned temperature are enclosed by the black window and the crosses.

The constant heat transfer coefficients between the tooling and the workpiece strip was 100 kW/(m^2·K). As the tool pins are sitting in housing blocks and the whole system is heated, the effect of heat transfer to the air and lubricant were neglected. The friction coefficient at Station A was $\mu = 0.05$ and $\mu = 0.09$ was defined at Station B.

6.3.3 Determination of the contact temperature

Based on the above-given thermo-mechanical model, the tool pin/strip interface temperature was calculated. As the tool pins were heated from the bottom, the attention was paid to the contact of the workpiece with the lower tool pin.

Figure 6.16 shows the calculated maximum temperature along the interface of the lower tool pins at Station A and Station B with respect to contact length. The workpiece is drawn from right to left passing through Station A and Station B. Contact position of 0 mm corresponds to the position where the strip exits the tool pin.

The numerical analysis indicates that the interface temperature between the lower tool pin and the workpiece at Station A is lowest at the entry of the strip into the contact zone and increasing towards the strip exit zone. This is due to the increasing deformation of the strip from entrance to exit. Finally, based on the numerical calculations, it can be concluded that the maximum temperature is above 160 °C at Station A. This value is similar to the one found in production during the forward stroke (refer to Chapter 5).

A similar tendency has been observed for the temperature distribution at the contact zone in Station B. However, the drop in temperature with respect to contact position is slightly less compared to the drop observed at Station A. One reason may be that at Station B, the contribution of deformation heating is very limited due to small thickness reduction, up to 4 %. Therefore, the temperature at the interface of Station B is limited

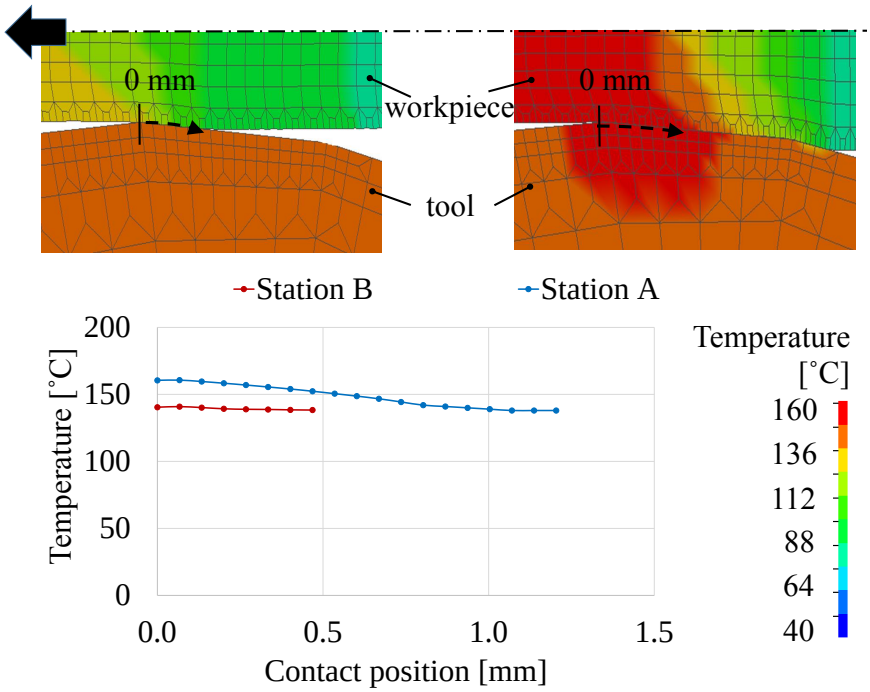

Figure 6.16: Maximum temperature along the tool/workpiece surface during SRT.

to 140 °C, which is close to the preheating temperature.

6.4 Identification of the tribo-parameters

Critical tribo-parameters of the industrial case study were previously identified under three headlines: process parameters, tool/workpiece contact pressure and tool/workpiece contact temperature. A similar procedure was implemented during the analysis of the SRT. In the following, a summary of the identified tribo-parameters of the SRT are given.

The process parameters used during testing and modelling were based on the production case and are summarised in Table 6.1. The test rate

Table 6.1: Process parameters for SRT.

Parameter		Value
Test rate	[spm]	38
Reduction at Station A	[%]	20
Reduction at Station B	[%]	4
Sliding length	[mm]	10
Sliding speed	[mm/s]	50

was 38 spm. The strip thickness was reduced by 20 % at Station A, and an additional reduction of 4 % was applied at Station B. The strip was drawn 10 mm with a speed of 50 mm/s in each stroke.

To calculate the contact conditions, a 2D numerical model was developed. The main goal of the modelling was to determine the pressure and the temperature at the tool/workpiece interface at Station A and B.

A mechanical model was used to calculate the interface pressure. It was found that at Station A, emulating the forward stroke, the interface pressure between tool pin and workpiece increases to 1100 MPa. At Station B, the work-hardened workpiece material and the short contact length give rise to an increase in the normal pressure. As a result, the local pressure at the tool/workpiece interface reaches up to 1700 MPa.

Finally, a thermo-mechanical analysis revealed that preheating the tool at Station A enables the SRT to emulate the industrial process to achieve an interface temperature of 160 °C. With the same preheating temperature at Station B the interface temperature is around 140 °C, i.e. somewhat lower than the one found in production. One reason for the higher temperature in production is that the thickness reduction is actually increasing with punch displacement during the backward stroke.

To conclude, the proposed off-line methodology for emulating industrial ironing operations has been developed successfully. In fact, the developed methodology, including the experimental and numerical set-up and procedures, can be used to emulate any other industrial ironing operation.

CHAPTER 7

Strip Reduction Test Campaign

This chapter is dedicated to a more comprehensive test campaign using the developed SRT tool. The performance of several tribo-systems are evaluated in the following sections. After selecting a good candidate, the experiments performed at elevated temperature are given and the results are discussed. Furthermore, the identified differences between the laboratory and the production platform are presented and several improvements are proposed.

7.1 Testing of selected tribo-systems

Tribo-system candidates were previously identified in Chapter 2.4.2. Although the main objective of the study is to develop a methodology based on an industrial case study, the development of a new collaborative partnership during the project and Grundfos A/S's interests caused a number

of new tribo-systems to be identified.

In order to evaluate the performance of the alternative lubricants, preliminary tests were performed by SRT with Station A only. The process parameters were summarised in Table 6.1. Unless otherwise mentioned, the same parameters were used throughout the entire, comprehensive testing campaign.

The first test campaign was conducted to evaluate the performance of several environmentally friendly lubricants. In addition to the current lubricant Rhenus LA 722086, the proposed lubricants were IRMCO 980-323, -156 and -080. Figure 7.1 shows the drawing force with respect to the number of strokes for the four lubricants. The experimental results revealed that none of the alternative lubricants of IRMCO were able to perform successfully due to increase in the drawing force. In fact, lubricant film breakdown initiated from the very beginning. It may be related to the lower viscosity of the water-based lubricants. Due to high contact pressure, the lubricant was squeezed out and pure metal-to-metal contact was introduced. As a result, heavy scoring along the strip surface oc-

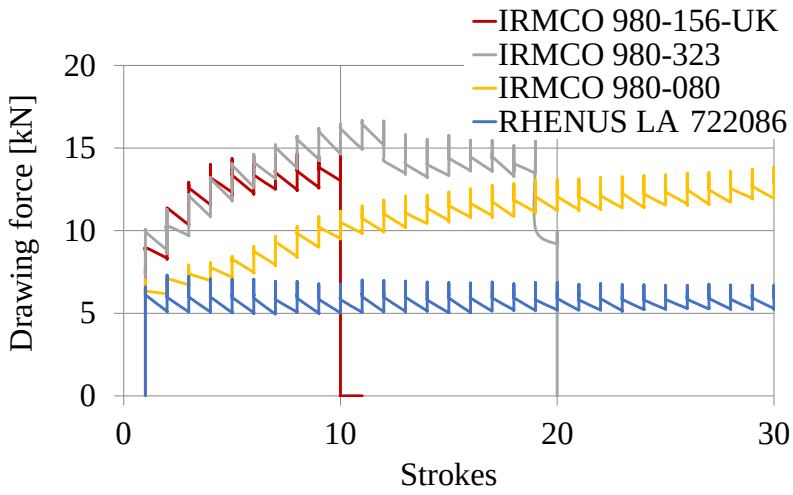

Figure 7.1: Performance of various environmentally friendly lubricants.

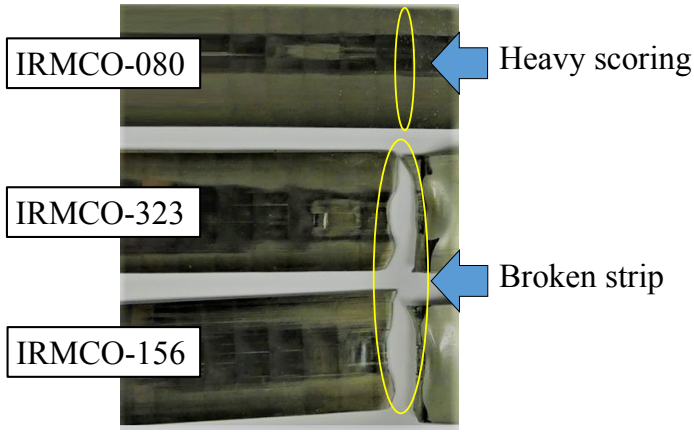

Figure 7.2: Picture of the strips with reduced thickness after using various environmentally friendly lubricants by testing with Station A only.

curred and the strip eventually broke (see Figure 7.2). The sudden drop in drawing force shown in Figure 7.1 indicates breaking of the strip.

Although none of the newly proposed tribo-systems are able to run successfully, the initial tests have shown that the tribo-system with the Rhenus LA 722086 lubricant can run for thousands of strokes without lubricant film breakdown at room temperature (refer to Figure 3.12b).

The next step in the off-line test campaign was to run the experiments with the Rhenus LA 722086 lubricant at elevated temperature, using both stations to emulate the entire industrial case study. In order to emulate such conditions, the tools were heated from room temperature to 140 °C, as proposed in Chapter 6. Figure 7.3a shows the drawing force with respect to number of strokes. In addition to Rhenus LA 72208, the result obtained previously for TDN 81 oil are shown as a reference force due to the fact that TDN 81 oil has run successfully at high temperature.

Figure 7.3b shows the temperature measurements with the thermocouples positioned in the tool when using Rhenus LA 722086. Two pairs of

thermocouples, TC_1 and TC_2, were inserted in the lower tool pin at Station A and B. The positions of the thermocouple pairs were previously given in Figure 6.4.

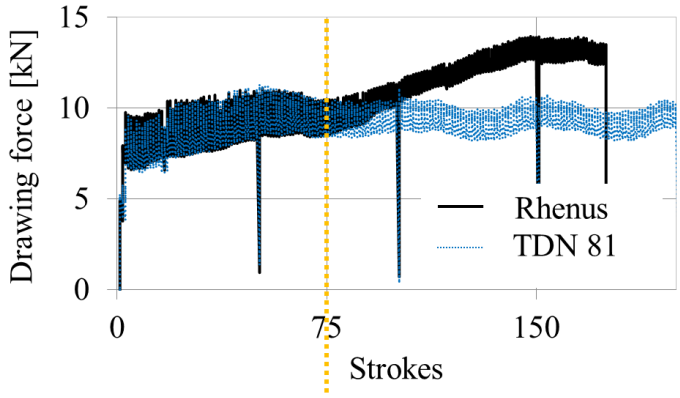

(a)

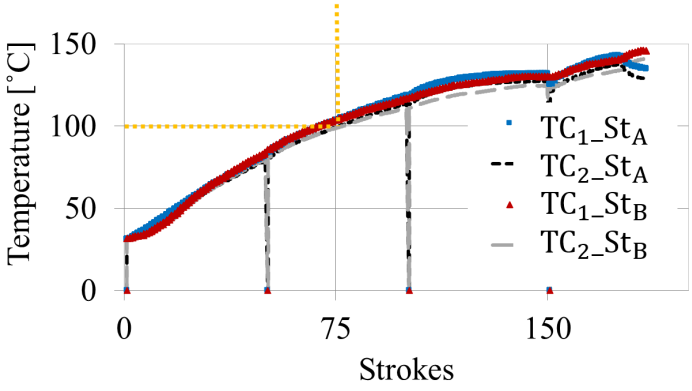

(b)

Figure 7.3: Measured (a) drawing force as a function of strokes for the tribo-system using Rhenus LA 722086 and TDN 81 as a reference oil and (b) temperature as a function of strokes for the tribo-system using Rhenus LA 722086 oil.

The temperature of TC_1 is higher than that of TC_2 at both stations as TC_1 is closer to the interface between the tool and strip. Figure 7.3a shows that after 175 strokes the strip breaks as the force drops instantaneously. The drawing force is stable at around 9 kN during the first 75 strokes. Thereafter, it starts rising and reaches 13 kN before the strip breaks. The sudden increase in the drawing force is an indicator of lubricant film breakdown. Accordingly, it is concluded that lubricant film breakdown of the tribo-system using Rhenus LA 722086 oil takes place after 75 strokes at a temperature of 100 °C (marked with dashed yellow lines in Figure 7.3a and Figure 7.3b).

7.2 Testing for further enhancements

The SRT experiments revealed that the tribo-system with Rhenus LA 72208 fails at high temperature, whereas the tribo-system runs acceptable in production when using similar tribological parameters. A careful analysis of both production and laboratory test conditions helps comprehending the differences in the test results. Table 7.1 summarises the differences between the production platform and the SRT.

One of the first clear differences is that in production, workpiece material is work-hardened before it goes through the ironing operation, while in SRT the material is provided directly from coil without undergoing a prior work-hardening. Despite this difference, during the thickness reduction, the normal pressures at both production and laboratory are in the same range. Although, from the point of view focussing on the pressure, the process was emulated successfully, the surface topography in production is different due to pre-forming operations which may affect the active lubrication mechanism. Another parameter affecting the Micro Plasto Hydro- lubrication mechanisms is the sliding speed. In production, the speed varies between 140-220 mm/s, whereas during SRT it is limited to 50 mm/s. As a result of suppressing the MPHDL via lower speed, the SRT may perform poorer than in production.

Another substantial difference is the thermal exchange time cycle. In production, the system is allowed to cool down when opening and closing the tooling. Furthermore, at each stroke a new sheet surface is transferred to the ironing station. In laboratory, although the initial temperature of the sheet was similar to that of production, no time was allowed for cooling down of the tooling. On the contrary, the temperature was kept above 140 °C through the entire SRT. Although the preheating temperature enables achieving the desired tool/workpiece interface temperature of the emulated ironing operation, the temperature does not drop during the idle time due to continuous contact in the entire tooling. In fact, the workpiece temperature increases as a result of the deformation- and friction-induced heating. Thus, the initial workpiece temperature after the first stroke was higher than 140 °C due to continuous sliding of the strip. Additionally, the flushing of the oil that clearly cools down the tool in production was not replicated in laboratory.

In order to study the effect of the sliding speed on the performance of the selected tribo-system, the experiment was run at three different drawing speeds: 50, 100 and 150 mm/s using Station A only. However, to reach

Table 7.1: Differences between the production and the laboratory platform.

Parameter	Laboratory	Production
Work hardening after forward stroke	Low ($\varepsilon_{max} < 0.35$)	High ($\varepsilon_{max} < 0.85$)
Surface topography	Original from coil	Deformed from previous steps
Contact length [mm]	Forward stroke: 1.5 Backward stroke: 0.5	Forward stroke: 2.5 Backward stroke: 1
Sliding speed [mm/s]	0-50	140-220
Lubrication	Through lubrication rolls	Flushing of the oil at high pressure
Thermal exchange	Tool/workpiece contact during idle time and homing operation	No tool/workpiece contact during idle time

desired sliding speeds within the capabilities of the tribotester, it was necessary to increase the sliding length. For a sliding speed of 50 mm/s, the sliding length was 10 mm, similar to what has been used until now. To reach a sliding speed of 100 mm/s, the sliding length was 12 mm. Lastly, the sliding length was increased to 20 mm to achieve a sliding speed of 150 mm/s.

Figure 7.4 shows the drawing force with respect to stroke number for various sliding speeds. All of the experiments start with a drawing force of 6 kN, similar to what was found in the numerical analysis given in Figure 6.2. For the experiment with a drawing speed of 50 mm/s, the force starts to rise at around 80 strokes, indicating lubricant film breakdown. In fact, it is very similar to the experiment with both Station A and B (see Figure 7.3a). This means that the lubricant film breakdown is already initiated at Station A. In the experiment with a drawing speed of 100 mm/s the force rises after 130 strokes, while in the experiment with a drawing speed of 150 mm/s the lubricant film breakdown occurred after 95 strokes. Accordingly, it is concluded that increasing the drawing speed has an influence on the onset of lubricant film breakdown, but not

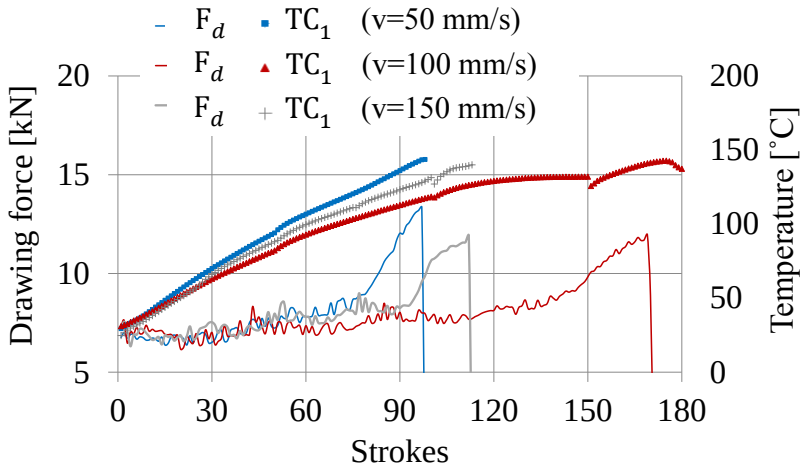

Figure 7.4: Measured drawing force as a function of strokes for the tribo-system using various sliding speeds.

enough to prevent it alone.

Another substantial difference listed in Table 7.1 is the thermal exchange between the die/workpiece and the tooling/environment. The impact of the temperature dissipation and thermal exchange on the lubricant film

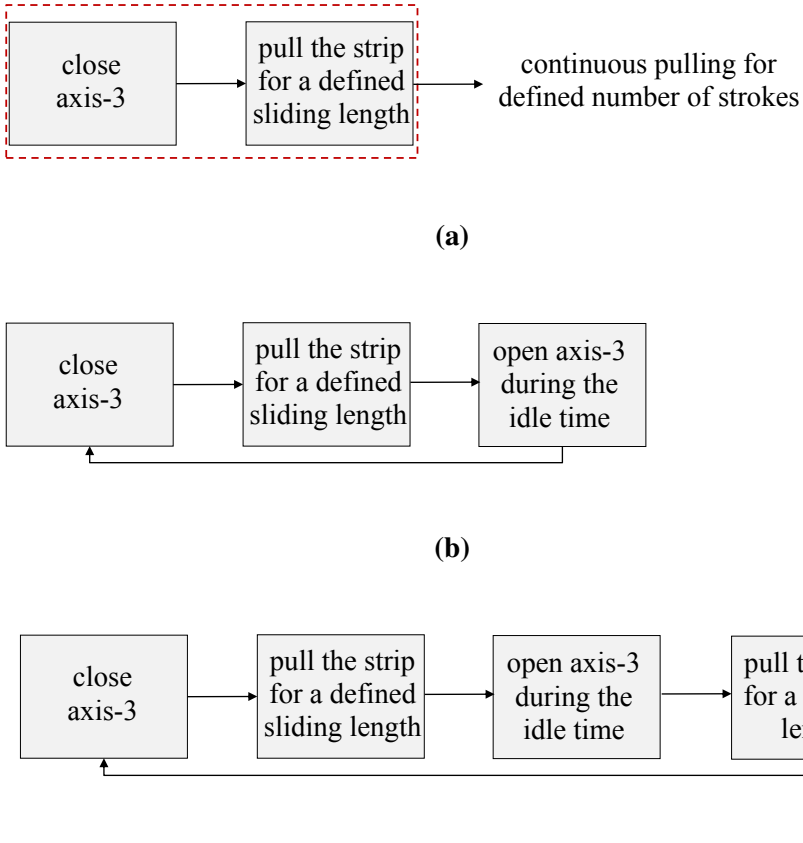

Figure 7.5: Process flow for a single stroke, illustrating (a) the original set-up, (b) Alternative-1 with released pressure of axis-3 during idle time and (c) Alternative-2 with released pressure of axis-3 and additional pulling (without thickness reduction) during idle time.

breakdown was studied in two alternative experimental set-ups. In these two proposed set-ups, the process chain was altered. Figure 7.5a shows a section of the entire process flow given in Figure 3.7. So far, the experiments were performed while keeping the axis-3 closed until the desired number of strokes was achieved. This is schematically illustrated in Figure 7.5a. The process chain of Alternative-1 is shown in Figure 7.5b. In the beginning of a stroke, first axis-3 is closed, then axis-1 pulls the strip with a defined sliding length and speed, similar to the original set-up. Hereafter, the pressure supplied by axis-3 is released during the idle time. In Alternative-2, an additional drawing of the strip with released pressure is performed (see Figure 7.5c). This means that during the idle time, the strip is drawn without thickness reduction. The length and the speed are input parameters and can be varied. In this experiment, the length with released pressure was set to 1 mm. The additional length was initially set to a short distance as the focus was to examine how the lubricant breakdown phenomenon would be affected by providing a new upcoming, fully lubricated strip surface for the following stroke.

The measured drawing forces with respect to the total number of strokes are given in Figure 7.6. In addition to Alternative-1 and -2, the result obtained by the initial process flow, i.e. with closed tooling throughout the entire process, is shown. Furthermore, the tribo-system that runs successfully with TDN 81 is given as a reference. All experiments were performed at an elevated temperature using both stations, except Alternative-2, for which Station B was eliminated due to non-reduced thickness sections (refer to the sketch of the strip given in Figure 7.6). Therefore, the reduction at Station A was set to 24 % for experiments with Alternative-2 process flow, whereas in the other experiments the strip thickness was reduced to 20 % at Station A and an additional 4 % of thickness reduction was applied at Station B.

The results show that in case of the process flow in Alternative-1, where the pressure of axis-3 is released without additional sliding, lubricant film breakdown has initiated almost at the same time as it did when keeping the tooling closed. Although releasing the pressure would lead to an additional heat convection with the air and a slight difference in the con-

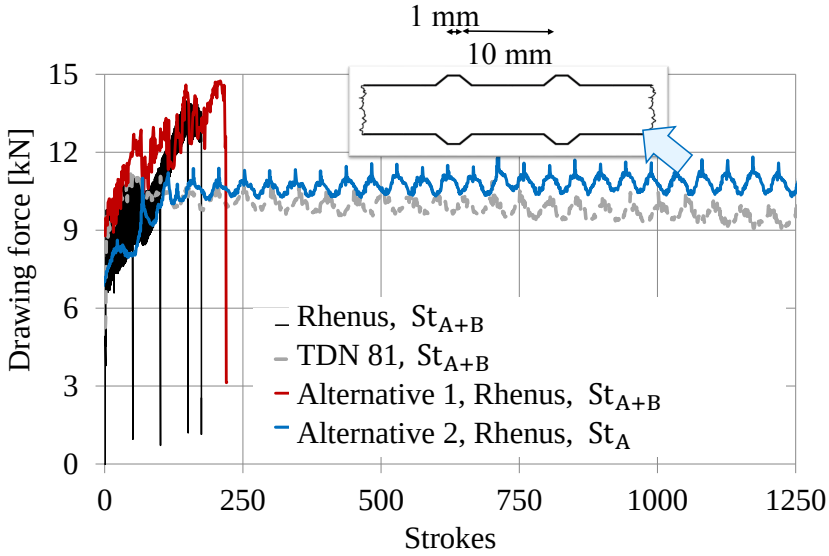

Figure 7.6: Measured drawing force as a function of strokes for the current and alternative process flows.

tact region of tool/workpiece interface, the upper tool pin preserves its contact with the sheet continuously. Therefore, the first alternative process flow did not improve the results. The second alternative was to slide the strip one additional millimetre without vertical pressure on the tool. The experimental results revealed that providing a new, well lubricated tool/workpiece contact surface for each stroke improves the performance of the tribo-system significantly as it could run more than 1000 strokes. A slight increase in the drawing force may be an indication of increasing severity of tribo-conditions.

For further examination, images from the lower tool surface at Station A were taken after 250 and 1250 strokes for the process flows in Alternative-1 and -2, respectively. In case of Alternative-1 together with the tool surface, Light Optical Microscopy (LOM) images taken from the strip surface after the thickness reduction indicate a heavy adhesive wear in the form of scoring along the strip surface (see Figure 7.7). LOM images taken after the experiment with the Alternative-2 process flow, on

the other hand, show a weaker form of abrasive wear. The strip surface is smooth with a few local scratches. In this case, the zone affected by the heat generation can be observed clearly. Finally, the results disclose that in spite of the indications towards the onset of lubricant film breakdown, the selected tribo-system with Alternative-2 runs acceptable for 1250 strokes.

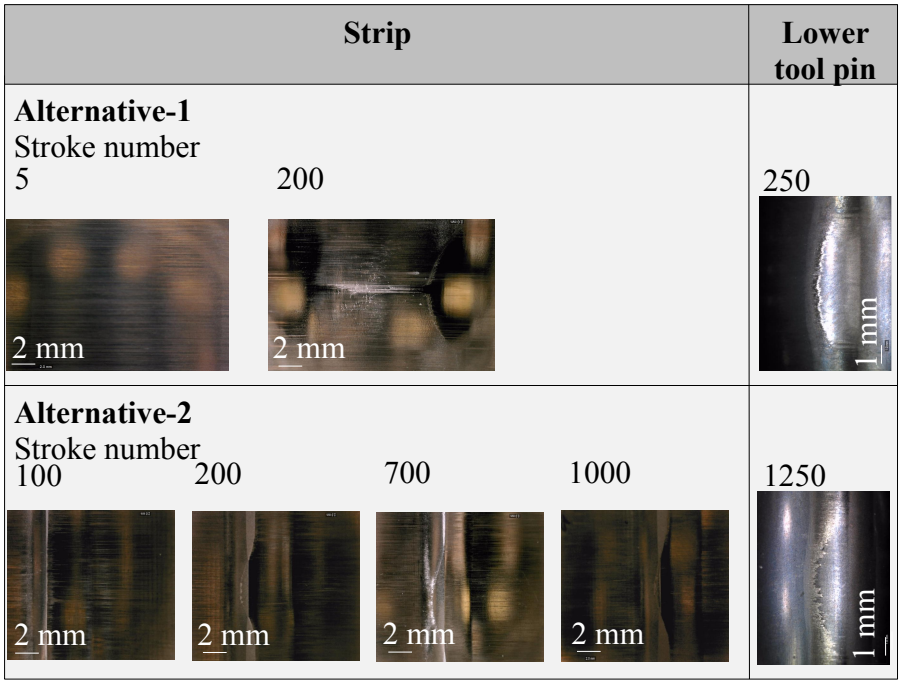

Figure 7.7: Light optical microscopy images of the lower tool pin and strip surfaces for the experiments with various process flows.

CHAPTER 8

Numerical Coupling of Metal and Liquid Flow

This chapter is dedicated to a new approach for combined modelling of plastic deformation and liquid lubrication in the contact interfaces between material and tooling in metal forming. A brief introduction including an overview of the state of the art, motivation and the objective of the study is followed by theoretical and numerical fundamentals of finite element formulations with deeper insight to the irreducible flow formulation. The fundamentals of plastic and fluid flow with a special emphasis on the flow formulation are given, and numerical implementation assuring strong coupling is presented. The proposed method is applied to simulate SRT. Applicability of the proposed fully-coupled approach is investigated and the results are discussed. The chapter ends with a summary, discussing the potential of the model and suggestions for future developments. The content of this chapter has been published elsewhere (Üstünyagiz et al. [137], [138], and [139]).

8.1 Introduction

While performing the off-line testing methodology, at the same time, it is vital to understand the lubrication mechanism of the production process. In most of the metal forming processes, the liquid lubrication regime is characterised by the mixed-film lubrication mechanism, where MPHDL and MPHSL are known to have a considerable influence on friction, wear and surface topography. At the same time, the active lubrication mechanism is influenced by a number of parameters. Complex influence of these parameters on lubrication must therefore be included by a fundamental numerical approach to predict the limits of lubrication.

The state of the art regarding the early studies of the influence of entrapped lubricant was given in Chapter1.2. In the last decades, there have not been significant advances in the modelling of contact with friction between workpiece and tools. The common practice is still to treat friction as a traction boundary condition with shear stresses along the interface between workpiece and tool and to assume shear stresses to follow either Coulomb's law or the law of constant friction stress. This means that a broad range of parameters, which are known to influence the frictional conditions in metal forming with liquid lubrication, such as surface expansion, sliding length, sliding speed, lubricant viscosity, and geometry and surface topography of tools and workpiece, are hidden in the tuning of friction and not directly taken into consideration.

This was recently recognised by Carretta et al. [140] who proposed a combination of computational fluid dynamics and solid mechanics to analyse Micro Plasto HydroDynamic effects in the numerical simulation of strip reduction. In their work, they identified numerical difficulties caused by the differences in stiffness of metals and fluids, which may be up to 9 or 10 orders of magnitude, and by excessive mesh distortion of the fluid. The latter was claimed to be solved by employing an Arbitrary Lagrangian-Eulerian (ALE) formulation in which the motion of the fluid mesh is uncoupled from the general motion of the workpiece mesh. In their most recent work [141], they have followed a two step

approach; simulation of macroscopic strip reduction with surface pockets and simulation of the microscopic liquid lubrication mechanism using the boundary conditions found in the first step. For the microscopic analysis, two thin layers of lubricant were modelled on both sides of the cavity. Opening of the main cavity at the front and back of the pocket was used as indications of MPHSL and MPHDL mechanisms. However, they reported a need for modelling a fictitious microscopic layer of lubricants and long simulation time, around 10 days.

Coupling of computational fluid dynamics and solid mechanics is generally not straightforward, because typical implementations of the Navier-Stokes equations work with velocities and pressures, whereas commonly utilised formulations of solid mechanics work with displacements. At the same time, the strong coupling of the liquid flow of lubricants and the plastic flow of metals has a vital importance in order to ensure that the rheological properties of the lubricant are also taken into consideration. Thus, there is room for improving the current state of the art in friction modelling by including the liquid flow in metal forming operations.

The objective of this chapter is to present a developed fully-coupled approach for modelling the interaction between plastic deformation and liquid lubrication and to apply it to the simulation of SRT.

8.2 Finite element formulation

In the finite element approach, the domain is discretised by a finite number of elements, where variables are interpolated by shape functions.

Depending on the governing equilibrium equation of the system, the finite element formulations can be either quasi-static or dynamic. An overview of the different types of formulations is given in Table 8.1.

The fundamentals of quasi-static and dynamic formulation are introduced in the following subsections. The presented introduction is based

Table 8.1: Finite element formulations and computer implementations applied to metal forming processes [142].

	Quasi-static formulations		
	Flow formulation	Solid formulation	Dynamic formulation
Equilibrium equation	Quasi-static	Quasi-static	Dynamic
Constitutive equation	Rigid-plastic/ viscoplastic	Elasto-plastic/ viscoplastic	Elasto-plastic/ viscoplastic
Main structure	Striffness matrix and force vector	Striffness matrix and force vector	Mass & damping matrices and internal-external force vectors
Minimisation of the residual force at each incremental step	Yes	Yes	No
Size of the incremental step	Medium	Medium to large	Very small
CPU time for incremental step	Medium	Medium to long	Very short
Time integration scheme[a]	Explicit	Implicit	Explicit
Accuracy of the results	Medium to high	High	Medium to low
Springback and residual stresses	No	Yes	Yes/No
Commercial FEM computer programs	Forge[b], Qform Deform[b], Eesy-2-Form	Abaqus (impl.), Autoform, Marc	Abaqus (expl.), Dyna3D, Pam-stamp

Notes: [a]In the sense that he algorithm does not need the values of the next time step to compute the solution; [b]also have solid formulation options.

on the work by Tekkaya and Martins [142]. A similiar outline is followed by Nielsen et al. [143]. More detailed descriptions of the FE formulation are addressed by Banabic [144], Zienkiewicz and Taylor [145] and Kobayashi et al. [146].

8.2.1 Quasi-static formulations

Quasi-static finite element schemes are based on quasi-static equilibrium equations. If the body forces are neglected, the equilibrium equation takes the following form:

$$\frac{\partial \sigma_{ij}}{\partial x_j} = 0 \tag{8.1}$$

where σ_{ij} is Cauchy stress tensor and x_j refers to Cartesian coordinates. Instead of satisfying point-wise partial differentiation of the equilibrium equation, it is satisfied in an average sense with an integral form in the entire volume domain V:

$$\int_V \frac{\partial \sigma_{ij}}{\partial x_j} \delta u_i dV = 0 \tag{8.2}$$

where δu_i is an arbitrary variation in velocity for rate-dependent applications or displacement for rate-independent cases.

Applying the dot rule of derivatives followed by the divergence theorem together with the essential and natural boundary conditions, Equation 8.2 takes the following form:

$$\int_V \sigma_{ij} \frac{\partial \delta u_i}{\partial x_j} dV - \int_{S_T} t_i \delta u_i dS = 0. \tag{8.3}$$

$t_i = \sigma_{ij} n_j$ represents the tractions applied on the boundary surface S_T in the direction of the unit normal vector n_j. Equation 8.3 is also known as the weak form of the equilibrium equation, Equation 8.1, as it is satisfied only in weaker continuity requirements.

At the instant of time t, the following set of equations, written in matrix form, can be built from Equation 8.3:

$$\mathbf{K}^t \mathbf{u}^t = \mathbf{F}^t \tag{8.4}$$

where **K** and **F** are the stiffness matrix and the load vector applied on the boundary, respectively.

The quasi-static finite element formulation used in metal forming processes utilises mostly an implicit time integration. The equilibrium conditions are checked at each increment of time in order to minimise the residual vector **R**, which is computed as follows for iteration number i:

$$\mathbf{R}_i^t = \mathbf{K}_{i-1}^t \mathbf{u}_i^t - \mathbf{F}^t. \tag{8.5}$$

The set of equations in Equation 8.4 is non-linear due to dependency of the **K** on the primary unknown, **u**. The non-linear set of equations can be solved by direct iteration, which evaluates the stiffness matrix for the displacement from the previous iteration. In that way the system (Equation 8.4) is reduced to a linear set of equations. The method converges in the beginning, but slows down when approaching the solution. Another solution technique is the Newton-Raphson method, which is based on linear expansion of the residual force vector **R** near the velocity estimate at the previous iteration (see Equation 8.6 and Equation 8.7). Although the Newton-Raphson method converges faster, it requires an initial guess of the velocity field close to the solution.

$$\mathbf{R}_i^t = \mathbf{R}_{i-1}^t + \left(\frac{\partial \mathbf{R}}{\partial \mathbf{u}} \right)_{i-1}^t \Delta \mathbf{u}_i^t = \mathbf{0} \tag{8.6}$$

$$\mathbf{u}_i^t = \mathbf{u}_{i-1}^t + \Delta\mathbf{u}_i^t \tag{8.7}$$

In an implicit finite element scheme, the solution of a linear system of equations is required for each iteration, which uses large memory and a high CPU. On the other hand, the advantage of an implicit solution is that it is unconditionally stable, it does not have to satisfy a stability condition, and equilibrium is enforced under user-defined tolerances.

8.2.2 Dynamic formulation

A dynamic finite element formulation is based on a dynamic equilibrium equation in the following form:

$$\frac{\partial \sigma_{ij}}{\partial x_j} - \rho \ddot{u}_i = 0 \tag{8.8}$$

where ρ stands for the density and $\ddot{u}$ is the acceleration. Applying a similar mathematical procedure to that of the previous subsection, the weak variational form of the dynamic equilibrium equation can be expressed as follows:

$$\int_V \rho \ddot{u}_i \delta u_i dV + \int_V \sigma_{ij} \frac{\partial(\delta u_i)}{\partial x_j} dV - \int_{S_T} t_i \delta u_i dS = 0 \tag{8.9}$$

and the general matrix form at the instant of time t can be written as:

$$\mathbf{M}^t \ddot{\mathbf{u}}^t + \mathbf{F}_{int}^t = \mathbf{F}^t. \tag{8.10}$$

$\mathbf{M}$ stands for mass matrix, $\mathbf{F}_{int} = \mathbf{Ku}$ is the vector of internal forces in connection with system stiffness and $\mathbf{F}$ is the force vector.

The non-linear set of equations is commonly solved by an explicit central difference time integration scheme, as such:

$$\mathbf{M}^t \left(\frac{\dot{\mathbf{u}}^{\frac{t+1}{2}} - \dot{\mathbf{u}}^{\frac{t-1}{2}}}{\Delta t^{\frac{t+1}{2}}} \right) + \mathbf{F}_{int}^t = \mathbf{F}^t, \tag{8.11}$$

$$\dot{\mathbf{u}}^{\frac{t+1}{2}} = \left(\mathbf{M}^t\right)^{-1} \left(\mathbf{F}^t - \mathbf{F}_{int}^t\right) \Delta t^{\frac{t+1}{2}} + \dot{\mathbf{u}}^{\frac{t-1}{2}}, \tag{8.12}$$

$$\mathbf{u}^{t+1} = \mathbf{u}^t + \dot{\mathbf{u}}^{\frac{t+1}{2}} \Delta t^{t+1}. \tag{8.13}$$

In the explicit time scheme, the calculations are performed in an incremental procedure, but the time increment Δt must be:

$$\Delta t \leqslant \frac{L_e}{c} \tag{8.14}$$

where L_e is the characteristic element length and c is the speed of sound.

At the end of each increment, the stiffness matrix is updated based on the displacement. Then, a new stiffness matrix is constructed and the next increment of displacement is applied to the system. In this type of analysis, the increments should be small enough to obtain accurate results, which may require long calculation time. Another drawback of this method is that it is only conditionally stable and the equilibrium after each increment of time is not checked.

8.3 Flow formulation

8.3.1 Plastic flow

The weak form of quasi-static equilibrium was described by Equation 8.3 and can also be obtained from the first order variation of the total potential energy rate. In the flow formulation, the unknowns are velocities instead of displacements, there is no strain tensor and stress is related to the strain rate tensor by means of constitutive equations. The velocity field is determined from the first order variation of the total potential energy. For minimum potential energy, Equation 8.3 takes the following form:

$$\delta\Pi = \int_V \overline{\sigma}\delta\dot{\overline{\varepsilon}}dV - \int_{S_T} t_i\delta u_i dS = 0. \tag{8.15}$$

The entire domain is subjected to the incompressibility condition:

$$\dot{\varepsilon}_v = 0 \quad in \quad V. \tag{8.16}$$

The most common methods to apply the incompressibility constraint involve the utilisation of Lagrange multipliers or penalty functions. The formulation of this study makes use of the penalty-based approach. After implementing the incompressibility constraint, the first order variation of the weak form of the equilibrium equation becomes:

$$\delta\Pi = \int_V \overline{\sigma}\delta\dot{\overline{\varepsilon}}dV + K\int_V \dot{\varepsilon}_v\delta\dot{\varepsilon}_v dV - \int_{S_T} t_i\delta u_i dS = 0 \tag{8.17}$$

where K is a large positive number that enforces incompressibility. However, this number cannot be too large because it may lead to ill-conditioning and locking of the system of equations.

8.3.2 Fluid flow

For any fluid satisfying the continuum assumption, the differential equation of linear momentum resulting from force equilibrium in a fluid particle can be expressed by

$$\frac{\partial \sigma'_{ij}}{\partial x_j} - \frac{\partial p}{\partial x_i} + \rho g_i = \rho \left(\frac{du_i}{dt} + u_j \frac{\partial u_i}{\partial x_j} \right). \tag{8.18}$$

The left-hand side of equation Eq. 8.18 is related to viscous forces, pressure and body forces. The symbol p denotes the hydrostatic pressure and σ'_{ij} represents the deviatoric (viscous) stresses, which are related to the total stresses σ_{ij} as follows, $\sigma_{ij} = \sigma'_{ij} + p$. The symbols ρ and g_i designate density and gravity acceleration, respectively.

The right-hand side of Equation 8.18 is related to inertia effects. If convective terms are neglected, due to the small space-dependency, this term reduces to the following:

$$\rho \frac{du_i}{dt} = \rho a_i \tag{8.19}$$

where a_i is the acceleration. Because deviatoric (viscous) stresses σ'_{ij} in fluids are proportional to strain rates $\dot{\varepsilon}_{ij}$:

$$\sigma'_{ij} = 2\mu_s \dot{\varepsilon}_{ij}, \tag{8.20}$$

by substituting Equation 8.19 and Equation 8.20 into Equation 8.18, the differential equation of the linear momentum for an incompressible fluid flow with constant viscosity reduces to the Navier-Stokes equation:

$$\mu_s \frac{\partial^2 u_i}{\partial x_j^2} - \frac{\partial p}{\partial x_i} + \rho g_i = \rho \frac{du_i}{dt}. \tag{8.21}$$

μ_s is the shear viscosity, which takes constant values $\mu_s = \mu_{s,0}$ for Newtonian fluids and strain rate dependent values $\mu_s = \mu_s(\dot{\varepsilon}_{ij})$ for non-Newtonian fluids (e.g., metals).

If the elastic response of metals as well as the inertia effects are neglected, the above-given expression becomes identical to the flow formulation. The basis for coupling the plastic flow of metals and the incompressible laminar flow of viscous fluids lies in the fact that the flow formulation treats metals as rigid-plastic (or rigid-viscoplastic) materials that fulfil the incompressibility condition $\dot{\varepsilon}_{ii} = 0$.

The governing form of the irreducible finite element flow formulation (also known as the direct penalty form of the finite element flow formulation) is derived from the discretisation of the weak form of Equation 8.21 by means of finite elements, as follows:

$$\int_V \sigma'_{ij}\delta\dot{\varepsilon}'_{ij}dV + K\int_V \dot{\varepsilon}_{ii}\delta\dot{\varepsilon}_{ii}dV - \int_{S_T} t_i\delta u_i dS + \int_V \rho g_i \delta u_i dv = 0. \tag{8.22}$$

As seen in Equation 8.22, the separation between deviatoric (viscous) and volumetric terms is similar to Equation 8.17. Therefore, the formulations enable a direct correlation of shear and bulk viscosity for metals and fluids undergoing laminar flow. For example, the deviatoric stresses of metals may be seen as the stress response of non-Newtonian fluids of very high viscosity $\mu_s = \overline{\sigma}/3\dot{\overline{\varepsilon}}$ (in close analogy to Equation 8.20) when comparing with the Levy-Mises constitutive equation:

$$\sigma'_{ij} = \frac{2}{3}\frac{\overline{\sigma}}{\dot{\overline{\varepsilon}}}\dot{\varepsilon}'_{ij}. \tag{8.23}$$

Conversely, the penalty factor K, utilised to ensure the incompressibility of metals, may be seen as the bulk viscosity μ_v of fluids relating the changes $\dot{\varepsilon}_{ii}$ in volume V with the hydrostatic pressure p (or average stress

σ_m):

$$K = \mu_v \quad with \quad \sigma_m = -p = K\dot{\varepsilon}_{ii}. \tag{8.24}$$

8.4 Numerical implementation

As a result of the equations given in previous section, it may be concluded that the velocity-pressure ($u - p$) characteristics of the flow formulation leads to a natural coupling between metals and fluids, in which metals are treated as incompressible fluids with a very high viscosity (see Equation 8.22). Thus, one of the main challenges in coupling of conventional finite element software used in fluid dynamics and solid mechanics can be straightforwardly solved by means of the new, proposed approach based on the flow formulation due to its capability of solving velocities u_i and hydrostatic pressures p simultaneously.

The discretisation of the weak form given in Equation 8.22 by means of M elements results in sets of non-linear equations and is described by

$$\sum_{m=1}^{M} \left\{ \int_{V^m} \delta \mathbf{v}^T \mathbf{K} \mathbf{v} dV^m + K^m \int_{V^m} \delta \mathbf{v}^T \mathbf{C}^T \mathbf{B} \mathbf{v} \mathbf{C}^T \mathbf{B} dV^m - \int_{S_T{}^m} \delta \mathbf{v}^T \mathbf{C}^T \mathbf{N} \mathbf{T} dS^m \right\} = 0 \tag{8.25}$$

where **v** is the vector of nodal velocities, **N** is the shape function matrix and **T** boundary surface traction matrix. **K** is the stiffness matrix and given by

$$\mathbf{K} = \mathbf{B}^T \mathbf{D}_\mu \mathbf{B} \tag{8.26}$$

where **B** is the strain rate matrix and described as follows:

$$\mathbf{B} = \mathbf{L}\mathbf{N}^T, \quad \mathbf{L} = \begin{bmatrix} \delta/\delta x & 0 & 0 \\ 0 & \delta/\delta y & 0 \\ 0 & 0 & \delta/\delta z \\ \delta/\delta y & \delta/\delta x & 0 \\ 0 & \delta/\delta z & \delta/\delta y \\ \delta/\delta z & 0 & \delta/\delta x \end{bmatrix}. \tag{8.27}$$

In Equation 8.25, **C** is the vectorial form of Kronocker delta δ_{ij}:

$$\mathbf{C}^T = \begin{bmatrix} 1 & 1 & 1 & 0 & 0 & 0 \end{bmatrix}. \tag{8.28}$$

The proposed approach was implemented in the existing flow formulation-based finite element computer programme, I-form. The implementation was carried out mainly by replacing the diagonal matrix **D**, built upon the Levy-Mises constitutive equations, by the following $\mathbf{D}_\mu$ matrix resulting from Equation 8.20:

$$\mathbf{D} = \frac{\bar{\sigma}}{\dot{\bar{\varepsilon}}} \begin{bmatrix} 2/3 & 0 & 0 & 0 & 0 & 0 \\ 0 & 2/3 & 0 & 0 & 0 & 0 \\ 0 & 0 & 2/3 & 0 & 0 & 0 \\ 0 & 0 & 0 & 1/3 & 0 & 0 \\ 0 & 0 & 0 & 0 & 1/3 & 0 \\ 0 & 0 & 0 & 0 & 0 & 1/3 \end{bmatrix}, \tag{8.29}$$

$$\mathbf{D}_\mu = \mu_s \begin{bmatrix} 2 & 0 & 0 & 0 & 0 & 0 \\ 0 & 2 & 0 & 0 & 0 & 0 \\ 0 & 0 & 2 & 0 & 0 & 0 \\ 0 & 0 & 0 & 1 & 0 & 0 \\ 0 & 0 & 0 & 0 & 1 & 0 \\ 0 & 0 & 0 & 0 & 0 & 1 \end{bmatrix}.$$

As a result of this, the stiffness matrix of the interface layer of the fluid elements that are utilised to discretise the lubricants is calculated from $\mathbf{K}_\mu = \mathbf{B}^T \mathbf{D}_\mu \mathbf{B}$, where $\mathbf{B}$ is the classical strain rate matrix.

8.5 Verification of applicability

As with all new numerical developments, it is necessary to investigate its accuracy, reliability and validity. This was carried out by assessing numerical predictions by experiments on the escape of entrapped lubricants.

8.5.1 Experimental work

The phenomenon of lubricant escape and a description of the experimental approach were previously given in Chapter 1.1.2. The experimental results used in this project were obtained from an earlier study

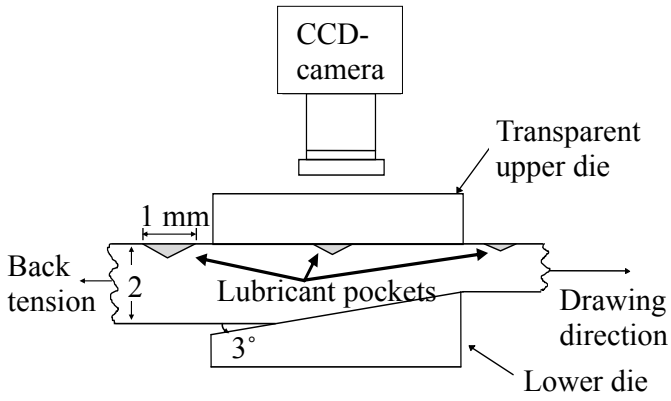

Figure 8.1: Schematical representation of experimental set-up used for the investigations into escape of lubricants from the surface pockets.

[35]. An aluminium AA5052 strip of 2 mm thickness was drawn through a wedge-shaped die with a die angle of 3° and reduced in thickness by 20 %. The upper side of the strip was provided with pyramidal-shaped pockets, with 1x1 mm base lengths and 10° slopes, which were filled with lubricant prior to drawing. A transparent, hardened glass die allowed observation of the lubrication mechanisms on the strip directly (see Figure 8.1). In this way the influence of friction, back tension, lubricant viscosity and drawing speed on forward (MPHSL) and backward (MPHDL) lubricant escape were studied.

The simulation conditions utilised to validate the new, proposed approach for modelling plastic deformation and liquid lubrication are given

coeff. of friction μ	back tension σ_{bt}	lubricant viscosity $\mu_{S,0}$	drawing speed v
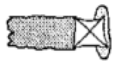 **0.025**	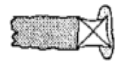 **0** MPa	 0.005 Pa·s	 0.2 mm/s
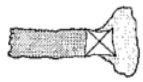 0.05	 62 MPa	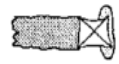 **0.15** Pa·s	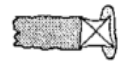 **0.5** mm/s
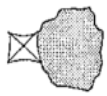 0.28	 105 MPa	 0.76 Pa·s	 5 mm/s

Figure 8.2: Illustration of experimental results on escape of lubricant from the surface pockets for various parameters [35].

in Figure 8.2. The values in underline bold were taken as references while the others are variants of a particular parameter keeping all the others at their reference values. As shown in the schematical drawings included in Figure 8.2, the increase in lower die friction and back tension lead to a shift from backward towards forward lubricant escape, whereas the increase in viscosity or velocity causes an opposite effect.

8.5.2 Numerical modelling

The stress-strain curve of the AA5052 strip was approximated by the following Ludwik-Hollomon equation [35]:

$$\overline{\sigma} = 321\overline{\varepsilon}^{0.08} \quad [MPa]. \tag{8.30}$$

The main process parameters utilised in numerical modelling were taken from literature [35] in order to match the experimental conditions. Additional assumptions used in this study were (i) sticking friction conditions along the contact interfaces between the strip and the lubricant in order to replicate the absence of relative velocity, (ii) a constant friction factor of $m = 0.3$ along the contact of the strip with the upper die made from hardened glass and (iii) a bulk viscosity of the lubricant of $\mu_v = 1500$ MPa·s [137].

The plastic deformation of the strip was modelled in 2D under plane strain deformation, which means that the pyramidal pockets were considered as infinitely long grooves in the sheet perpendicular to the drawing direction. It should be kept in mind for the following sections that replacing the pyramidal pockets by infinitely long grooves may promote deformation of the pocket due to reduced stiffness. This may lead to an increase of the hydrodynamic pressure and hence affect the lubricant escape.

The sheet and lubricant were discretised by means of linear quadrilateral

elements, whereas the dies were treated as rigid objects and discretised by means of linear contact-friction elements (see Figure 8.3a). The large difference in stiffness between metals and lubricants commonly gives

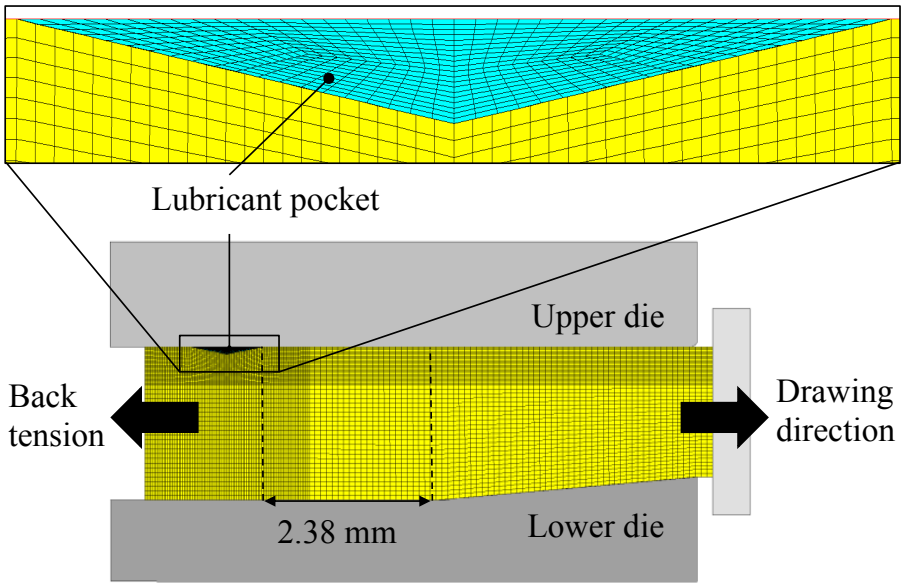

(a)

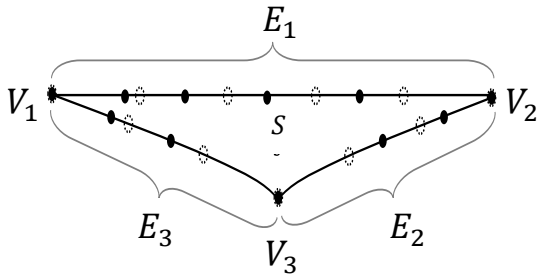

(b)

Figure 8.3: (a) Finite element model of strip reduction with a detail of the pocket on the strip surface and (b) schematical representation of smoothing for the pocket geometry.

rise to unacceptable mesh distortion inside the pockets as soon as the strip material starts to be drawn. Because this problem leads to numerical difficulties, a continuous smoothing algorithm was developed. The algorithm can be easily and effectively applied to the lubricant mesh without influencing the quality of the results due to the history independence of its constitutive equations (refer to Equation 8.20). The smoothing algorithm is based on fixing the vertices V_1, V_2 and V_3 identified in Figure 8.3b by the boundary nodes where the neighbouring edge segments have a mutual angle greater than a critical angle. The overall quality of the mesh is improved by smoothing all other nodes. First, the edges E_1, E_2 and E_3 between vertices are defined. A parametric-based procedure is utilised for the edge smoothing. The present algorithm is improved by handling the smoothing in one step by uniform distribution of the edge nodes along the (in general curved) edges. The full points in Figure 8.3b represent the position of nodes lying on the edge before smoothing, whereas the dotted circles illustrate the nodal positions after smoothing. Finally, the surface S is smoothened by Laplacian surface smoothing.

A typical simulation consisting of a mesh with approximately 9300 nodal points and 9100 elements, similar to that shown in Figure 8.3a, required approximately 4 hours to be finished in a laptop computer equipped with an Intel CPU e5-1660 (3.0 GHz) processor. The convergence norm for the velocity field $|\Delta u|/|u|$ was chosen as 0.001.

8.5.3 Results and discussion

MPHSL - Friction along the lower die

The influence of friction along the lower die on the forward lubricant escape was analysed by performing numerical simulations with various friction factors along the contact interface between the inclined lower die and the strip material. The simulations were performed without back tension, a constant lubricant viscosity of $\mu_{s,0} = 0.15$ Pa·s and a drawing

speed of $v = 0.2$ mm/s in order to replicate the experimental conditions (refer to Figure 8.2).

Figure 8.4 shows the build-up of liquid pressure p_{liq} and sealing pressure p_f at the pocket front as a function of the strip displacement during the drawing process. In the numerical model, the pocket is initially placed 2.38 mm away from the entrance of the reduction zone as shown in Figure 8.3a. Figure 8.4 presents pressures after a 2.8 mm strip displacement, where the pocket has entered the reduction zone, so that the liquid pressure build-up has started. For the experimental work, Coulomb's friction model was used. Although the experimental study was based on Coulomb's friction law, due to high normal pressure characteristics of the strip reduction process, the constant friction law was selected for numerical modelling. Two different values of the friction factor were chosen in order to model frictionless ($m = 0$) and typical ($m = 0.3$) conditions of drawing.

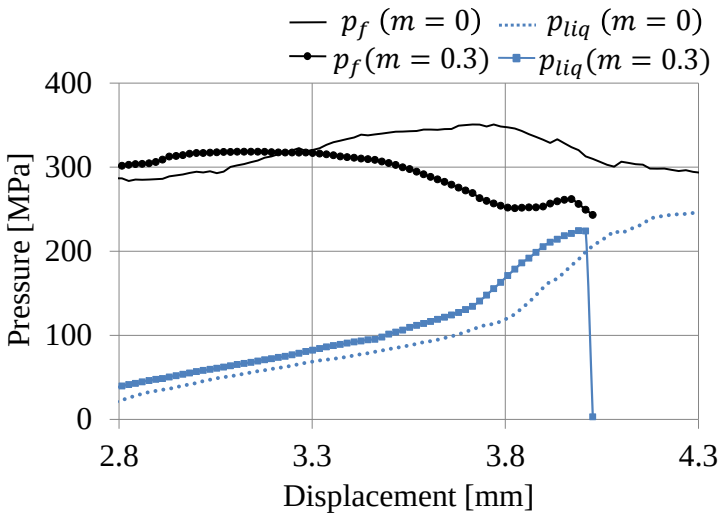

Figure 8.4: Evolution of the liquid lubricant pressure p_{liq} and the front sealing pressure p_f of the pocket with respect to displacement for two friction factors m along the inclined lower die.

As seen in Figure 8.4, the liquid pressure p_{liq} increases as the pocket is drawn through the inclined plastic deformation zone. The forward sealing pressure p_f remains above 200 MPa due to previous plastic deformation of the strip material but its overall value depends on the friction along the lower die.

For example, in case of $m = 0$, the pressure p_{liq} builds up to 250 MPa without reaching the sealing pressure p_f, which remains approximately equal to 300 MPa. This means that frictionless conditions in the lower die do not promote forward escape of lubricant, as it was experimentally observed by Bech et al. [35] (refer to Figure 8.2).

In contrast, the finite element predictions for $m = 0.3$ suggest forward escape of the lubricant because the build-up of pressure p_{liq} reaches the sealing pressure p_f, which is lower in this case than for $m = 0$. The simulated results with the increased friction factor m show the same tendency as the experimental results provided in Figure 8.2.

Although the finite element model does not replicate the outflow of lubricant from the pocket, the drop of pressure p_{liq} in the numerical model can also be explained by an instantaneous change in volume. In fact, once the pressure p_{liq} inside the pocket overtakes the adjacent sealing pressure p_f, there is a sudden increase in the volume of the pocket that justifies the aforementioned drop of pressure p_{liq} from a numerical point of view. This phenomenon is not reported in the literature as the focus is commonly placed on the escape of lubricant from the pocket and an associated drop in pressure p_{liq}.

Figure 8.5 shows the finite element predicted onset of lubricant escape for different friction factors m. As seen, the onset of lubricant escape occurs earlier with increasing friction on the lower die, in close agreement with the parameter study performed by Bech et al. [35], which shows that an increase in friction promotes the forward escape while limiting the backward escape (see Figure 8.2). However, this agreement can only be seen as qualitative due to the different shapes of the actual geometry and the finite element model of the pocket (pyramidal versus infinite long groove).

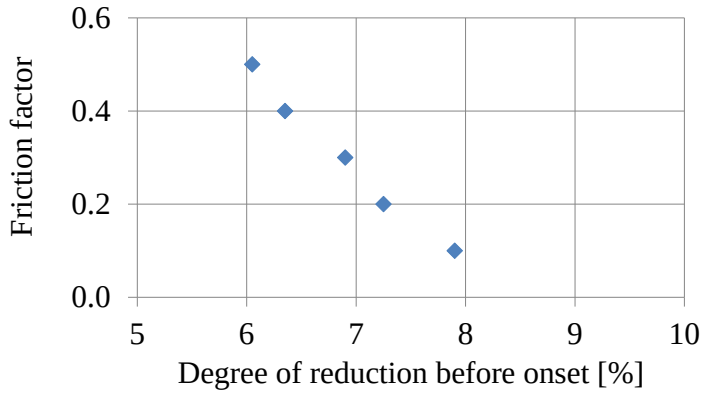

Figure 8.5: Dependency of the onset of lubricant escape on the friction factor at the inclined lower die.

MPHSL - Back tension

The influence of back tension on the forward lubricant escape was analysed by performing numerical simulations with various back tension, σ_{bt}, values applied in the leftmost end of the strip material (see Figure 8.3a). The simulations were performed with three different values of back tension: $\sigma_{bt} = 0$, 30, 62 MPa, and a constant friction along the lower die $m = 0$, a lubricant viscosity of $\mu_{s,0} = 0.15$ Pa·s and a drawing speed of $v = 0.5$ mm/s.

Figure 8.6 shows that an increase in back tension will lead to a significant decrease in the sealing pressure p_f. The liquid pressure p_{liq} is also found to decrease, but not to the same extent, which implies an increasing tendency to forward lubricant escape, as it was experimentally observed (see Figure 8.2).

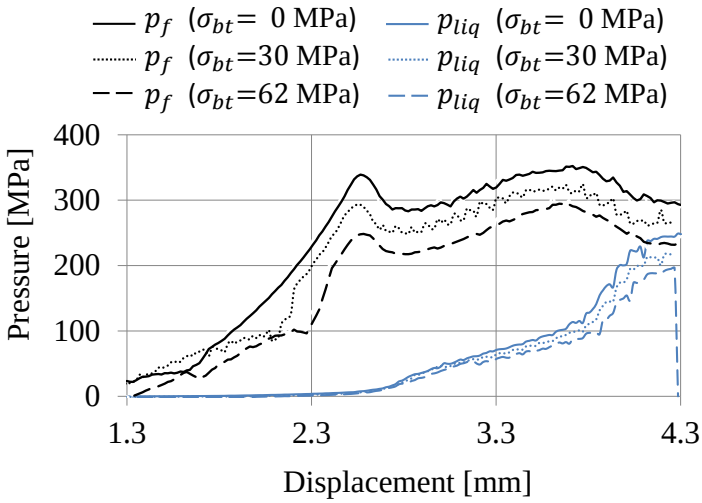

Figure 8.6: Evolution of liquid pressure p_{liq} and the front sealing pressure p_f of the pocket with respect to displacement for various back tension σ_{bt} values.

MPHDL - Shear Viscosity

The influence of pressure dependent shear viscosity μ_s is

$$\mu_s = \mu_{s,0} exp\left(\beta p_{liq}\right). \tag{8.31}$$

The simulations were performed with three different values of shear viscosity: $\mu_{s,0} = 0.005$, 0.76, 1.5 Pa·s and a pressure-viscosity coefficient of $\beta = 2.1\text{x}10^{-8}$ Pa^{-1}. A constant friction along the lower die $m = 0$, a back tension value of $\sigma_{bt} = 0$ MPa and a drawing speed of $v = 0.5$ mm/s were chosen from the experimental conditions summarised in Figure 8.2.

The numerical simulation of the lubricant escape caused by the local increase of p_{liq} at the rear end of the pocket was unsuccessful due to limited finite element discretisation and unacceptable distortion of the lubricant mesh. It is worth noting that this localised mesh distortion should not be

confused with the global mesh distortion of the overall lubricant mesh (pocket) that is effectively solved by the previously mentioned smoothing algorithm.

To overcome the above-mentioned difficulty, it was decided to combine the finite element simulation with an analytical model of the increase in liquid pressure p_{liq} at the rear end of the pocket based on the Reynolds equation:

$$\frac{dp_{liq}}{dx} = 6\mu_s v \frac{h - h_m}{h^3} \tag{8.32}$$

where h is the local film thickness, h_m is the film thickness in the plateau, μ_s is the pressure dependent viscosity, v is the sliding velocity between tool and liquid and p is the liquid pressure.

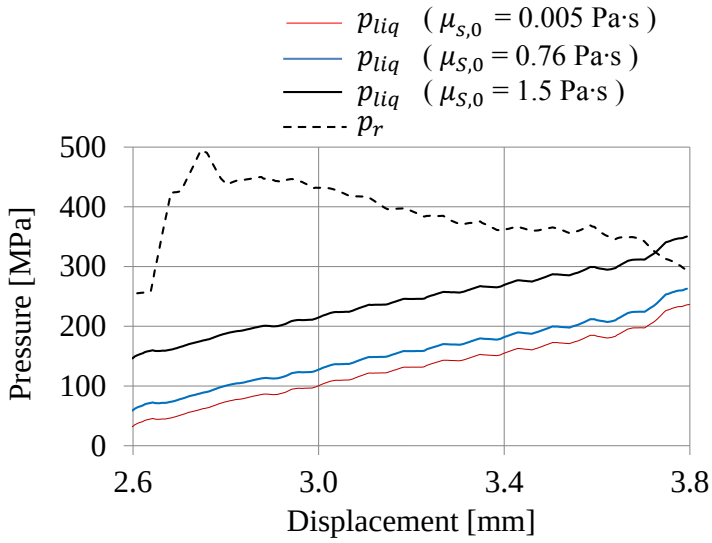

Figure 8.7: Evaluation of the liquid pressure p_{liq} and the rear sealing pressure p_r of the pocket with respect to displacement for various shear viscosity $\mu_{s,0}$ values.

Considering a pocket edge with a radius of curvature of $R = 80$ μm and a film thickness of $h_m = 0.1$ μm on top of the asperities [35], the local increase of the liquid pressure Δp_{liq} for two different shear viscosities, $\mu_{s,0} = 0.76$ Pa·s and $\mu_{s,0} = 1.5$ Pa·s, is equal to 26.9 MPa and 114.3 MPa, respectively. Now, because the required amount of Δp_{liq} for allowing the lubricant to escape had been previously estimated as 32 MPa [35], it may be concluded that for viscosities larger than $\mu_{s,0} = 0.76$ Pa·s, backward escape is likely to happen. If the viscosity is raised further, the tendency for the lubricant to escape shifts to the earlier stages of the reduction (see Figure 8.7), in accordance with the experimental results of Figure 8.2.

MPHDL - Drawing speed

The influence of the drawing speed on the backward lubricant escape was analysed by performing numerical simulations with three different drawing speeds: $v = 0.2$, 0.5, 5 mm/s. A constant friction along the lower die $m = 0$, a lubricant viscosity of $\mu_{s,0} = 0.15$ Pa·s and a back tension value of $\sigma_{bt} = 0$ MPa were chosen in accordance with Figure 8.2.

Figure 8.8a shows that the liquid pressure p_{liq} increases with the drawing speed v, while the rear sealing pressure p_r has an opposite trend. This allows the two curves to intersect for drawing speeds of $v = 0.5$ and 5.0 mm/s in accordance with the experiments. In fact, the increase in drawing speed follows similar trends as the increase in shear viscosity because both situations raise the stress response of the lubricant.

Figure 8.8b illustrates the hydrostatic pressure in the lubricant and vertical stress distribution in the strip just before the backward escape occurs for a drawing speed of $v = 5$ mm/s, which is marked with a circle in Figure 8.8a. The forward sealing pressure is high enough to restrict forward escape, whereas the backward sealing pressure is very close to the hydrostatic pressure in the lubricant.

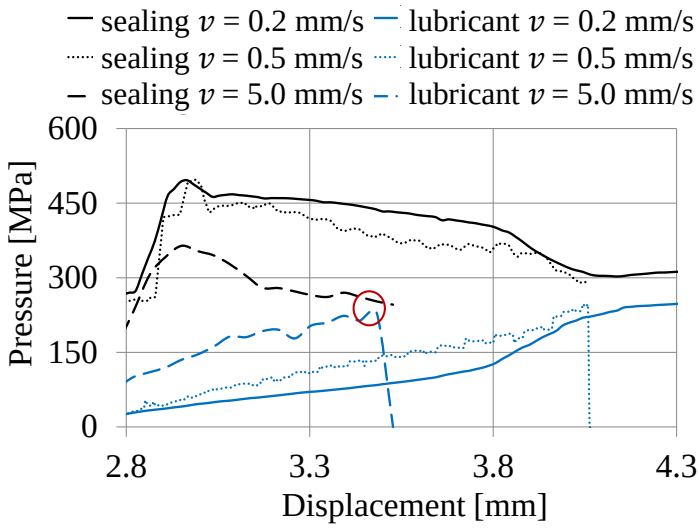

(a)

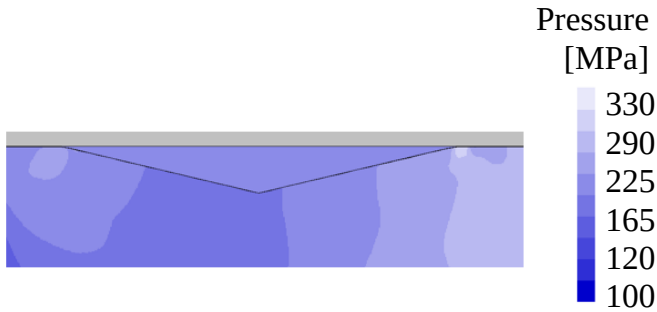

(b)

Figure 8.8: (a) Evolution of the liquid pressure p_{liq} and rear sealing pressure p_r of the pocket with displacement for different drawing speeds and (b) distribution of the vertical stress within the pocket and its surroundings just before the onset of escape corresponding to the location marked by the red circle in (a).

8.6 Conclusion

The finite element flow formulation can be utilised to simultaneously solve the plastic deformation of metals and the viscous flow of liquid lubricants. The required modifications to implement such a fully-coupled approach in existing computer programmes are simple and mainly consist of replacing the stress-strain matrix built upon the constitutive equations of metals by the viscous, nearly incompressible equations of Newtonian fluids. The velocity-pressure nature of the flow formulation ensures the required strong coupling and the numerical difficulties caused by the heavy mesh distortions due to large differences between the stiffness of metals and liquids can be solved by an appropriate smoothing algorithm.

The new, proposed approach was successfully applied to the drawing of a strip with a lubricant pocket in order to investigate the MPHSL and MPHDL mechanisms. Varying the process parameters, both MPHSL and MPHDL mechanisms were investigated. The overall trends were characterised, and results compare well with experimental data and observations published by Bech et al. [35]. Current limitations in the computer implementation of the proposed fully-coupled approach, however, impedes simulation of the physical escape of the lubricant.

CHAPTER 9

Conclusions and Future Work

Testing of new tribo-systems in production is costly. Adapting the off-line methodology in laboratory, on the other hand, avoids the use of production tools for testing, and the costs that may be incurred due to tool breakage and stops in production. Additionally, off-line testing gives the flexibility of examining many different tribo-systems and production lines once the methodology has been established. One of the most critical aspects of this methodology is that the laboratory testing of tribo-systems for the selected sheet metal forming application must ensure similar conditions with the tribo-parameters that are utilised in real production in order to generate data which are meaningful for industry. Thus, an accurate reproduction of the sheet metal forming operations by means of physical simulation requires a careful design and continuous communication with industrial partners.

In the present work, a methodology for off-line evaluation of new tribo-systems in industrial ironing operations has been developed. One of the innovative key points is to use the Universal Sheet Tribotester (UST2)

which can perform multiple strokes, providing the possibility of emulating an industrial production. The off-line methodology was applied to the industrial case of Grundfos A/S, where the environmentally benign Rhenus oil can run for a limited number of strokes. The selected production process concerns the manufacturing of a stainless steel cup, which is used in water pumps as a bearing plate. The plate is manufactured in a progressive tool consisting of 13 stages. The critical final step is a combined collar drawing and ironing, where the severe rheological conditions result in lubricant film breakdown.

To replicate the severe tribological conditions in industrial ironing processes, a Strip Reduction Test (SRT) set-up has been designed. The innovative step of the design is to replicate both the forward stroke and the backward retraction of the punch by means of a two-stage tool design. The main parameters to consider were the tool and workpiece materials, surface roughnesses, sliding length, sliding speed, interface temperature, interface pressure and lubrication.

Preliminary tests have shown promising results regarding the identification of lubricant film breakdown with the new SRT tool design. Reproducibility of the results was tested and the influence of Station B was examined. Similar to what occurs during production, lubricant film breakdown takes place during the emulated backward stroke in Station B. The initial experiments were run with and without AlCrN coating and with various test rates to emphasise the importance of these factors on the tool life while testing the capabilities of the tool set-up.

The next step was to analyse the production platform and identify critical tribo-parameters. 2D numerical analysis of the production platform was established to estimate the tool/workpiece interface pressure. The numerical model was validated by geometrical measurements of the final product. For the given ironing process, it was identified that the thickness reduction during the forward stroke is 20 % and during the backward stroke, a reduction of 4 % takes place. Subsequently, it was calculated that the normal pressure on the punch nose is 1050 MPa during the forward stroke, while it reaches up to 2050 MPa during the back-

ward stroke. The reason for such an increase during the ejection of the punch is large strain hardening of the cup wall after the main wall reduction. Additionally, the elastic contraction of the lower die together with a very small contact length between the workpiece and the die leads to large pressure gradients during the backward stroke.

The tool/workpiece interface was further analysed to define the contact temperature. A combined numerical and experimental approach has been developed. The method uses the experimental measurements of the tool temperature in a few points at thermal steady-state. The critical aspects of the experimental design was not only to measure the temperature as close as possible to the tool/workpiece interface but also to define the exact measurement points. For that, computed tomography scanning of the punch was performed and the actual thermocouple hole dimensions were identified. The measured temperatures were later used to calculate the steady-state tool temperature distribution, which was the initial temperature distribution of the punch in the subsequent thermo-mechanical analysis. Another input for the thermo-mechanical analysis was the heat transfer coefficient (HTC) between the punch and the workpiece and between the punch and the lubricant. A combined experimental and numerical analysis was applied for the determination of the HTC between the tool and the lubricant. It was found that the HTC in unloaded conditions is 0.15 kW/($m^2 \cdot$ K). A sensitivity analysis of the numerical model was performed to verify the effects of the mesh discretisation, temperature measurement location and tool geometry. Among these parameters, mesh size and the thermocouple insert depth were identified as the critical parameters that affect the measured and calculated temperatures the most. Finally, the instantaneous maximum temperatures with both deformation and frictional heating were found to be around 158 °C and 150 °C for the forward and backward strokes, respectively.

After the detailed analysis of the production platform, the SRT set-up was examined. Similar to what was done during the analysis of the production, a mechanical numerical model was used to investigate the interface pressure. It was found that the interface pressure between tool pin and workpiece increases to 1100 MPa during the emulated forward

stroke and 1700 MPa during the emulated backward stroke. The normal pressure during the backward stroke is slightly lower than the one found in production. The reason is that in production, towards the end of the ejection, the pressure increases continuously due to a greater thickness of the cup wall. Finally, the SRT set-up was redesigned to achieve the desired tool/workpiece contact temperature. Preheating of the tool set-up to 140 °C increases the interface temperature up to 160 °C when simulating the forward stroke. The interface temperature of the emulated backward stroke is limited to 140 °C, which is slightly lower than the one found in production, due to constant thickness reduction and a resulting limited contribution of deformation-induced heating. In fact, the set-up provides the possibility of increasing the preheating temperature of the emulated backward stroke to 150 °C. However, as the experiments at high temperature failed much earlier than in production, the focus was to identify the source of early failure and suggest further enhancements and investigate the effect of various parameters in the results.

The differences between the production and laboratory platform have been listed and by adapting the SRT, the effects of some aspects have been studied. It was found that the lower speed in laboratory may be contributing to more severe process conditions. Although increased speed delays the onset of lubricant film breakdown, the increase in the total number of strokes before the breakdown is limited. Another aspect was to analyse the effect of the thermal exchange in the contact zone for each stroke. In the production, the wall reduction is not continuous as it is in the experiments. To mimic this, experiments in which the strip is drawn without a thickness reduction between each stroke were designed and conducted. A significant enhancement in promoting the delay in onset of lubricant film breakdown was observed. The new process flow provides a new contact between the tool and the workpiece and the resulting thicker lubricant layer improves the process. Furthermore, the set-up is able to cool down during the idle time. Avoiding being in the high-temperature range continuously, the boundary lubricant layer may be preserved much more effectively to expand the process limits. An interesting study for the future may be examining more deeply the boundary lubrication from a materials and/or chemical science perspective to

understand how the boundary lubrication is actually affected by various parameters.

Additional research has been conducted to investigate the potential of new tribo-systems. Among the tested environmentally friendly tribo-systems, the one already used in production is the most promising one. Future work may involve the developer of the lubricants to suggest a more efficient lubricant. An interesting study may involve looking deeper into the process parameters such as examining the effect of variations in the punch speed using a servo-press and optimising the punch nose geometry.

Simulative testing in laboratory requires a careful consideration of many aspects and detailed experimental and numerical design steps. It is challenging to fully match the tribological conditions in the laboratory with the ones in production. Even though there may be differences between the two platforms, the results can be utilised for classifying the tribo-systems and investigating the relative influence of a large variety of parameters on the limits of lubrication. One principal suggestion for future work is to design a tool, place before the emulative test set-up, in order to pre-form the strip, and provide a hardened strip for the emulative test.

To sum up, the proposed off-line methodology for emulating industrial ironing operations has been successfully developed. In fact, the developed methodology including the experimental and numerical set-up and procedures can be used to emulate many other industrial ironing operations. The tool set-up can also be used for other purposes such as testing of various tool and workpiece materials, coatings, lubricants, structured surfaces as well as process parameters. The developed test tool has actually been actively used by other researchers at DTU-MEK [96] [147]. Additionally, the LabVIEW programme has the flexibility to adapt to various ironing operations as well as other simulative tests where the horizontal and the vertical axis are used, such as draw bead testing, without requiring any additional programming tasks. This project has therefore opened up the possibility of implementing various new test tools for other simulative tests.

After concluding that the overall methodology had been developed successfully, the attention was turned to more fundamental research. In mixed lubrication in metal forming, at the contact interfaces between material and tooling, the lubricant acts like a pressure carrier. To improve the understanding of the phenomenon of lubricant escape, a new approach for combined modelling of plastic deformation and liquid lubrication has been proposed. The proposed approach is an alternative to the conventional modelling, in which an artificial friction layer has been used. It solves the liquid flow of the lubricant and the plastic deformation of the metal simultaneously.

The finite element flow formulation allows a full coupling of metal and fluid flow due to velocity-pressure characteristics. The formulation makes it possible to treat metals as high-viscous, incompressible fluids. In the finite element formulation, the deviatoric stresses of metals are coupled with viscous stresses of fluids, and the bulk viscosity of the fluid corresponds to the incompressibility of the metals that is imposed by a penalty factor.

After providing the theoretical and numerical background, the developed approach was successfully applied to the drawing of a strip with one surface pocket. The strip was drawn through a wedge-shaped die where its thickness was reduced as in the SRT. Process parameters, namely friction, back tension, drawing speed and shear viscosity of the liquid were altered. The effects of each scenario on the possible escape of lubricant from the surface pocket by means of the Micro Plasto HydroStatic Lubrication (MPHSL) and Micro Plasto HydroDynamic Lubrication (MPHDL) mechanisms were analysed. The results are comparable with experimental data published previously. Increase in lower die friction and back tension leads to a decrease in the sealing pressure and as a result, the forward lubricant escape, MPHSL, initiates. Increase in the drawing speed and the lubricant shear viscosity, on the other hand, give rise to an increase in the hydrostatic pressure of the lubricant. As a result, the lubricant is dragged backwards and MPHDL is promoted.

In the beginning of the modelling, due to the distortion of the fluid

mesh, the numerical analysis could run only for a limited sliding length. To solve this numerical difficulty resulting from the large difference in stiffness between metals and fluids, a continuous smoothing algorithm was introduced. Yet, in some test cases, poor convergence due to ill-conditioning of the strongly coupled approach was experienced. The current model replicates the MPHSL and MPHDL phenomena only until the onset of lubricant film breakdown. This constraint requires further investigations and may call for a decoupling of the metal flow and the liquid flow, which in the author's opinion would solve the numerical problem of ill-conditioning.

Current limitations in the computer implementation of the proposed fully-coupled approach do not allow replicating the physical escape of the lubricant. Therefore, the approach is not capable of modelling experimental conditions having simultaneous forward and backward escapes of lubricant because it will only be able to determine the onset of the escape mode that will occur first, and not what will happen afterwards.

Bibliography

[1] J. A. Schey, *Metal Deformation Processes: Friction and Lubrication*. Marcel Dekker Inc., 1970.

[2] B. Bhushan, *Introduction to Tribology*. Wiley, 2013.

[3] B. Bhushan, "History of tribology and micro/nanotribology," *NATO ASI Series. Series E, Applied Science*, vol. 330, pp. 1–16, 1997.

[4] J. Williams, *Engineering Tribology*. Cambridge University Press, 2005.

[5] T. Kayaba and K. Kato, "The adhesive transfer of the slip-tongue and the wedge," *ASLE Transactions*, vol. 24, pp. 164–174, 1981.

[6] M. Hanson, *On Adhesion and Galling in Metal Forming*. PhD thesis, Uppsala Universitet. Faculty of Science and Technology, 2008.

[7] T. Altan and A. E. Tekkaya, *Sheet Metal Forming - Fundamentals*. ASM International, 2012.

[8] N. Bay, "Metal forming and lubrication," *Encyclopedia of Materials: Science and Technology*, pp. 5377–5380, 2000.

[9] W. Hardy and I. Doubleday, "Boundary lubrication - the temperature coefficient," *Proceedings of the Royal Society of London Series A-containing Papers of a Mathematical and Physical Character*, vol. 101, pp. 487–492, 1922.

[10] W. S. Hardy, *Collected Scientific Papers*. University Press, 1936.

[11] D. Godfrey, "Boundary lubrication in interdisciplinary approach to friction and wear," in *Proceedings of a NASA-sponsored symposium* (P. M. Ku, ed.), (San Antonio, Texas, USA), pp. 335–384, November 1967.

[12] L. Andrew, "Electron diffraction analysis of the orientation of the molecules of lubricating oils," *Transactions of the Faraday Society*, vol. 32, pp. 607–615, 1936.

[13] J. Israelachvili, P. McGuiggan, and A. Homola, "Dynamic properties of molecularly thin liquid-films," *Science*, vol. 240, pp. 189–191, 1988.

[14] F. Bowden and D. Tabor, *Friction and Lubrication of Solids*. Oxford University Press, 1950.

[15] N. Bay and T. Wanheim, "Contact phenomena under bulk plastic deformation conditions," in *Proceedings of the 3rd International Conference of Technology of Plasticity*, vol. 4, (Kyoto, Japan), pp. 1667–1691, July 1990.

[16] L. Butler, "The influence of base lubricant viscosity and boundary additions on surface contact and friction during metal deformation," *Journal of the Institute of Metals*, vol. 89, pp. 449–455, 1961.

[17] L. Butler, "The effect of variation of base lubricant viscosity on coefficient of friction during metal deformation - the microinterferometry technique," *Journal of the Institute of Petroleum*, vol. 48, pp. 27–31, 1962.

[18] T. Wanheim, "Friction at high normal pressures," *Wear*, vol. 25, pp. 225–244, 1973.

[19] A. Azushima, "Characteristics of lubrication in cold sheet rolling," in *Proceedings of the 1st International Conference of Lubrication Challanges in Metalworking and Processing*, (Chicago, Illinois, USA), pp. 81–87, June 1978.

[20] J. Reid and J. Schey, "Full fluid film lubrication in aluminum strip rolling," *ASLE Transactions*, vol. 21, pp. 191–200, 1978.

[21] S. Lu and Y. Chuang, "Effects of surface roughness on lubrication in cold-rolling of metals," *Journal of Tribology, Transactions of the ASME*, vol. 107, pp. 522–526, 1985.

[22] H. Kudo and A. Azushima, "Interaction of surface microstructure and lubricant in metal forming tribology," in *Proceedings of the 2nd International Conference on Advanced Technology of Plasticity*, (Stuttgart, Germany), pp. 373–384, August 1987.

[23] Y. H. Tsao and L. B. Sargent, "A mixed lubrication model for cold rolling of metals," *ASLE Transactions*, vol. 20, pp. 55–63, 1977.

[24] S. Sheu and W. R. D. Wilson, "Mixed lubrication of strip rolling," *Tribology Transactions*, vol. 37, pp. 483–493, 1994.

[25] N. Patir and H. Cheng, "Application of average flow model to lubrication between rough sliding surfaces," *Journal of Lubrication Technology, Transactions of the ASME*, vol. 101, pp. 220–230, 1979.

[26] W. Wilson and S. Sheu, "Real area of contact and boundary friction in metal forming," *International Journal of Mechanical Sciences*, vol. 30, pp. 475–489, 1988.

[27] P. Lancaster and G. Rowe, "A comparison of boundary lubricants under light and heavy loads," *Wear*, vol. 2, pp. 428–437, 1959.

[28] H. Kudo, "A note on the role of microscopically trapped lubricant at the tool-work interface," *International Journal of Mechanical Sciences*, vol. 7, pp. 383–388, 1965.

[29] T. Nellemann, N. Bay, and T. Wanheim, "Real area of contact and friction stress - the role of trapped lubricant," *Wear*, vol. 43, pp. 45–53, 1977.

[30] T. Mizuno and M. Okamoto, "Effects of lubricant viscosity at pressure and sliding velocity on lubricating conditions in the compression-friction test on sheet metals," *Journal of Lubrication Technology, Transactions of the ASME*, vol. 104, pp. 53–59, 1982.

[31] H. Kudo, M. Tsubouchi, H. Takada, and K. Okamura, "An investigation into plasto-hydrodynamic lubrication with a cold sheet drawing test," *CIRP Annals*, vol. 31, pp. 175–180, 1982.

[32] A. Azushima, T. Tsubouchi, and H. Kudo, "Direct observation of lubricant behaviors under the micro - phl at the interface between workpiece and die," in *Proceedings of the 3rd International Conference on Technology of Plasticity*, (Kyoto, Japan), pp. 551–556, July 1990.

[33] A. Azushima, M. Uda, and H. Kudo, "An interpretation of the speed dependence of the coefficient of friction under the Micro-PHL condition in sheet drawing," *CIRP Annals*, vol. 40, pp. 227–230, 1991.

[34] A. Azushima and H. Kudo, "Direct observation of contact behaviour to interpret the pressure dependence of the coefficient of friction in sheet metal forming," *CIRP Annals - Manufacturing Technology*, vol. 44, pp. 209–212, 1995.

[35] J. Bech, N. Bay, and M. Eriksen, "Entrapment and escape of liquid lubricant in metal forming," *Wear*, vol. 232, pp. 134–139, 1999.

[36] I. Shimizu, J. L. Andreasen, J. I. Bech, and N. Bay, "Influence of workpiece surface topography on the mechanisms of liquid lubrication in strip drawing," *Journal of Tribology, Transactions of the ASME*, vol. 123, pp. 290–294, 2001.

[37] S. Lo and W. Wilson, "A theoretical model of micro-pool lubrication in metal forming," *Journal of Tribology, Transactions of the ASME*, vol. 121, pp. 731–738, 1999.

[38] A. Azushima, A. Yanagida, and S. Tani, "Permeation of lubricant trapped within pocket into real contact area on the end surface of cylinder," *Journal of Tribology, Transactions of the ASME*, vol. 133, pp. 011501–1, 011501–6, 2011.

[39] W. Wilson, "Tribology in cold metal forming," *Journal of Manufacturing Science and Engineering, Transactions of the ASME*, vol. 119, pp. 695–698, 1997.

[40] N. Bay, O. Wibom, and P. A. F. Martins, "Testing of friction and lubrication in bulk metal forming," (Anaheim, USA), November 1998. Keynote paper presented at ASME International Mechanical Engineering Congress and Exposition, IMECE.

[41] N. Bay, D. Olsson, and J. Andreasen, "Lubricant test methods for sheet metal forming," *Tribology International*, vol. 41, pp. 844–853, 2008.

[42] N. Kawai and K. Dohda, "Development of tribology in metal-forming," *JSME International Journal*, vol. 30, pp. 1018–1025, 1987.

[43] S. Kalpakjian, "Recent progress in metal forming tribology," *CIRP Annals*, vol. 34, pp. 585–592, 1985.

[44] S. Lassen and N. Bay, "Evaluation of tribology tests for sheet metal forming," in *IDDRG Working Groups Meeting*, (Linz, Austria), June 1993.

[45] J. L. Andreasen, D. D. Olsson, K. Chodnikiewicz, and N. Bay, "Bending under tension test with direct friction measurement," *Proceedings of the Institution of Mechanical Engineers Part B-journal of Engineering Manufacture*, vol. 220, pp. 73–80, 2006.

[46] D. D. Olsson, N. Bay, and J. L. Andreasen, "Direct friction measurement in draw bead testing," in *Proceedings of the 8th International Conference on Technology of Plasticity*, (Verona, Italy), October 2005.

[47] J. L. Andreasen, N. Bay, M. M. Andersen, E. Christensen, and N. Bjerrum, "Screening the performance of lubricants for ironing of stainless steel with a strip reduction test," *Wear*, vol. 207, pp. 1–5, 1997.

[48] E. Ceron, *New tribo-systems for sheet metal forming of advanced high strength steels and stainless steels*. PhD thesis, Technical University of Denmark. Department of Mechanical Engineering, 2014.

[49] J. Schey and M. McLean, "Critical evaluation of test methods for sheet metalworking lubrication," *American Society of Mechanical Engineers, Materials Division (publication) Md*, vol. 10, pp. 25–32, 1988.

[50] P. K. Saha and W. R. Wilson, "Friction in forming electrogalvanized steel sheet with tool steel and carbide coated tools," *American Society of Mechanical Engineers, Production Engineering Division (publication) Ped*, vol. 67, pp. 209–218, 1993.

[51] M. Jonasson, T. Pulkkinen, L. Gunnarsson, and E. Schedin, "Comparative study of shotblasted and electrical-discharge-textured rolls with regard to frictional behavior of the rolled steel sheet surfaces," *Wear*, vol. 207, pp. 34–40, 1997.

[52] A. Wihlborg and L. Gunnarsson, "A frictional study of uncoated EBT steel sheets in a bending under tension friction test," *Wear*, vol. 237, pp. 129–136, 2000.

[53] P. Carlsson, U. Bexell, and M. Olsson, "Tribological behaviour of thin organic permanent coatings deposited on hot-dip coated steel sheet - a laboratory study," *Surface and Coatings Technology*, vol. 132, pp. 169–180, 2000.

[54] H. Kim, B. Hwang, and W. Bae, "An experimental study on forming characteristics of pre-coated sheet metals," *Journal of Materials Processing Technology*, vol. 120, pp. 290–295, 2002.

[55] M. Alinger and C. Van Tyne, "Evolution of the tribological characteristics of several forming die materials," *Journal of Materials Processing Technology*, vol. 111, pp. 20–24, 2001.

[56] K. J. Weinmann and S. K. Kernosky, "Friction studies in sheet metal forming based on a unique die shoulder force transducer," *CIRP Annals - Manufacturing Technology*, vol. 45, pp. 269–272, 1996.

[57] E. Ceron and N. Bay, "Determination of friction in sheet metal forming by means of simulative tribo-tests," *Key Engineering Materials*, vol. 549, pp. 415–422, 2013.

[58] E. Ceron and N. Bay, "A methodology for off-line evaluation of new environmentally friendly tribo-systems for sheet metal forming," *CIRP Annals - Manufacturing Technology*, vol. 62, pp. 231–234, 2013.

[59] N. Bay and E. Ceron, "Off-line testing of tribo-systems for sheet metal forming production," *Advanced Materials Research*, vol. 966-967, pp. 3–20, 2014.

[60] J. Schey, "Friction in sheet forming with soft and hard tooling," *Steel Research*, vol. 69, pp. 148–153, 1998.

[61] J. Lanzon, M. Cardew-Hall, and P. Hodgson, "Characterising frictional behaviour in sheet metal forming," *Journal of Materials Processing Technology*, vol. 80-1, pp. 251–256, 1998.

[62] M. Vermeulen and J. Scheers, "Micro-hydrodynamic effects in EBT textured steel sheet," *International Journal of Machine Tools and Manufacture*, vol. 41, pp. 1941–1951, 2001.

[63] J. Schey, "Speed effects in drawbead simulation," *Journal of Materials Processing Technology*, vol. 57, pp. 146–154, 1996.

[64] L. Courvoisier, M. Martiny, and G. Ferron, "Analytical modelling of drawbeads in sheet metal forming," *Journal of Materials Processing Technology*, vol. 133, pp. 359–370, 2003.

[65] Y. Joshi, P. Christiansen, I. Masters, N. O. Bay, and R. Dashwood, "Numerical modelling of drawbeads for forming of aluminium alloys," *Journal of Physics: Conference Series (online)*, vol. 734, p. 032082, 2016.

[66] P. Groche and M. Christiany, "Evaluation of the potential of tool materials for the cold forming of advanced high strength steels," *Wear*, vol. 302, pp. 1279–1285, 2013.

[67] P. Groche and G. Nitzsche, "Reduction of friction in deep drawing of aluminium alloys by generating local hydrostatic-pressure lubrication," *Proceedings of the Institution of Mechanical Engineers Part B-journal of Engineering Manufacture*, vol. 220, pp. 43–48, 2006.

[68] L. R. Sanchez, "Experimental investigation of friction effects enhanced by tool geometry and forming method on plane strain sheet metal forming," *Tribology Transactions*, vol. 42, no. 2, pp. 343–352, 1999.

[69] L. Sanchez, "Characterisation of a measurement system for reproducible friction testing on sheet metal under plane strain," *Tribology International*, vol. 32, pp. 575–586, 1999.

[70] S. Fukui, T. Ohi, H. Kudo, I. Takita, and J. Seino, "Some aspects of friction in metal-strip drawing," *International Journal of Mechanical Sciences*, vol. 4, pp. 297–312, 1962.

[71] K. Dohda and N. Kawai, "Compatibility between tool materials and workpiece in sheet-metal ironing process," *Journal of Tribology, Transactions of the ASME*, vol. 112, pp. 275–281, 1990.

[72] J. L. Andreasen and N. Bay, "A strip reduction test for measurement of lubricity in ironing," in *Proceedings of the 19th IDDRG Biennial Congress*, (Eger, Hungary), pp. 435–444, 1996.

[73] S. Aleksandrović, M. Đorđević, M. Stefanović, V. Lazić, D. Adamović, and D. Arsić, "Different ways of friction coefficient determination in stripe ironing test," *Tribology in Industry*, vol. 36, pp. 293–299, 2014.

[74] D. D. Olsson, N. Bay, and J. L. Andreasen, "Prediction of limits of lubrication in strip reduction testing," *CIRP Annals*, vol. 53/1, pp. 231–234, 2004.

[75] J. L. Andreasen, K. Krebs, G. Kann, and N. Bay, "Quantitative evaluation of lubricants and tool surfaces for ironing of stainless steel," in *Proceedings of the 1st International Conference on Tribology in Manufacturing Processes*, (Gifu, Japan), pp. 358–363, October 1997.

[76] G. Kann and K. Krebs, "Tribologi ved strækninsreduktion. (in Danish)," Master's thesis, Technical University of Denmark. Department of Mechanical Engineering, 1997.

[77] J. L. Andreasen, N. Bay, and L. De Chiffre, "Quantification of galling in sheet metal forming by surface topography characterisation," *International Journal of Machine Tools and Manufacture*, vol. 5-6, pp. 503–510, 1998.

[78] D. D. Olsson, *Limits of Lbrication in Sheet Metal Forming of Stainless Steel*. PhD thesis, Technical University of Denmark. Department of Manufacturing Engineering and Management, 2003.

[79] B. Wadman, J. Eriksen, M. Olsson, E. Schedin, E. Madsen, and N. Bay, "Influence of surface texture on the galling characteristics of lean duplex and austenitic stainless steels," in *Proceedings of the Duplex World 2010 Conference and Exhibition*, (Beaune, France,), pp. 1211–1220, October 2010.

[80] M. Moghadam, P. Christiansen, and N. O. Bay, "Detection of the onset of galling in strip reduction testing using acoustic emission," *Procedia Engineering*, vol. 183, pp. 59–64, 2017.

[81] N. Bay, A. Azushima, P. Groche, I. Ishibashi, M. Merklein, H. Morishita, T. Nakamura, S. Schmid, and M. Yoshida, "Environmentally benign tribo-systems for metal forming," *CIRP Annals*, vol. 59, pp. 760–780, 2010.

[82] European Parliment and of the Council, "1907/2006 - REACH." `http://eur-lex.europa.eu/legal-content/EN/TXT/?uri=CELEX%3A02006R1907-20140410`, 2006. Accessed: 2017-01-11.

[83] T. N. I. for Occupational Safety and H. (NIOSH), "Criteria for a recommended standard: Occupational exposure to metalworking fluids." `https://www.cdc.gov/niosh/docs/98-102/`. Accessed: 2017-01-11.

[84] N. Bay, "Trends and visions in metal forming tribology," in *Special Edition: 10th International Conference on Technology of Plasticity, ICTP*, (Aachen, Germany), pp. 15–26, September 2011.

[85] A. Azushima and Y. Jimbo, "Effect of carbide properties on lubrication characteristics of roll in cold sheet rolling. (in Japanese)," *Journal of the Iron and Steel Institute of Japan*, vol. 81, pp. 1150–1155, 1995.

[86] Y. Jimbo and A. Azushima, "Effect of carbide properties of roll materials on lubricity in cold sheet rolling of low-carbon steel," *International Journal of Machine Tools and Manufacture*, vol. 41, pp. 347–360, 2001.

[87] O. Sandberg, "Advanced low-friction tool steel for metal processing: Properties and industrial experiences," *International Journal of Microstructure and Materials Properties*, vol. 3, pp. 391–400, 2008.

[88] S. Kataoka, M. Murakawa, T. Aizawa, and H. Ike, "Tribology of dry deep-drawing of various metal sheets with use of ceramics tools," *Surface and Coatings Technology*, vol. 177, pp. 582–590, 2004.

[89] K. Tamaoki, K. Manabe, S. Kataoka, and T. Aizawa, "Electroconductive ceramic tooling for dry deep drawing," *Journal of Materials Processing Technology*, vol. 210, pp. 48–53, 2010.

[90] K. Tamaoki, K. Manabe, S. Kataoka, and T. Aizawa, "Continuous dry cylindrical and rectangular deep drawing by electroconductive ceramic dies," *Journal of Manufacturing Science and Engineering, Transactions of the ASME*, vol. 135, p. 0310107, 2013.

[91] H. Kim, S. Han, Q. Yan, and T. Altan, "Evaluation of tool materials, coatings and lubricants in forming galvanized advanced high strength steels (AHSS)," *CIRP Annals-Manufacturing Technology*, vol. 57, pp. 299–304, 2008.

[92] F. Klocke, T. Massmann, K. Bobzin, E. Lugscheider, and N. Bagcivan, "Carbon based tool coatings as an approach for environmentally friendly metal forming processes," *Wear*, vol. 260, pp. 287–295, 2006.

[93] M. Murakawa, N. Koga, and T. Kumagai, "Deep-drawing of aluminum sheets without lubricant by use of diamond-like carbon coated dies," *Surface and Coatings Technology*, vol. 76-77, pp. 553–558, 1995.

[94] T. Aizawa, E. Iwamura, and K. Itoh, "Nano-lamination in amorphous carbon for tailored coating in micro-dry stamping of AISI-304 stainless steel sheets," *Surface and Coatings Technology*, vol. 203, pp. 794–798, 2008.

[95] J. Vetter, "60 years of DLC coatings: Historical highlights and technical review of cathodic arc processes to synthesize various DLC types, and their evolution for industrial applications," *Surface and Coatings Technology*, vol. 257, pp. 213–240, 2014.

[96] M. H. B. Sulaiman, P. Christiansen, and N. O. Bay, "A study of DLC coatings for ironing of stainless steel," *IOP Conference Series: Materials Science and Engineering*, vol. 896, p. 011001, 2017.

[97] E. Üstünyagiz, M. Hafis Sulaiman, P. Christiansen, C. V. Nielsen, and N. Bay, "A study on DLC tool coating for deep drawing and ironing of stainless steel," *Key Engineering Materials*, vol. 767, pp. 181–188, 2018.

[98] G. Finstermann, G. Nopp, N. Eisenkock, and G. Keintzel, "New advances in temper and skin-pass rolling technology," in *Proceedings of AISE (the Association of Iron and Steel Engineers) Annual Convention*, (Nashville, Tennesee, USA), 2002.

[99] J. Simao, D. Aspinwall, M. Wise, and M. Elmenshawy, "Mill roll texturing using EDT," *Journal of Materials Processing Technology*, vol. 45, pp. 207–214, 1994.

[100] M. H. B. Sulaiman, *Development and Testing of Tailored Tool Surfaces for Sheet Metal Forming*. PhD thesis, Technical University of Denmark. Department of Mechanical Engineering, 2017.

[101] Strecon, "Strecon robot polishing machine / RAP." `http://www.strecon.com/media/1242/web_4887_strecon-pn_rap_robotpolishingmachine.pdf`. Accessed: 2018-04-04.

[102] "SHETRIB - New environmentally benign sheet metal forming tribology systems." `http://www.shetrib.mek.dtu.dk/`. Accessed: 07.11.2017.

[103] U. Staehr and C. E. Jensen, "Grundfos product information MAGNA1 medium/large," tech. rep., Grundfos A/S, 2014.

[104] Outokumpu. `http://steelfinder.outokumpu.com/properties/`.

[105] "Uddeholm Vanadis 4 Extra SuperClean," tech. rep., Uddeholm, 2016.

[106] "Sikkerhedsdatablad ifolgeforordning (EF) 1907/2006, Rhenus LA 722086. (in Danish)," tech. rep., Rhenus, 2013.

[107] E. Üstünyagiz, C. V. Nielsen, P. Christiansen, P. A. Martins, and N. Bay, "Continuous strip reduction test simulating tribological conditions in ironing," *Procedia Engineering*, vol. 207, pp. 2286–2291, 2017.

[108] Kistler, "Kistler instruction manual reaction torque sensors," tech. rep., Kistler, 2009.

[109] J. L. Endrino, G. S. Fox-Rabinovich, and C. Gey, "Hard AlTiN, AlCrNPVD coatings for machining of austenitic stainless steel," *Surface and Coatings Technology*, vol. 200, pp. 6840–6845, 2006.

[110] E. Üstünyagiz, C. V. Nielsen, and N. Bay, "A systematic approach to analyse critical tribological parameters in an industrial case study of progressive die sequence production," in *Proceedings of the 8th International Seminar on Precision Forging*, (Nagoya, Japan), March 2018.

[111] O. Pawelsky, "Über das stauchen von hohlzylindern und seine eignung zur bestimmung der formänderungsfestigkeit dünner bleche. (in German)," *Archiv für das Eisenhüttenwesen*, vol. 38, pp. 437–442, 1967.

[112] M. Merklein and A. Kuppert, "A method for the layer compression test considering the anisotropic material behavior," *International Journal of Material Forming*, vol. 2, pp. 483–486, 2009.

[113] L. Alves, C. V. Nielsen, and P. Martin, "Revisiting the fundamentals and capabilities of the stack compression test," *Experimental Mechanics*, vol. 51, pp. 1565–1572, 2011.

[114] M. R. Jensen, "Specification of directional depended materials in LS-DYNA," tech. rep., Livermore Software Technology Corporation, 2005-2011.

[115] E. Üstünyagiz, C. V. Nielsen, N. S. Tiedje, and N. Bay, "Combined numerical and experimental determination of the convective heat transfer coefficient between an AlCrN-coated Vanadis

4E tool and Rhenus oil," *Measurement*, vol. 127, pp. 565–570, 2018.

[116] E. Üstünyagiz, C. V. Nielsen, P. Christiansen, P. A. Martins, T. Altan, and N. Bay, "A combined numerical and experimental approach for determining the contact temperature in an industrial ironing operation," *Journal of Materials Processing Technology*, vol. 264, pp. 249–258, 2018.

[117] W. S. Farren and G. I. Taylor, "The heat developed during plastic extension of metals," *Proceedings of the Royal Society A: Mathematical, Physical and Engineering Sciences*, vol. 107, pp. 422–451, 1925.

[118] S. L. Semiatin, E. W. Collings, V. E. Wood, and T. Altan, "Determination of the interface heat transfer coefficient for non-isothermal bulk-forming processes," *Journal of Engineering for Industry*, vol. 109, p. 49, 1987.

[119] P. Burte, Y.-T. Im, T. Altan, and S. Semiatin, "Measurement and analysis of heat transfer and friction during hot forging," *American Society of Mechanical Engineers, Production Engineering Division (publication) Ped*, vol. 30, pp. 105–116, 1988.

[120] V. K. Jain, "Determination of heat transfer coefficient for forging applications," *Journal of Materials Shaping Technology*, vol. 8, pp. 193–202, 1990.

[121] P. Bariani, G. Berti, T. Dal Negro, and S. Masiero, "Experimental evaluation and FE simulation of thermal conditions at tool surface during cooling and deformation phases in hot forging operations," *CIRP Annals-manufacturing Technology*, vol. 51, pp. 219–222, 2002.

[122] K. Asai and K. Kitamura, "Estimation of frictional property of lubricants for hot forging of steel using low-speed ring compression test," *Procedia Engineering*, vol. 81, pp. 1970–1975, 2014.

[123] K. Asai, K. Kitamura, N. Yukawa, and N. Hayashi, "Estimation of friction by using improved calibration curves of ring compression test for hot forging of steel," *Procedia Engineering*, vol. 207, pp. 2280–2285, 2017.

[124] M. P. Pereira and B. F. Rolfe, "Temperature conditions during 'cold' sheet metal stamping," *Journal of Materials Processing Technology*, vol. 214, pp. 1749–1758, 2014.

[125] A. Fallahiarezoodar, R. Peker, and T. Altan, "Temperature increase in forming of advanced high-strength steels effect of ram speed using a servodrive press," *Journal of Manufacturing Science and Engineering, Transactions of the ASME*, vol. 138, p. 094503, 2016.

[126] P. S. Nielsen, K. S. Friis, and N. Bay, "Testing and modelling of new tribo-systems for industrial sheet forming of stainless steels," *Proceedings of the Institution of Mechanical Engineers, Part J: Journal of Engineering Tribology*, vol. 225, pp. 1036–1047, 2011.

[127] E. Ceron, P. A. Martins, and N. Bay, "Thermal analysis of bending under tension test," *Procedia Engineering*, vol. 81, pp. 1805–1810, 2014.

[128] Omega, "ANSI and IEC color codes for thermocouples, wire and connectors." `https://www.omega.com/temperature/pdf/tc_colorcodes.pdf`. Accessed: 2017-02-01.

[129] K. L. Friis, "Nye tribologiske systemer til pladeformgivning. (in Danish)," Master's thesis, Technical University of Denmark. Department of Mechanical Engineering, 2007.

[130] P. S. Nielsen, "Testning af nye tribosystemer til pladeformgivning. (in Danish)," Master's thesis, Technical University of Denmark. Department of Mechanical Engineering, 2008.

[131] P. Henningsen and J. Hattel, "Measurement of temperature and determination of the heat transfer coefficient in backward can extrusion," in *Proceedings of the first ESAFORM conference on material forming*, (Paris, France), pp. 85–88, 1998.

[132] Omega, "Comparison of time constant vs. overall outside diameter of bare thermocouple wires of grounded junction thermocouples in air." `https://www.omega.co.uk/techref/pdf/z051.pdf`. Accessed: 2017-02-01.

[133] T. Altan and A. E. Tekkaya, *Sheet Metal Forming - Processes and Applications*. ASM International, 2012.

[134] S. Lee, M. Nogami, S. Yamaguchi, T. Kurabuchi, and N. Ohira, "Evaluation of heat transfer coefficients in various air-conditioning modes by using thermal manikin," (Le Bourget Du Lac, France), pp. 2289–2296, August 2013.

[135] "Handbook of stainless steel," tech. rep., Outokumpu, 2013.

[136] P. R. Burte, Y.-T. Im, T. Altan, and S. L. Semiatin, "Measurement and analysis of heat transfer and friction during hot forging," *Journal of Engineering for Industry*, vol. 112, p. 332, 1990.

[137] E. Üstünyagiz, P. Christiansen, C. V. Nielsen, N. Bay, and P. A. Martins, "A fully-coupled approach for modelling plastic deformation and liquid lubrication in metal forming," in *Proceedings of the 7th International Conference on Tribology in Manufacturing Processes*, (Phuket, Thailand), pp. 45–56, February 2016.

[138] E. Üstünyagiz, P. Christiansen, C. V. Nielsen, N. Bay, and P. A. Martins, "Revisiting liquid lubrication methods by means of a fully coupled approach combining plastic deformation and liquid lubrication," *Journal of Engineering Tribology*, vol. 231, pp. 1425–1433, 2017.

[139] E. Üstünyagiz, P. Christiansen, C. V. Nielsen, N. Bay, and P. A. Martins, "A fully-coupled approach combining plastic deformation and liquid lubrication," in *12th International Conference on Numerical Methods in Industrial Forming Processes*, (Troyes, France), July 2016.

[140] Y. Carretta, R. Boman, J. Ponthot, N. Legrand, M. Laugier, and T. Quang, "Multiscale modelling of the micro-plasto-hydrodynamic lubrication – a crucial mechanism for friction in metal forming," in *Proceedings of the 6th International Conference on Coupled Problems in Science and Engineering - Coupled Problems*, (Venice, Italy), May 2015.

[141] Y. Carretta, J. I. Bech, N. Legrand, M. Laugier, J. P. Ponthot, and R. Boman, "Numerical modelling of micro-plasto-hydrodynamic lubrication in plane strip drawing," *Tribology International*, vol. 110, pp. 378–391, 2017.

[142] A. Tekkaya and P. Martins, "Accuracy, reliability and validity of finite element analysis in metal forming: a user's perspective," *International Journal for Computer-Aided Engineering and Software*, vol. 26, pp. 1026–1055, 2009.

[143] C. Nielsen, W. Zhang, L. Alves, N. Bay, and P. Martins, *Modelling of Thermo-Electro-Mechanical Manufacturing Processes*. Springer, 2013.

[144] D. Banabic, *Sheet Metal Forming Processes - Constitutive Modelling and Numerical Simulation*. Springer, 2010.

[145] O. Zienkiewicz and R. Taylor, *The Finite Element Method*, vol. 1. Butterworth-Heinemann, 2000.

[146] S. Koboyashi, S.-I. Oh, and T. Altan, *Metal Forming and The Finite Element Method*. New York: Oxford University Press, 1989.

[147] M. Moghadam, C. V. Nielsen, P. Christiansen, and N. Bay, "Tool condition monitoring in strip reduction testing using acoustic emission," in *Proceedings of the 8th International Seminar on Precision Forging*, (Nagoya, Japan), March 2018.

Appendix A

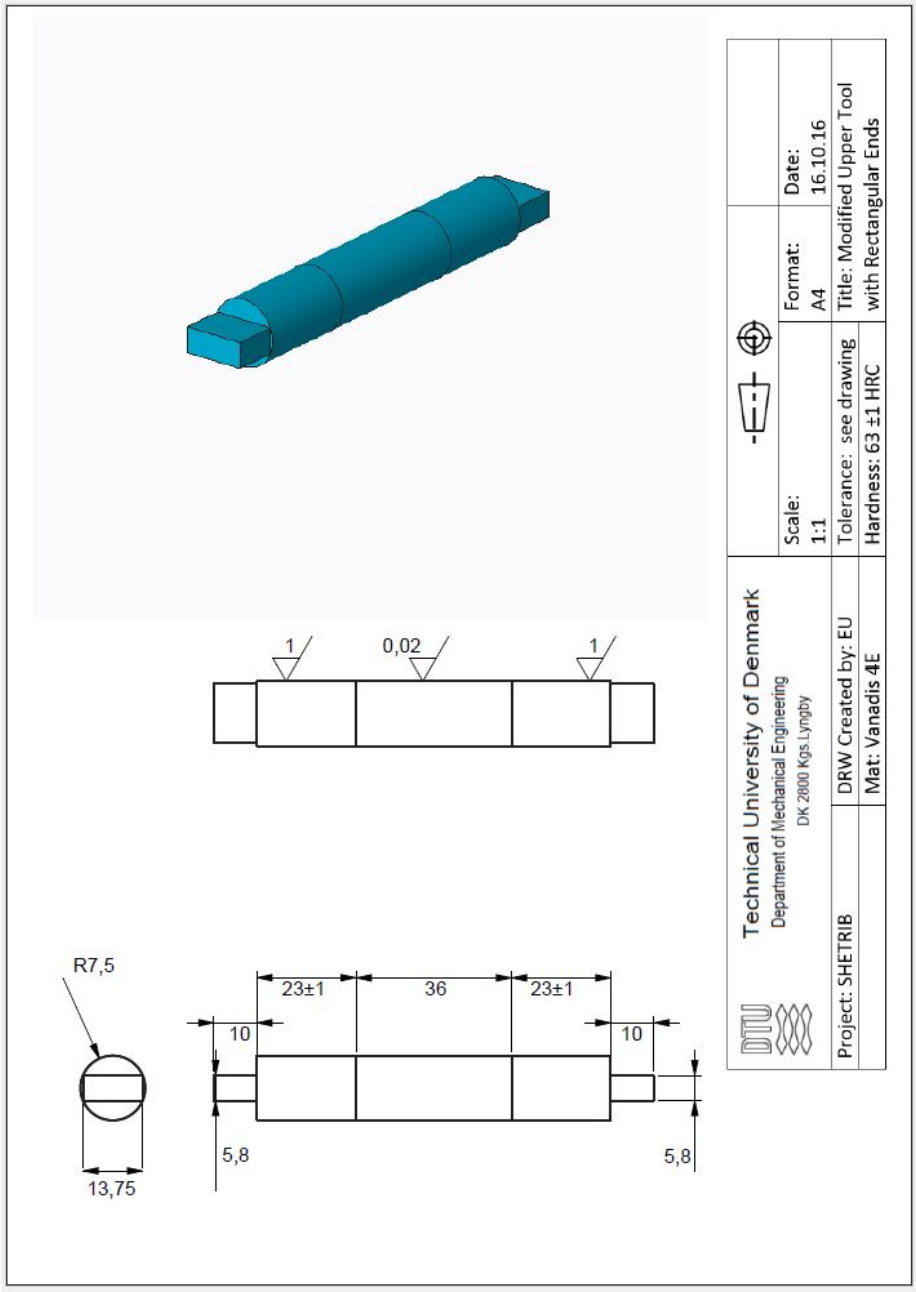
1
0,02
1
R7,5
23±1
36
23±1
10
10
5,8
5,8
13,75
Technical University of Denmark
Department of Mechanical Engineering
DK 2800 Kgs.Lyngby
Scale: 1:1
Format: A4
Date: 16.10.16
Project: SHETRIB
DRW Created by: EU
Tolerance: see drawing
Title: Modified Upper Tool with Rectangular Ends
Mat: Vanadis 4E
Hardness: 63 ±1 HRC

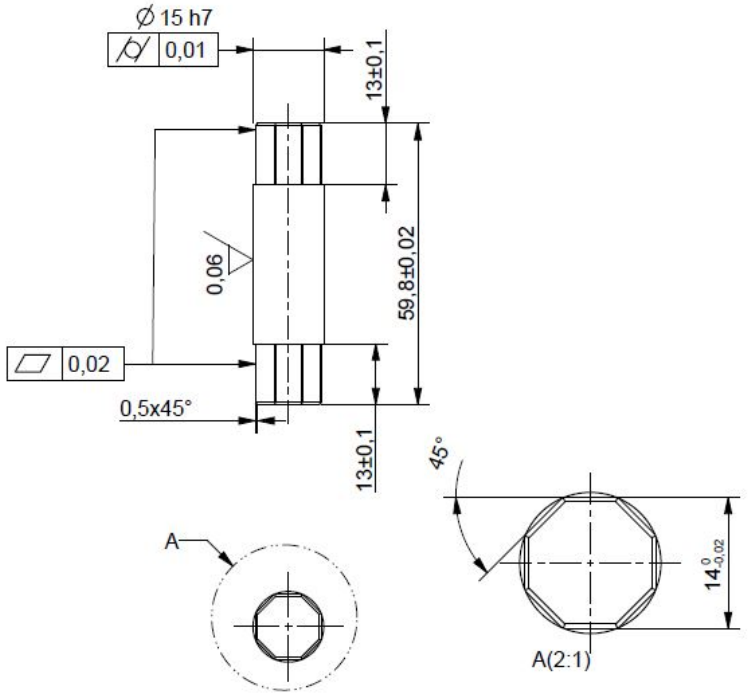

Hærdes til 63+-1 HRC

IPU Teknologiudvikling Produktionstorvet, Bygn. 425 DK-2800 Kgs. Lyngby +45 45254600 Fax: +45 45930190 WWW.IPU.DK		X / X X / X X / X Date: / Name:	
Project: Tribotester v3	DRW Created by: NAP Model Created by:	Tolerance: see drawing	Titel: Bottom tool
Project no.: 2581	Mat.: VANADIS 4	Sheet 1 / 1	Drawing number: 2581-0211-1

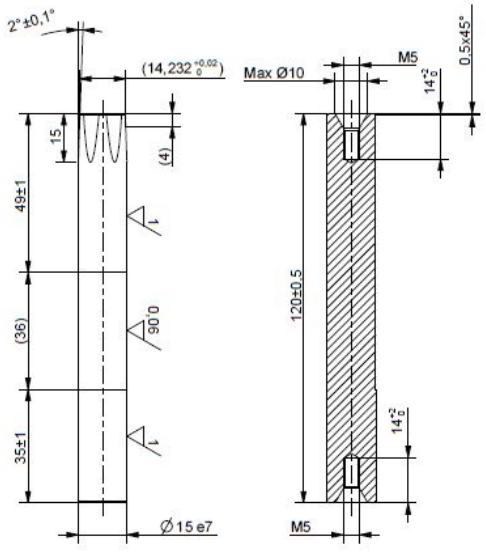

SECTION A-A

Hærdes til 63+-1 HRC

IPU Teknologiudvikling Produktionshavet, Bygn. 425 DK-2800 Kgs. Lyngby +45 4525 4600 Fax: +45 45 930 190 WWW.IPU.DK		Scale: 1:1 / Format: A3	X / X X / X X / X Date: / Name:
Project: Tribotester v3	DRW Created by: NAP Model Created by:	Tolerance: see drawing	Titel: Measuring-tool
Project no.: 2581	Mat.: VANADIS 4	Sheet 1 / 1	Drawing number: 2581-0112-1

Appendix B

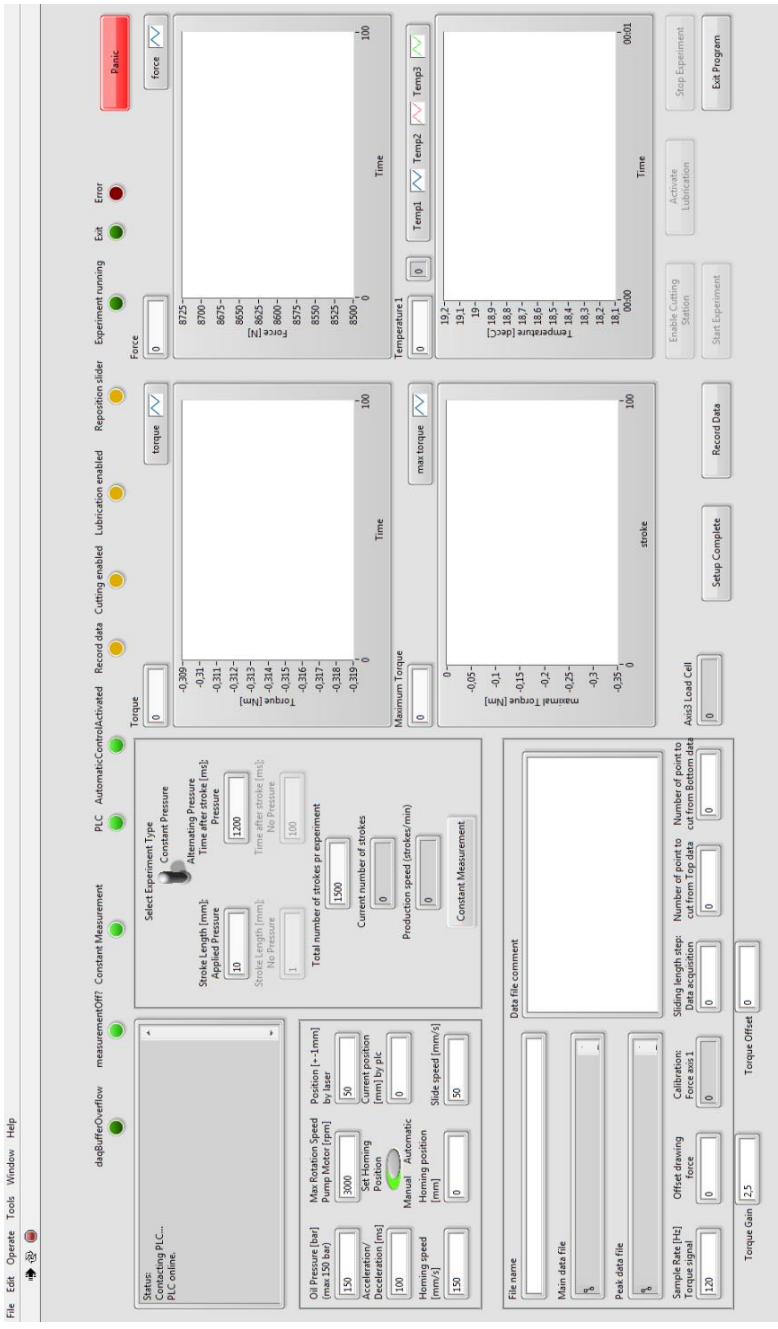
File Edit Operate Tools Window Help
daqBufferOverflow
measurementOff?
Constant Measurement
PLC
AutomaticControlActivated
Record data
Cutting enabled
Lubrication enabled
Reposition slider
Experiment running
Exit
Error
Panic
Status:
Contacting PLC...
PLC online.
Select Experiment Type
Constant Pressure
Alternating Pressure
Stroke Length [mm]:
Applied Pressure
Time after stroke [ms]:
Pressure
Oil Pressure [bar] (max 150 bar)
Max Rotation Speed Pump Motor [rpm]
Position [+-1mm] by laser
Acceleration/ Deceleration [ms]
Set Homing Position
Current position [mm] by plc
Manual
Automatic
Homing speed [mm/s]
Homing position [mm]
Slide speed [mm/s]
Total number of strokes pr experiment
Current number of strokes
Production speed (strokes/min)
Constant Measurement
Torque
Maximum Torque
Force
torque
max torque
force
Torque [Nm]
Time
stroke
maximal Torque [Nm]
Force [N]
Temperature 1
Temperature [decC]
Temp1
Temp2
Temp3
File name
Main data file
Peak data file
Data file comment
Sample Rate [Hz] Torque signal
Offset drawing force
Calibration: Force axis 1
Sliding length step: Data acquisition
Number of point to cut from Top data
Number of point to cut from Bottom data
Axis3 Load Cell
Setup Complete
Record Data
Enable Cutting Station
Start Experiment
Activate Lubrication
Stop Experiment
Exit Program
Torque Gain
Torque Offset

Appendix C

This Appendix is taken from the technical report of Frederik Winther Andersen, who completed a 5 ECTS special Master's course *'Implementation of temperature measurements in strip reduction testing on new tribo tester'* under the supervision of Esmeray Üstünyagiz and Chris V. Nielsen.

Calibration

Before the thermocouple can be used, it has to be calibrated. This is done to be sure that the measured temperature is correct. The calibration is performed by assuming the thermocouple to be linear and exposing the thermocouple to two reference temperatures. A linear regression can thereby be made and the calibration constants x and y can be found. Thereby, the calibrated temperature is a function of the uncalibrated temperature. The first temperature is at a known room temperature and the other is the boiling temperature for water at a known pressure.

The room temperature is measured with two Resistance Detector Thermometer (RTD) sensors, which have very high accuracy. The RTD sensors were calibrated at DTU Risø and are certified. The calibration is made inside a thermally insulated box for keeping the temperature as constant as possible. Thermocouples and RTD sensors are kept inside

the insulated box for an hour to get an as stable temperature as possible. Within the time the temperature was measured, an average temperature is found. The average value for both of the RTD sensors is also found. This is found to be 20.12°C. This is set to be the known room temperature.

The temperature at which water boils at a specific pressure can be found by the Clausis Clapeyron Equation:

$$\ln\left(\frac{P_1}{P_2}\right) = \frac{\Delta H_{vap}}{R}\left(\frac{1}{T_2} - \frac{1}{T_1}\right).$$

T_1 is the boiling temperature in Kelvin at the pressure P_1. At one atmosphere, water boils at 100° C. Respectively T_2 and P_2 are the boiling temperature and pressure on the day the experiment was performed.

R is the gas constant $\left(8.315\frac{J}{mol\cdot K}\right)$ and ΔH_{vap} is the enthalpy of vaporisation $\left(40.66\frac{kJ}{mol}\right)$. The pressure the 8th of February 2017 was measured to 103.41Pa in Jaegersborg, closest weather station, situating 2.8 km to DTU. By solving for T_2 the boiling temperature is found:

$$T_2 = \frac{1}{\frac{1}{T_1} - \frac{R\ln\left(\frac{P_2}{P_1}\right)}{\Delta H_{vap}}} = \frac{1}{\frac{1}{373.15K} - \frac{8.315\frac{J}{mol\cdot K}\ln\left(\frac{1.0205atm}{1atm}\right)}{40.66\frac{kJ}{mol}}} = 100.58^\circ C.$$

The thermocouples are then submerged into boiling water and the measurement is conducted.

Appendix D

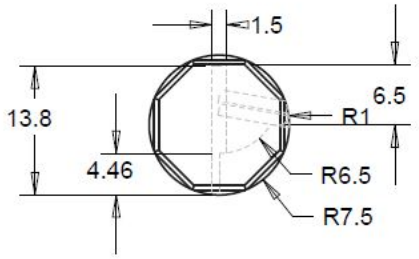

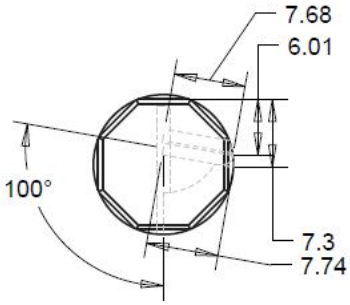

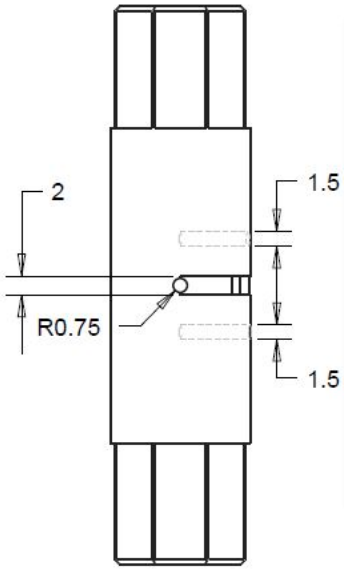

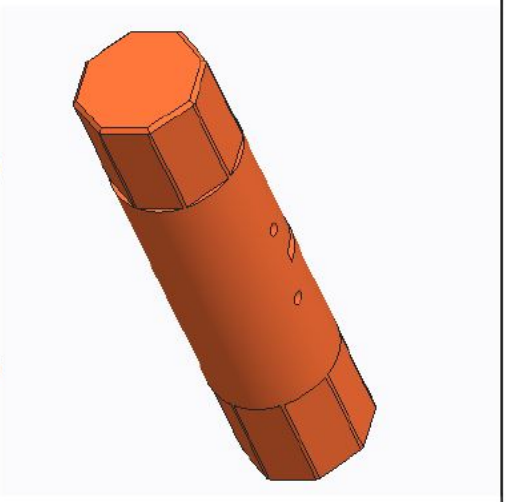

SCALE 2.000

DTU Technical University of Denmark Department of Mechanical Engineering DK 2800 Kgs.Lyngby				
		Scale: 2:1	Format: A4	Date: 02.02.17
Project: SHETRIB	DRW Created by: EU	Tolerance: +0.1	Title: Lower Tool with Thermocouple Insert Holes	
	Mat: Vanadis 4E	Hardness: 63 ±1 HRC		

DTU Mechanical Engineering
Section of Manufacturing Engineering
Technical University of Denmark

Produktionstorvet, Bld. 427A
DK-2800 Kgs. Lyngby
Denmark
Phone (+45) 4525 4763
Fax (+45) 4593 0190
www.mek.dtu.dk
ISBN: 978-87-7475-544-9